THESIS – TL142501

TERNARY PALLADIUM BASED CATHODE CATALYST SUPPORTED ON NITROGEN DOPED REDUCED GRAPHENE OXIDE FOR AEMFC

FRIZKA VIETANTI
NRP. 02511650010006

SUPERVISORS
Diah Susanti, S.T., M.T., Ph.D
Lukman Noerochim, S.T., M.Sc.Eng., Ph.D

MAGISTER PROGRAMME
INNOVATIVE MATERIAL
MATERIAL DEPARTMENT
FACULTY OF INDUSTRIAL TECHNOLOGY
SEPULUH NOPEMBER INSTITUTE OF TECHNOLOGY
SURABAYA
2018

Tesis disusun untuk memenuhi salah satu syarat memperoleh
gelar
Magister Teknik
di
Institut Teknologi Sepuluh Nopember
Oleh:
Frizka Vietanti
NRP 02511650010006

Tanggal Ujian : 13 Juli 2018
Periode Wisuda : September 2018

Disetujui oleh :

1. Diah Susanti, S.T., M.T., Ph.D.
NIP. 197701162003122007 (Pembimbing I)

2. Lukman Noerochim, S.T., M.Sc.Eng., Ph.D
NIP. 197703132003121001 (Pembimbing II)

3. Dr. Widyastuti,S.Si,M.Si
NIP. 197906202006042001 (Penguji)

4. Sigit Tri Wicaksono, S.Si., M.Si.,Ph.D
NIP. 197801132002121003 (Penguji)

Dekan Fakultas Teknologi Industri

Dr. Bambang Lelono Widjiantoro, S.T., M.T.
NIP. 196905071995121001

M10604818
Thesis Advisor:Chen-Hao Wang

碩士學位考試委員會審定書

Qualification Form by Master's Degree Examination Committee

Department:Department of Materials Science and Engineering

Student's Name:Frizka Vietanti

Thesis Title:

Ternary Palladium based Supported on Nitrogen doped Reduced Graphene Oxide for AEMFC Cathode Catalyst

This is to certify that the dissertation submitted by the student named above, is qualified and approved by the Examination Committee.

Degree Examination Committee

Members' Signatures:

Shao-Ju Shih

Chen-Hao Wang

Advisor: Chen-Hao Wang

Program Director's Signature:

Department/Institute Chairman's Signature: 顏怡文

Date: 2018 / 07 / 02 (yyyy/mm/dd)

TERNARY PALLADIUM BASED CATHODE CATALYST SUPPORTED ON NITROGEN DOPED REDUCED GRAPHENE OXIDE FOR AEMFC

Student Name : Frizka Vietanti
NRP : 02511650010006
Supervisor - 1 : Diah Susanti, S.T., M.T., Ph.D.
Supervisor - 2 : Lukman Noerochim, S.T., M.Sc.Eng., Ph.D

ABSTRACT

The oxygen reduction reaction (ORR) is a fundamental reaction in fuel cells to generate power, for which ternary Pd-based with carbon based catalyst plays an important role. Herein, we report the three steps synthesis of ternary Pd-M (M= Fe, Co, Ni) incorporated nitrogen doped graphene (N-rGO) composite, which generated high ORR activity, good stability, and tolerance for methanol oxidation in alkaline media. This method involved a microwave hydrothermal to synthesize nitrogen doped graphene, an emulsion to synthesize ternary Pd-M, and a rota-evaporator technique to make a composite. For ORR, decreased activity were found PdFeCo/N-rGO > PdCoNi/N-rGO > PdFeNi/N-rGO. The PdFeCo/N-rGO catalyst has demonstrated the highest electron transfer number, which is close to dominant four electron pathway, and also generated least yield of % HO_2^-. This confirmed to X-ray diffraction (XRD) pattern of PdFeCo/N-rGO also showed the smallest crystallite size and the highest I_D/I_G which caused extra defects on carbon, thus led to increase ORR activity. There is no obvious agglomeration and the homogeneous distribution of PdFeCo/N-rGO nanoparticles over the layered graphene sheets were clearly observed from field emission scanning electron microscopy (FE-SEM) and representative field emission transmission electron microscope (FE-TEM) images. In addition, the X-ray photoelectron spectroscopy (XPS) was studied for elemental composition and presence highest precentage of graphitic-N which can increase active site leading to enhance the ORR activity.

Keywords: ternary Pd-M (M = Fe, Ni, and Co), N-rGO, oxygen reduction reaction, stability, methanol oxidation

– An intentionally blank page –

KATODA KATALIS BERBASIS TERNARI PALLADIUM DIDUKUNG DENGAN *NITROGEN DOPED REDUCED GRAPHENE OXIDE* UNTUK AEMFC

Nama Mahasiswa : Frizka Vietanti
NRP : 02511650010006
Pembimbing - 1 : Diah Susanti, S.T., M.T., Ph.D.
Pembimbing - 2 : Lukman Noerochim, S.T., M.Sc.Eng., Ph.D

ABSTRAK

Oxygen reduction reaction (ORR) adalah suatu reaksi dasar dalam sistem sel bahan bakar untuk menghasilkan energi, dimana berbasis Pd yang dikompositkan dengan dengan material berbasis karbon memainkan peranan penting. Kami telah melakukan sisntesis komposit Pd-M (M = Fe, Co, Ni) dengan *nitrogen doped graphene* (N-rGO), yang menghasilkan aktivitas ORR tinggi, stabilitas yang baik, dan toleransi untuk oksidasi metanol dalam media basa. Metodenya terdiri dari mickowave hidrotermal untuk mensintesis *nitrogen doped graphene*, metode emulsi untuk mensintesis ternari Pd-M, dan metode rota-evaporator untuk mengkompositkan Pd-M/N-rGO. Performa ORR yang dihasilkan meninjukkan PdFeCo / N-rGO> PdCoNi / N-rGO> PdFeNi / N-rGO. Katalis PdFeCo / N-rGO menghasilkan jumlah elektron transfer tertinggi yang menunjukkan kecenderungan mekanisme empat elektron serta menghasilkan % HO2- yang kecil. Hal ini juga terkonfirmasi pada analisa *X-ray diffraction* (XRD) dari PdFeCo/N-rGO yang menunjukkan ukuran kristal terkecil dan ID / IG tertinggi yang menyebabkan cacat ekstra pada karbon, sehingga menyebabkan peningkatan aktivitas ORR. Tidak ada aglomerasi yang jelas dan distribusi homogen dari nanopartikel PdFeCo / N-rGO di atas lembaran graphene berlapis yang jelas diamati dari *field emission scanning electron microscopy* (FE-SEM) dan *field emission transmission electron microscopy* (FE-TEM). Selain itu, X-ray photoelectron spectroscopy (XPS) digunakanuntuk mengetahui komposisi masing-masing elemen dan prosentase tertinggi dari grafitik-N yang dapat meningkatkan aktivitas ORR.

Keywords: ternari Pd-M (M = Fe, Ni, and Co), N-rGO, *oxygen reduction reaction*, stabilitas, oksidasi metanol

– An intentionally blank page –

ACKNOWLEDGEMENT

Praises is given to My Dearest God, Allah SWT, which always blessed me, so I can complete this thesis which its titled **"Ternary Palladium based Cathode Catalyst Supported on Nitrogen doped Reduced Graphene Oxide for AEMFC".** This thesis was conducted to fulfill Engineering Double Master Degree requirement both of Materials Science and Engineering Department in National Taiwan University of Science and Technology and Materials Engineering Department in Sepuluh Nopember Institute of Technology.

My mother and my father, thank you for your support and kind prayer to me. I am sorry for leaving you for one year. Thank you for permitting me to study aboard although I should leave you. For my brother and sister, thank you for always give me motivation and spirit. Especially for my love, Dio Alif Widiyanto, you are my best love in my heart. Thank you so much for your support. Your motivation and prayer always become my spirit. Thank you for your family who also always support and motivate to study here.

Special thanks to my supervisors, Professor Chen-Hao Wang, Mrs. Diah Susanti, and Mr. Lukman Noerochim for teaching and supporting me. Kai-Chin Wang as my doctoral senior student who always helps me a lot for giving new knowledge starting in the first time when I came to lab until finished my thesis. Hsin-Chih as my postdoctoral, thank you for all of your kindness always help me to solve my problem research.

Moreover, I would like to say thank you for labmates of E1-133. Fariz, Belle, Junior, Ting-Ruei, Cheng-Yi, JC, GC, Marry, Yu-Chun, Yi-An, Anteh, and Teddy, thanks a lot for your help during my experiment. You already introduced some intruments which I never know how to operate it. Thank you for being my best friends and I will miss you all. Good luck for you and hopefully you will get the best future in our beloved country.

– An intentionally blank page –

TABLE OF CONTENT

– An intentionally blank page –

LIST OF FIGURE

LIST OF TABLE

– An intentionally blank page –

CHAPTER I
INTRODUCTION

1.1 Research Background

The ORR is a fundamental reaction in fuel cells to generate power. During its evolution, there are many fuel cell unit configurations are proposed, based on different electrolyte and electrode materials, catalysts and operation temperatures. Solid-state alkaline exchange membrane fuel cell (AEMFC) is considered to be a more promising energy conversion device for stationary and mobile applications compared with the acidic fuel cell because of the enhanced reaction kinetics for both oxygen reduction and fuel oxidation in the alkaline medium, which can lead to higher efficiencies [1]. The advantage over other fuel cells is easier to operate at low temperature (23-70°C) [2].

Regarding for fuel cell operation, carbon-supported platinum (Pt/C) catalyst has well known as the best material for cathode catalyst fuel cell application due to high ORR performance. However, Pt catalyst materials are limited reserve, high cost, and instability of the fuel cell operating condition [3]. Moreover, Pt NPs at the cathode under electrochemical oxidation conditions tend to migrate and grow through Oswald ripening process [4]. Therefore, numerous strategies have been employed. Some non-Pt based electrocatalysts were also suggested for oxidation reaction, but their stability was not unequivocally established [5]. The examination of ORR in alkaline solutions has revealed that Pd exhibits higher activity than in acidic solutions due to a decrease in the anion poisoning effect in alkaline solutions [6-9]. The price of Pd is practically five times lower than the price of platinum. Transition metals serve as a promising alternative due to their intrinsic activity and sufficient stability in oxidative electrochemical environments. Among wide range of these metals, cobalt, nickel, and iron, have been extensively explored as bifunctional catalysts, capable of simultaneously catalyzing ORR. Not only do they show innate electrochemical capabilities, but their structural diversity, as well as their ability to be mixed, doped, and combined with other materials [10]. Pd exhibits considerable catalytic activity toward ORR, which promotes Pd alloys as feasible alternatives in the development of nonplatinum catalysts with catalytic activity similar to that of Pt. The transition metals addition are used for alloying Pd such as PdFe [11-15], PdNi [16-17] and PdCo [18-21] have been been reported, which can increase ORR activity. Graphene has been extensively studied as an alternative support to enhance nanoparticle catalyst activity and durability owing to its high surface area, high conductivity, high stability, and strong interaction [22-28]. Doping graphene with heteroatoms such as nitrogen also has been demonstrated to significantly enhance the ORR activity of carbon based electrodes to facilitate the charge transfer and electrode-electrolyte interactions [29]. The benefit of doping nitrogen on reduced graphene oxide (rGO) support [30-32] has been suggested to interaction with Pd. Furthermore, the ternary nanoparticles show reduced OH adsorption energies and improved activity for the oxygen reduction reaction (ORR) compared to pure Pt nanoparticles [33].

Carrera-Cerritos et al. [34] has already studied the Pd nanobars and Pt nanoparticles deposited for comparison both on commercial carbon and reduced graphene oxide (rGO). The ORR activity order is as follows Pt/C > Pt/rGO > Pd/rGO > Pd/C. Ejaz and Jeon [35] has shown the ORR performance of Pd/N-rGO is better than Pd/rGO. Sun et al. [36] investigated ternary PdNiM (M = Cu or Sn) supported on nitrogen doped graphene (NG) used as nanocatalysts for the ORR in an alkaline electrolyte. The oxygen reduction performance of the catalyst shows 20% commercial Pt/C > PdNiSn/NG > PdNiCu/NG > 20% commercial Pd black > PdNi/NG > NG. Alloy transition metal nanoparticles consisting of Pd have been considered as the one best alternative electrocatalysts to replace Pt-based catalysts for ORR.

Although many researchers observed the transition metals addition are used for alloying Pd, but there are no reports the transition metals addition to make ternary alloy with Pd based nanoparticles supported on nitrogen-doped reduced graphene oxide (N-rGO). In this research, ternary PdM (M = Fe, Ni, Co) alloys are loaded on N-rGO by three methods. The first method is microwave-hydrothermal method to synthesize N-rGO, the second method is emulsion method to synthesize ternary Pd-M nanoparticles, and the third method is rota-evaporation to distribute ternary Pd-M nanoparticles supported on N-rGO.

1.2 Scope Problems

The problems are discussed in this work including:

1. What is the effect of carbon based material to support ternary Pd-M nanoparticles on morphologies, structures, and ORR activities of the catalysts?
2. What is the effect of transition metals addition for ternary Pd-M nanoparticles supported on carbon based material on morphologies, structures, and ORR activities of the catalysts?
3. What is the effect of the best catalyst on methanol oxidation and durability?

1.3 Research Objectives

This research focuses on three themes including:

1. To observe the effect of carbon based material to support ternary Pd-M nanoparticles on morphologies, structures, and ORR activities of the catalysts.
2. To observe the effect of transition metals addition for ternary Pd-M nanoparticles supported on carbon based material on morphologies, structures, and ORR activities of the catalysts.
3. Observed the effect of the best catalyst on methanol oxidation and durability.

1.4 Research Advantages

The best ternary Pd-M supported on carbon based material can be applied as cathode catalyst in AEMFC application that exhibit higher activity, methanol tolerance, and durability.

– An intentionally blank page –

CHAPTER II

LITERATURE REVIEW

2.1 Fuel Cell

Fuel cell is electrochemical devices which convert the chemical energy of a reaction directly into electrical energy. The principle physical structure of a fuel cell consists of an electrolyte layer in contact with a porous anode and cathode on either side (Figure 2.1) [37].

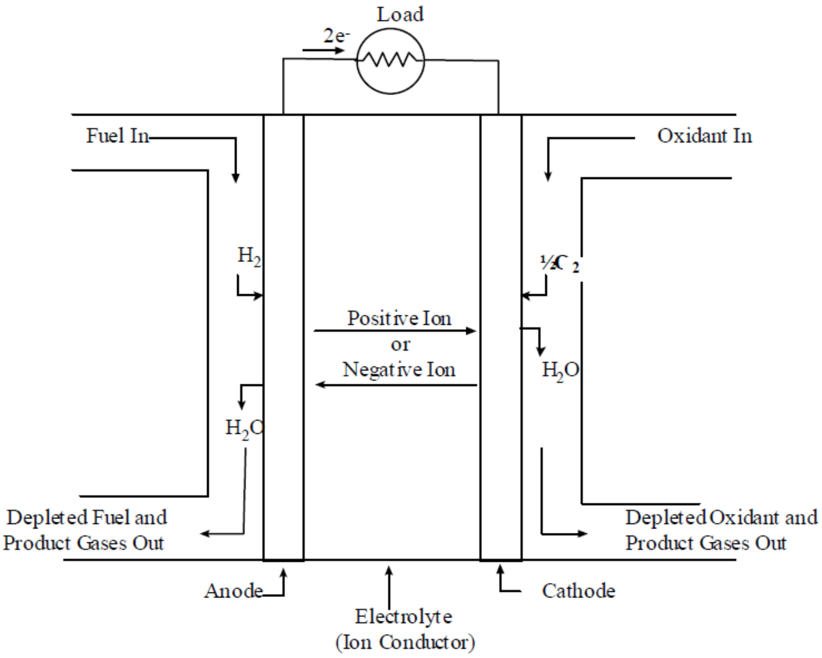

Figure 2.1 Schematic of a fuel cell [37]

Fuel cell systems are not limited by Carnot cycle efficiency. Therefore, a fuel cell system with a combined cycle has very high efficiency about 55 - 85% as compared to the efficiency of current power generation systems about 30 - 40%. In a distributed generation system, fuel cells can reduce costly transmission line installation and transmission losses. There are no moving parts in a fuel cell and very few moving parts (compressors, fans, etc.) in a fuel cell system. Therefore, it has higher reliability compared to an internal combustion or gas turbine power plant [38].

During its evolution, there are many fuel cell unit configurations were proposed, based on different electrolyte and electrode materials, catalysts and operation temperatures. Presently, there are six major fuel cell types: Alkaline fuel cell (AFC), Molten Carbonate fuel cell (MCFC), Phosphoric Acid fuel cell (PAFC), Proton Exchange Membrane fuel cell (PEMFC), Solid Oxide fuel cell (SOFC) and Direct Methanol fuel cell (DMFC). However, the popularity of PEMFCs, a relatively new type of fuel cell, is rapidly outpacing that of the others [39].

2.2 Electrochemical Reactions in Fuel Cell

At the surfaces of the two electrodes, two electrochemical reactions take place. At the anode, over which hydrogen gas passes, occurs the HOR. At the cathode, over which oxygen or air passes, occurs the ORR. The two electrode reactions are as follows [40]:

Anode Reaction:

$$H_2 \rightarrow 2H^+ + 2e^- \quad (2.1)$$

It is corresponding to an anode potential $E°_a = 0.00V$ (under standard conditions) versus SHE.

Cathode Reaction:

$$1/2O_2 + 2H^+ + 2e^- \rightarrow H_2O \quad (2.2)$$

It is corresponding to a cathode potential $E°_c = 1.229V$ (under standard conditions) versus SHE.

Therefore, the overall reaction of the fuel cell follow:

$$H_2 + 1/2O_2 \rightarrow H_2O \quad (2.3)$$

It is the equilibrium standard electromotive force calculated to be 1.229V.

2.3 Anion Exchange Membrane Fuel Cell

Alkaline fuel cell (AFC) is an electrochemical device that can convert the chemical energy of H_2 directly inito an electrical current. In principle, the direction of the reactions at the electrodes in the reserve of that in alkaline water electrolysis. AFCs use a liquid electrolyte solution of potassium hydroxide (KOH) because it is the most conducting of all alkaline hydroxides. AFC offers some advantages over other fuel cells, such as that they are easier to operate at low temperature (23-70°C) [41]. The fuel cell reaction for a traditional AFC and a hydrogen-fuelled alkaline membrane fuel cell are described below [42-43]:

Anode: $2H_2 + 4OH^- \rightarrow 4H_2O + 4e^-$ (2.4)

($E_a = 0.83$ V vs. SHE at 1 bar, 298.15 K)

Cathode: $O_2 + 2H_2O + 4e^- \rightarrow 4OH^-$ (2.5)

($E_c = 0.40$ V vs. SHE at 1 bar, 298.15 K)

Overall: $2H_2 + O_2 \rightarrow 2H_2O$ + energy + heat (2.6)

($E_{cell} = 1.23$ V at 1 bar, 298.15 K)

One of the main problems of the AFC is related to the use of the liquid electrolyte [43-45]. The KOH solution is very sensitive to the presence of CO_2. A major operating constraint is therefore the requirement for low CO_2 concentrations in the feed oxidant stream. When air is used instead of oxygen, the hydroxyl ions may react with CO_2 contained in the air [44, 46] and form K_2CO_3 according to the following reaction:

$CO_2 + 2OH^- \rightarrow CO_3^- + H_2O$ (2.7)

and/or

$CO_2 + 2KOH \rightarrow K_2CO_3 + H_2O$ (2.8)

The main cause of the decreasing performance on carbonate formation is the precipitation of large metal carbonate such as K_2CO_3 (equation 2.5). This reaction decreases the number of hydroxyl ions available for reaction at the anode. If the electrolyte is highly concentrated, carbonate precipitation may block the pores of the gas diffusion layer [38]. Another disadvantage is the amount of liquid electrolyte, if the liquid is in excess or if there is a lack, it leads to electrode to electrode flooding or electrode drying. Since then, many research have focused on the promising development of an AFC based on anion conducting polymer electrolytes to replace the KOH solution, called as Anion Exchange Membrane Fuel Cell (AEMFC), which mechanism in Figure 2.1 [47-48]. Technically, AEMFC are similar to PEMFC, with the difference being that the solid membrane is in alkaline AEM instead of an acidic PEM. With an AEM in an AEMFC, the OH^- anion is transported from the cathode to the anode (Figure 2.2), opposite to the H^+ conduction direction in a PEMFC. Although in principle both technologies are similar, the use of AEM creates an alkaline pH cell environment, therefore the AEMFC offers advantages over the PEMFC technology which is following [49].

- Enhanced oxygen reduction catalysis, allowing for the use of less expensive, Pt-free or precious group metal (PGM)-free catalysts;
- Extended range of cell and stack materials stable in the fuel cell environment;
- A wider choice of fuels in addition to pure hydrogen; and
- A wider range of less expensive polymer chemistry (fluorinated raw materials are not necessary).

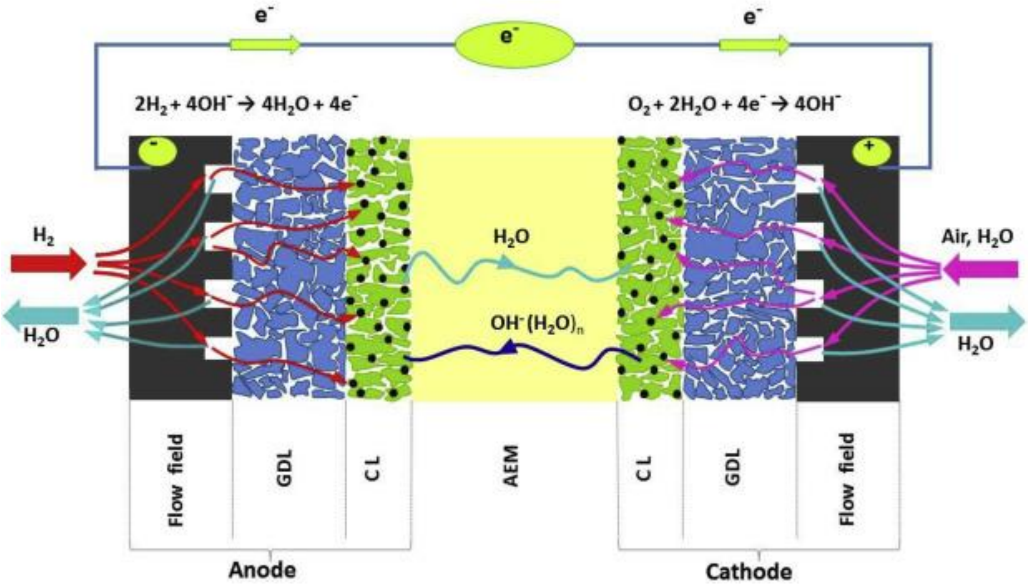

Figure 2.2 Schematic diagram of an H_2-AEMFC and the main species transported through the cell [49]

2.4 Palladium-based Catalayst for ORR

One of the primary interested for the use of the electrocatalysts in fuel cells is the development of high performance cathode catalysts to reduce the high overpotential that is present during the oxygen reduction reaction (ORR). Regarding for fuel cell operation, carbon-supported platinum (Pt/C) catalyst has well known as the best material for cathode catalyst fuel cell application due to high ORR performance. However, Pt catalyst materials are limited reserve, high cost, and instability of the fuel cell operating condition [3]. Therefore, numerous strategies have been employed.

There are some criteria of material selections to replace Pt as cathode catalyst such following [50-51]:

- Good catalyst must have optimal mass transport because hydrogen and oxygen gasses transverse porous layer to reach active sites during fuel cell operation. Active area depend on metal particle size and metal dispersion on carbon supported.
- Flooding water caused by not suitable pore size. Porous supports exhibit higher water sorption. Water is a great conductor but the accumulation of water in electrode lead flooding cell that block gasses access.
- Reducing thickness of catalyst layer can minimized mass transport losses. The balance of surface area losses and mass transport losses must be considered depending on the application.
- Using carbon supports are good conductors of electrons. Carbon supported catalyst particles provide electronic conductivity because it has three phase boundary between gas supply, catalyst particle, and ionic conductors in Figure 2.3.

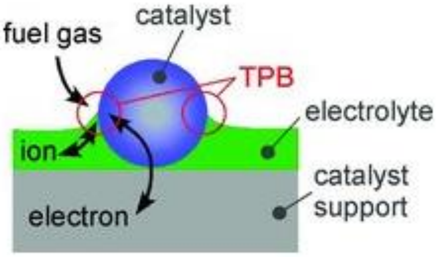

Figure 2.3 The three phase boundary of carbon supported catalyst [51]

Palladium (Pd) exhibits considerable catalytic activity toward ORR, which promotes Pd alloys as feasible alternatives in the development of nonplatinum catalysts with catalytic activity similar to that of Pt. The examination of ORR in alkaline solutions has revealed that Pd exhibits higher activity than in acidic solutions due to a decrease in the anion poisoning effect in alkaline solutions [6-9].

In addition, the price of Pd is practically five times lower than the price of platinum.

Carrera-Cerritos et al. [34] has already synthesized Pd nanobars and Pt nanoparticles deposited for comparison both on commercial carbon and reduced graphene oxide (rGO) by the same method. The TEM images inidicate that the Pt catalysts on commercial carbon are composed of irregularly spherical shape, while the Pd catalysts had square shape nanoparticles similar to nanobars or nanorods, which is shown in Figure 2.4 (a and b). On the other hand, the Pd nanoparticles in the Pd/rGO catalyst have a mixture of irregular and square shapes, which is shown in Figure 2.4 (d). The differences in size and shape indicate that rGO plays a different role during the nanobars formation, perhaps modifying the nucleation and reduction which are influence for the undirectional growth. This is determined by the presence or absence of carbon functional groups on the surface which may act as anchoring centers as nucleation sites.

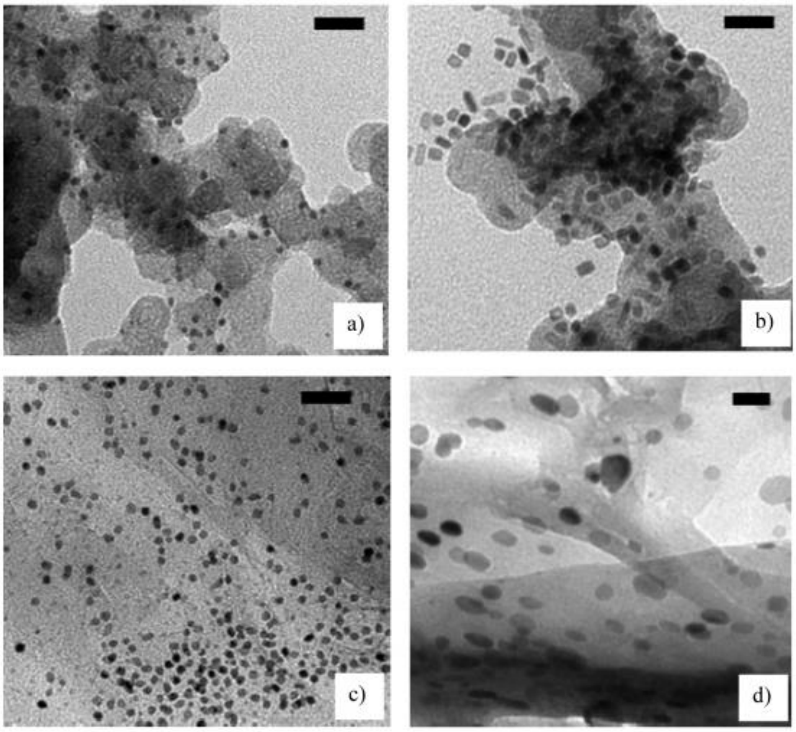

Figure 2.4 The TEM images of (a) Pt/C, (b) Pd/C, (c) Pt/rGO, and (d) Pd/rGO with scale bar 20 nm [34]

They [34] also has shown the ORR performance of Pd nanobars and Pt nanoparticles and deposited for comparison both on commercial carbon and reduced graphene oxide (rGO) can be shown in Figure 2.5. The ORR activity order is as follows Pt/C > Pt/rGO > Pd/rGO > Pd/C. Considering the interesting graphene properties in Figure 2.5 [22-28], the superior electro activity would be expected from the graphene based catalyst compared to carbon based. It shows the graphene supported Pd had higher electrocatalytic activity than Pd/C, it is also the same reported [6, 52]. The enhanced ORR activity of Pd/rGO was attributed to the tensile strain effect when Pd contacted graphene, which resulted in the electron exchange transfer between Pd and graphene interfaces and increased the interaction states and transmission between Pd and graphene while keeping sufficient π electrons on graphene for conduction [52]. However the ORR performance of Pt catalyst supported on rGO has shown lower performance than the Pt catalyst supported on C. It was believed that the ORR diffusion limiting currents were strongly affected by the structure of the catalyst supporting material. The sheet structure of graphene, with small particles entrapped within the fold of these foils, might be block oxygen compared with spherical carbon black particles. Thus, flat structures of graphene may be less effective for nanosized Pt particles than the spherical structure of carbon blacks which randomly distributed in the catalyst layer [34].

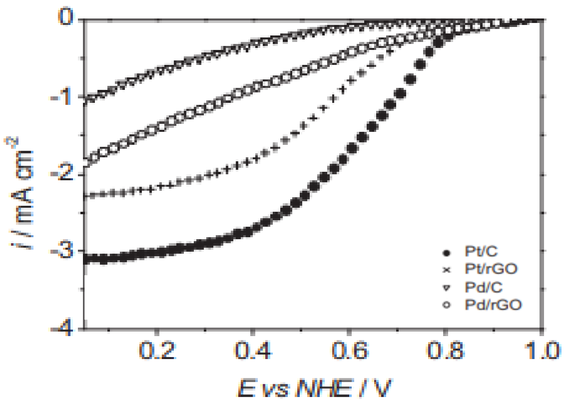

Figure 2.5 The RDE curves of the synthesized catalysts at 1200 rpm [34]

The benefit of doping nitrogen on reduced graphene oxide (rGO) support [30-32] has been suggested to interaction with Pd. Ejaz and Jeon [35] has shown the ORR performance of Pd/N-rGO is better than Pd/rGO which is shown in Figure 2.6. They has investigated through linear sweep voltammetry (LSV) on a glassy carbon RRDE in O_2-saturated 0.1 M KOH at 1600 rpm. They also has written down comparison of the electrochemical activity between the prepared Pd catalysts in Table 2.1. The number of electrons transferred on Pd/rGO and Pd/N-rGO catalyst were close to 4 showing the dominance of a direct four electron pathway ORR performance and they wrote down the reaction in equation 2.9. The illustration of a difference between direct $4e^-$ and $2x2e^-$ ORR pathways are shown in Figure 2.7 [53].

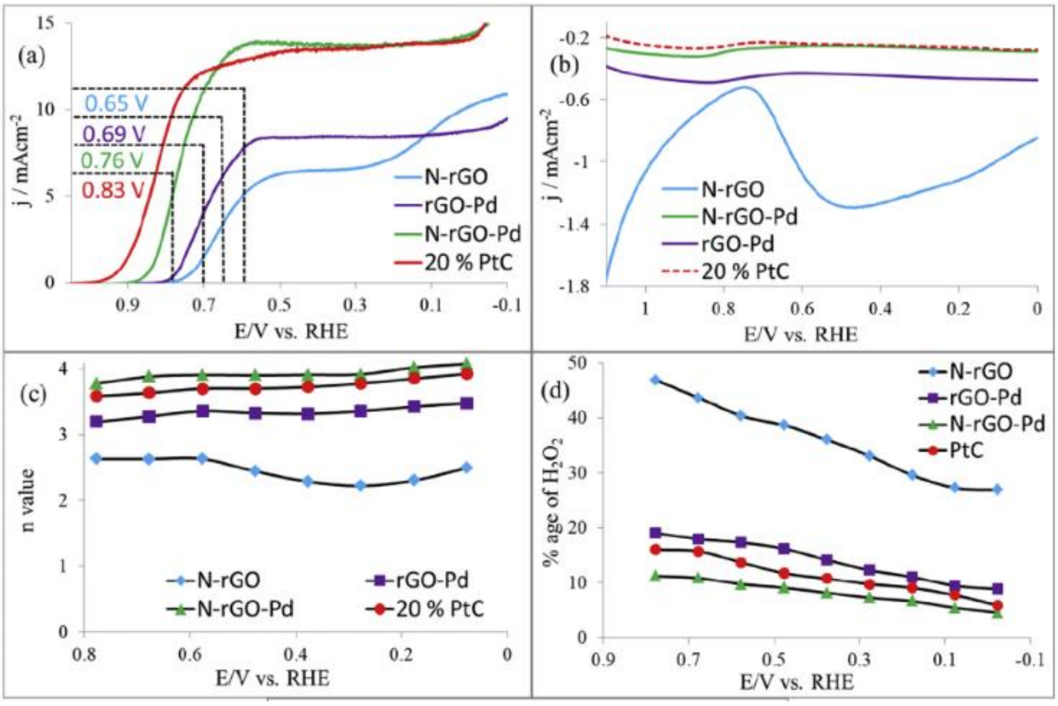

Figure 2.6 The RRDE curves of N-rGO, Pd/rGO, Pd/N-rGO, and Pt/C at 1600 rpm in O_2-saturated 0.1 M KOH solution (a) disk current (b) ring current (c) the corresponding transferred electron numbers (d) H_2O_2 production [35]

Table 2.1 The electrochemical activity between the prepared Pd catalysts [35]

Properties	Pd/rGO	Pd/ N-rGO
Onset potential (V vs. RHE)	0.827	0.912
Half-wave potential (V vs. RHE)	0.69	0.76
n value	3.4	3.91
H_2O_2 (%)	20	<10

$$O_2 + 2H_2O + 4e^- + \rightarrow 4OH^- \quad (2.9)$$

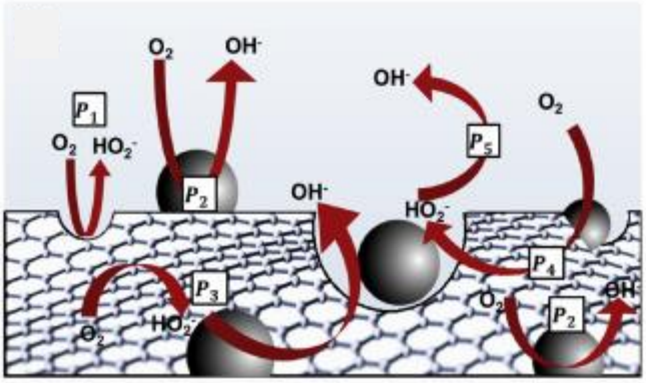

Figure 2.7 The illustration The illustration of a difference between direct 4e- and 2x2e- ORR pathways [53]

2.5 Palladium-based with Transition Metals for ORR

Palladium (Pd) represents an attractive alternative candidate for the ORR in alkaline media because Pd is more abundant and less expensive than Pt, also in alkaline media, has a higher activity [6-9]. Pd and Pt have similar properties (same group of the periodic table, same fcc crsytal structure, similar atomic size) [54]. The developments to ehanced activity by alloying with transition metals (M), like Co, Fe, and Ni. The positive effect of Co presence is the decrease in metal particle size with increasing Co content in the PdCo/C catalyst, thus increasing ORR activity [18, 55]. The effect of addition Fe has also been extensively investigated, Tarasevich et al. [56] explained that the occurrence of iron can influence catalyst activity in two ways : (i) through the stabilization of palladium nanoparticles, despite the high temperature of pyrolysis during the synthesis of the catalyst, and (ii) through hindering oxide-palladium formation.

The role of metal transition to contribute some effects of electrocatalyst was shown in Figure 2.8. Liu et al. [57] has compared the influenced of metal transition supported on nitrogen dopen carbon xerogels in acid solution. From the figure clearly shows that ORR activity is greatly affected by the metal type. Fe-NCX exhibit the best activity, with an ORR onset potential is 0.823 V, followed by Co-NCX and also Ni-NCX. The Fe-NCX displays higher onset potential along with increase diffusion limited current density due to the high amount and uniform distribution of ORR active sites on the catalyst surface [58].

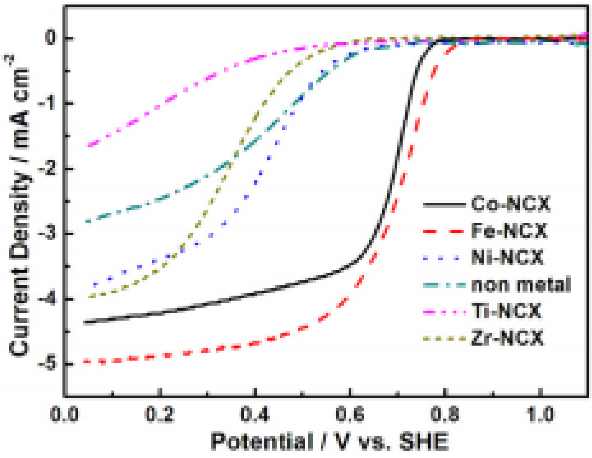

Figure 2.8 The RDE curves of M-CNX catalysts in O_2-purged 0.5 M H_2SO_4 solution with 1600 rpm and scan rate of 5 mV/s [57]

Sun et al. [36] investigated ternary PdNiM (M = Cu or Sn) supported on nitrogen doped graphene (NG) used as nanocatalysts for the ORR in an alkaline electrolyte. The oxygen reduction performance of the catalyst in Figure 2.9 shows 20% commercial Pt/C > PdNiSn/NG > PdNiCu/NG > 20% commercial Pd black > PdNi/NG > NG. The half-wave and current density of catalysts were shown in Table 2.2. The catalytic performance of ternary PdNiSn has the highest result compared others. It can be investigated that the ternary Pd-based catalyst can give more advantages than binary Pd-based catalyst, which not only reduced the level of Pd but also greatly improved the catalytic activity [59-60].

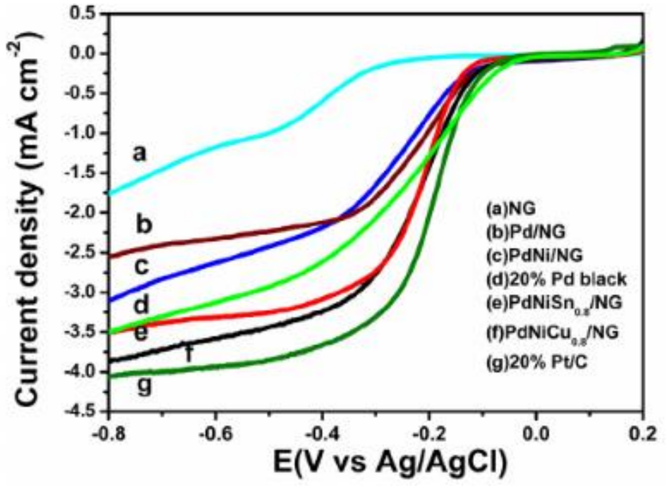

Figure 2.9 The ORR polarization of NG, PdNi/NG, PdNiSn/NG, PdNiCu/NG, 20% commercial Pd black, and 20% commercial Pt/C at 1600 rpm in O_2-saturated 0.1 M KOH [36]

Table 2.2 Electrocatalytic activities of the NG, PdNi/NG, PdNiSn/NG, PdNiCu/NG, 20% commercial Pd black, and 20% commercial Pt/C in 0.1 M KOH at a scan of 20 mV/s [36]

	Half-wave/V	Current density/mA cm^{-2}
NG	-0.400	1.750
PdNi/NG	-0.255	3.120
PdNiSn/NG	-0.210	3.880
PdNiCu/NG	-0.210	3.503
20% commercial Pd black	-0.235	3.501
20% commercial Pt/C	-0.193	4.110

2.6 Graphene

Graphene sheets are a few atoms thick but are nonetheless stable under ambient conditions, metallic, and remarkably high qulity [61]. Since Novoselov et al. [61] and Stankovich et al. [41] have recently achieved some valuable and cheaper methods of preparing graphene sheets for mass production usage, the probability of employing graphene sheets for ordinary application has been increased. Many researches on the mechanical and electrical properties of the graphene sheets have been conducted all over the world. The exceptional electronic properties of graphene and its formidable potential in various applications, have ensured a rapid growth of interest in this new material [62]. Graphene is the key material in the current nanotechnology revolution and the ideal material for the fabrication of functional devices finding applications in electronics, plasmonics, sensors, supercapacitors, energy generation and storage, like batteries, solar cells, and fuel cells [63]. Especially in fuel cell applications, graphene has been extensively studied as an alternative support to enhance nanoparticle catalyst activity and durability owing to its high surface area, high conductivity, high stability, and strong interaction [22-28].

A graphene crystal is an infinite 2D layer consisting of sp^2 hybridized carbon (Figure 2.10), which belongs to one of the five 2D Bravais lattices called the hexagonal (triangular) lattice. Graphene was initially considered as a theoretical building block used to describe the graphite crystal, and to study the formation of the carbon nanotubes (rolled graphene sheets), and predict their fascinating electronic properties [64].

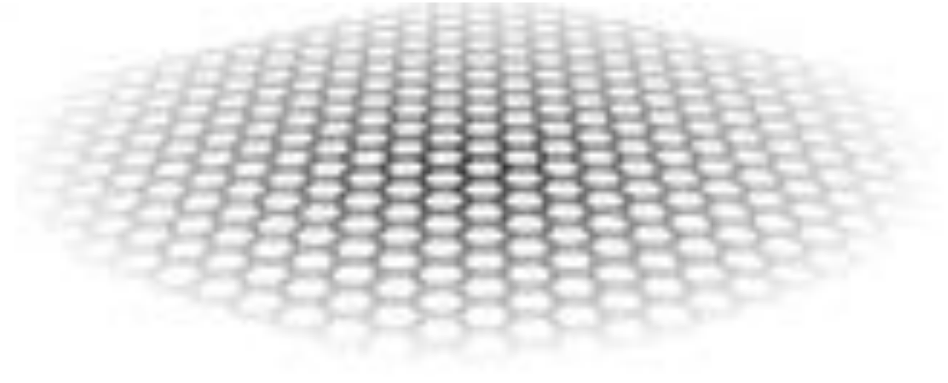

Figure 2.10 Graphene surface [64]

Many fascinating properties were discovered through the investigation of pristine graphene including extremely high charge (electrons and holes) mobility

(230,000 cm^2/Vs) with 2.3% absorption of visible light, thermal conductivity (3000 W/mK), the highest strength (130 GPa), and the highest theoritical spesific surface area (2600 m^2/g) [65]. Chaudhary et al. [66] has compared the properties between graphene and other different carbons (Table 2.3).

Table 2.3 Properties of Different Carbons [66]

	SWCNT	MWCNT	Graphene
Conductivity (S/m)	10^2	10^5	10^8
Melting point (K)	3800 (graphite)		
Tensile strength (GPa)	22.2 + 2.2	11-63	
Thermal conductivity (x 10^{-3} W/mK)	1.75-5.8	3	3-5
Temperature coefficience of resistance (x 10^{-3}/K)	< 1.1	-1.37	-1.47
Mean free path at room temperature	10^3	2.5 x 10^4	10^3
Maximum current density (A/cm^2)	10^9	10^9	10^8

2.6.1 Structure and Morphology of Graphene

Graphene is defined as a single layer of carbon atoms arranged in a hexagonal lattice, as illustrated in Figure 2.11. The primitive cell of graphene is composed of two non equivalent atoms, A and B, and these two sublattices are translated from each other by a carbon-carbon distance a_{c-c} = 1.44 Å. A single carbon atom has four valence electrons with a ground-state electronic shell configuration of [He] $2s^2$ $2p^2$ [67].

In graphene, the chemical conding of carbon atoms are caused by the superposition of 2s with $2p_x$ and $2p_y$ orbitals. The planar orbital forms σ bonds which is stable with neighboring carbon atoms in the honeycomb lattice, affects the bonding energy and elastic properties of the graphene sheets. While the $2p_z$

orbital produces π bonds with neighboring atoms, thus affects the electronic properties of graphene [68]. This phenomenon is shown in Figure 2.12.

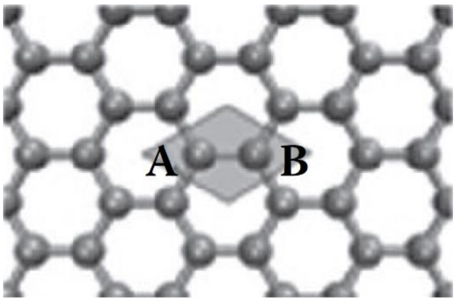

Figure 2.11 Honeycomb lattice of graphene [67]

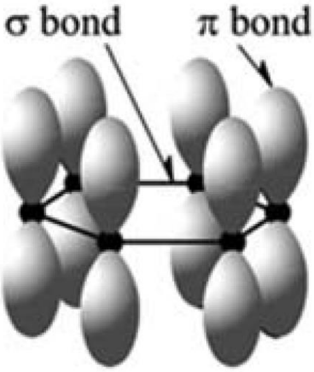

Figure 2.12 The bonding structure of σ bonds and π bonds in graphene [68]

Xu et al. [69] has shown the morphology of pristine graphene (PG) at low and high magnification, respectively. As shown, the PG shows a plane structure with some graphene sheets stacking to graphite platelets due to the strong Van der Waals forces among individual graphene nanosheets. Furthermore, the microstructures of PG were investigated by transmission electron microscope (TEM), as shown in Figure 2.13 (a). It can be observed that PG shows a multilayer graphene structure with some graphene sheets stacking to graphite platelets in Figure 2.13 (b). The selected area electron diffraction (SAED) result indicates that PG has a polycrystal structure, and the inner circle is brighter than outer circle in inset of Figure 2.13 (c), demonstrating that PG is composed of multilayer graphene sheets.

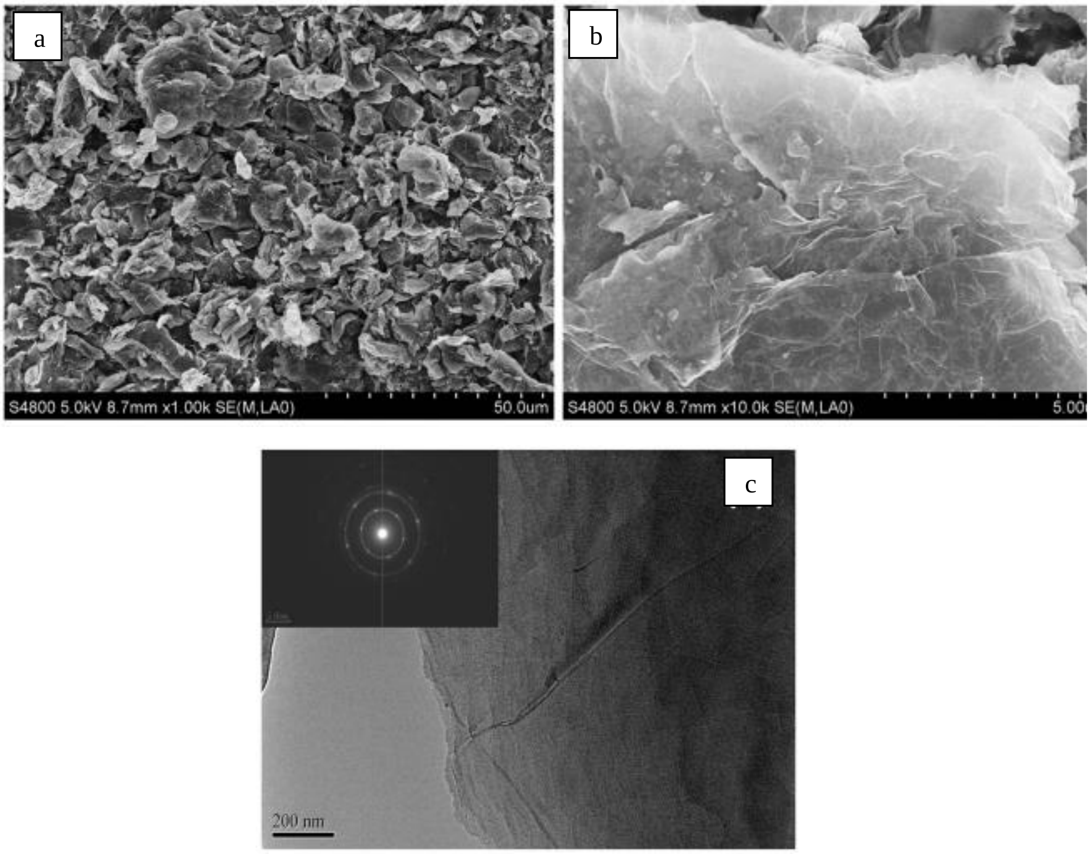

Figure 2.13 (a,b) The SEM images at different magnification of the pristine graphene and (c) The TEM images of pristine graphene inserts of SAED patterns [69]

In addition to characterize the structure of graphene, Xu et al. [70] has shown different XRD patterns of graphite, GO, and self-assembled graphene. From Figure 2.14 can be observed the interlayer spacing of the freeze dried self-assembled graphene was calculated to be 3.76 Å. This value is much lower than of GO precursor (6.94 Å) while slightly higher than that of natural graphite (3.63 Å). These result indicates the existence of π-π stacking between graphene sheets and also the presence of residual oxygenated groups [71]. The broad XRD peak of the freeze dried self-assembled graphene indicates the poor ordering of graphene sheets along their stacking direction and reflects that it is composed of few-layer stacked graphene sheets [69].

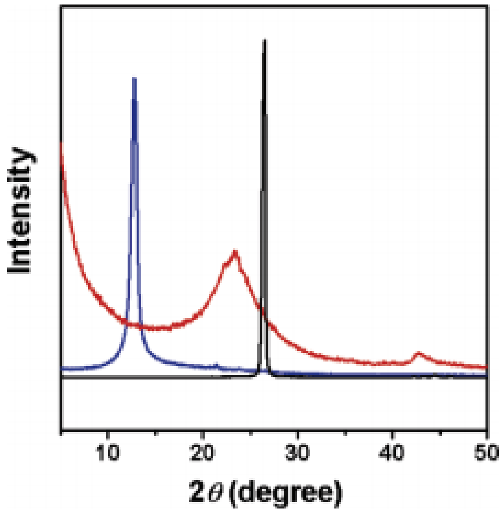

Figure 2.14 The XRD patterns of natural graphite (black), GO (blue), and freeze-dried self-assembled graphene (red) [70]

For further characterization the structure of graphene, raman spectroscopy is useful for studying disorder and defects in crystal structure, it is often employed to characterize graphite and its derivatives. Disorder is determined by the intensity ratio between the disorder induce D band and the raman allowed G band (I_D/I_G). Perumbilavil et al. [72] has shown the raman spectra of GO, reduced graphene oxide, and the base material graphite are shown in Figure 2.15. The G band is common for all sp^2 carbon forms, and it arises from the C-C bond stretch. This band is formed from first order raman scattering [73]. The D band in GO is broadened due to the reduction in size of the sp^2 domains by the creation of defects, vacancies, and distortions during oxidation [74]. The increase of I_D/I_G from graphite to GO confirms the grafting of oxygen containing functional groups to the graphitic planes. During reduction, the D band intensity is reduced, but not so much as in graphite. After reduction, I_D/I_G of rGO decrease which indicates the removal of most of the oxygen containing functional groups. I_D/I_G ratio in rGO is higher than that of graphite because the sp^2 domains which are newly formed during reduction are smaller than those of graphite [72].

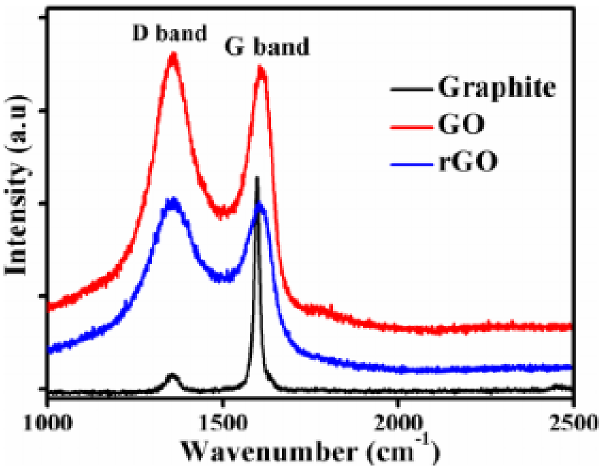

Figure 2.15 Raman spectra of graphite, GO, and rGO [72]

2.6.2 Electrochemical Activity of Graphene

Cyclic voltammetry is employed to measure the rGO samples at a stagnant GCE working electrode, permitting observation of any capacitive effect without adjustments from the flow of electrolyte to the electrode surface. Hayes et al. [75] show a comparison of the anodic and the cathodic current response during cyclic voltammetry analysis of the bare GCE, untreated graphite, graphene oxide (GO), and graphene oxide reduced (rGO) in distilled water by hydrothermal method. The current detected during cyclic voltammetry analysis in O_2-, air-, N_2-saturated 0.1 M KOH electrolyte are compared for each sample preparation. The rGO DI H_2O sample at about -0.312 V provides a cathodic current of 13.67 Ag^{-1} in O_2-saturated KOH, 14.67 Ag^{-1} in air-saturated KOH, and 13.47 Ag^{-1} in N_2-saturated KOH electrolyte. Although the current may change slightly from catalysis at the developed rGO surface in response to variation in the dissolved O_2 of the electrolyte, there is a reliable pseudocapacitance that is not modified significantly which is shown in Figure 2.16 (c). From the Figure 2.16, there is no distinctive capacitive behaviour for the graphite and the graphene oxide. A possible explanation for the redox peaks is the presence of carbonyl-containing oxygen groups on the surface of the reduced graphene oxide, promoting a redox behaviour during voltammetric analysis.

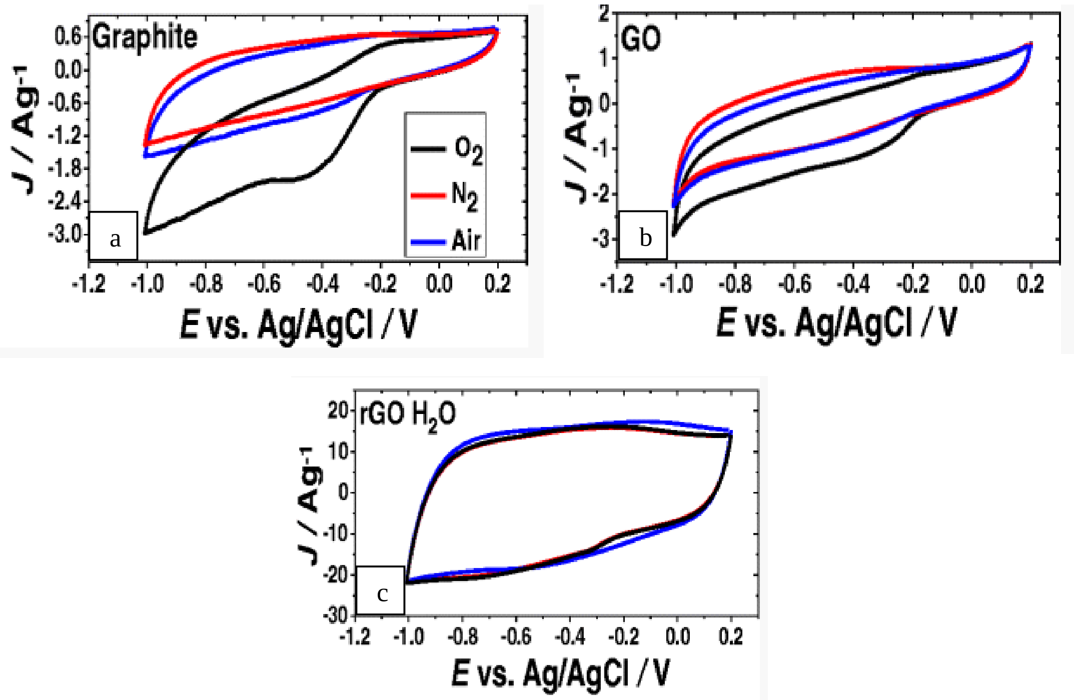

Figure 2.16 Cyclic voltammetry measured in O_2-saturated, N_2-saturated, and air-saturated 0.1 M KOH of (a) graphite, (b) GO, and (c) graphene oxide reduced (rGO) in H_2O [75]

Figure 2.17 shows the LSV analysis of the rGO in comparison to the current generated from the starting graphite material, graphene oxide and polished GCE disc. This indicates a capacitive contribution to the overall cathodic current response from analysis in O_2-saturated 0.1 M KOH. The first step of ORR shows an initial current maximum at approximately −0.5 V for the GCE, graphite, graphene oxide and rGO DI H_2O samples analysed. This first ORR current step correlates with the current produced by the first two electron reduction of oxygen (equation 2.1) [53].

$$O_2 + H_2O + 2e^- \rightarrow HO_2^- + OH^- \tag{2.10}$$

$$HO_2^- + H_2O + 2e^- \rightarrow 3OH^- \tag{2.11}$$

The second stage of ORR (equation 2.11) involves the reduction of the perhydroxyl radical and water to hydroxide anions [54]. The additional slight increase in cathodic current at approximately −0.7 V, most apparent for LSV scans of the GCE, graphite, graphene oxide and rGO DI H_2O sample (Figure 2.17) correlates to this second step in ORR catalysis (equation 2.11). This second reaction onset would not be clearly observable where the ORR is close to or comprises of a single four electron reaction step [76].

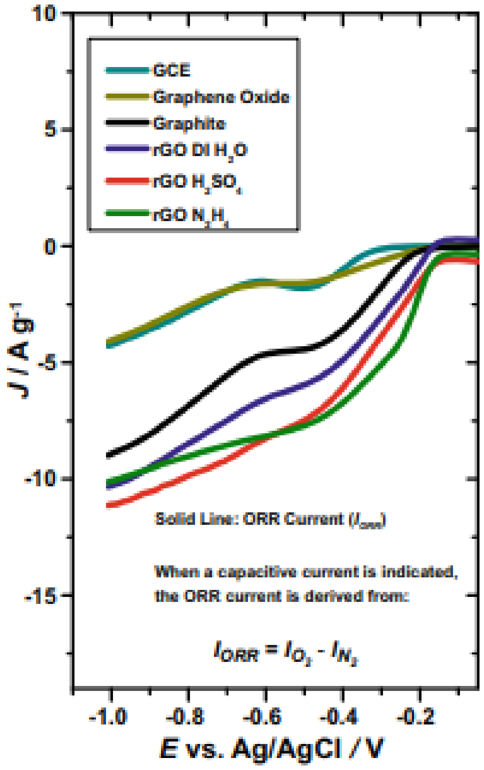

Figure 2.17 ORR performances in O_2-saturated 0.1 M KOH of GCE, grahite, graphene oxide, and graphene oxide reduced (rGO) in H_2O [75]

2.7 Nitrogen doped Graphene

Graphene with theoretically superior physical and chemical properties has been proposed as a promising electrode material for energy devices, such as solar cells, supercapactitors, secondary batteries, and fuel cells [77-79]. Doping graphene with heteroatoms (e.g., N, P, S, and B) has been demonstrated to significantly enhance the surface hydrophilicity of carbon based electrodes to facilitate the charge transfer and electrode-electrolyte interactions [29]. Among the heteroatom, nitrogen doping is considered as one of the prominent effective methods for improving the chemical reactivity of graphene correlated with the stronger electronegativity of nitrogen atom relative to that carbon, and the propounding conjugation between the lone pair electrons of nitrogen and π-electrons of the graphene [80-81]. The concept behind the ORR activity of N-doped graphene lies in the difference between electronegativities of carbon (χ = 2.55) and nitrogen (χ = 3.04) which polarizes the carbon-nitrogen bonds [82-83]. As a consequence, the induced positive/negative charges in the adjacent carbon atoms facilitate oxygen adsorption and its subsequent reduction. It also has been reported that the nitrogen doped carbon nanostructures show n-type or metallic behavior and are expected to have greater electron mobility than their corresponding un-doped carbon nanostructures [84].

2.7.1 Structure and Morphology of N-doped Graphene

It is widely estabilshed that incorporation of nitrogen atoms into the matrix of sp^2-bonded carbon can lead to the appearance of different kinds of nitrogen impurities. For graphene, it was found that mainly three types of bonding may occur: (i) direct substitution (graphitic N), (ii) the pyridinic configuration, and (iii) the pyrrolic structure. A variety of possible configurations of the nitrogen impurities in graphene has shown in Figure 2.18.

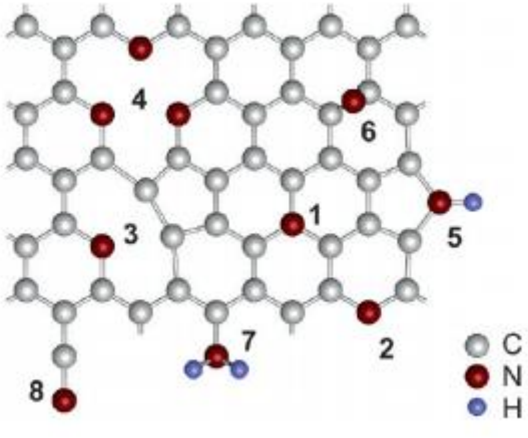

Figure 2.18 Possible configurations of nitrogen impurities in graphene: (1) substitutional or graphitic N, (2) pyridine-like N, (3) single N pyridinic vacancy, (4) triple N pyridinc vacancy, (5) pyrrole-like, (6) interstitial N or adatom, (7) amine, and (8) nitrile [85]

Each of the configurations affects the electronic and transport properties of the functionalized material rather differently. In the graphitic configuration, three nitrogen valence electrons form three σ-bonds, one electron fills the π-states, and the fifth electron enters the π*-states of conduction band, providing a strong n-doping effect. However, the situation becomes more complicated for pyridinic and pyrrolic environments, and the implication of the simple tight-bonding model does not predict any charge transfer effect for such impurities [85].

Qu et al. [86] has shown the morphology of nitrogen-doped graphene oxide in Figure 2.19 (a-d) which characterized by TEM. An electron diffraction of the N-graphene in Figure 2.19 (a) shows a ringlike diffraction pattern with dispersed bright spots. The above observed difference indicates that the otherwise crystalline graphene became partially misoriented in the N-graphene due to structure distortions caused by the intercalation of nitrogen atoms into its graphitic plans. The cross sectional of the suspended edge of as-synthesized N-graphene shows only a few layers (typically 2-8 layers) of graphene sheets which can be seen in Figure 2.19 (b-d). The interlayer distances in the N-graphene were measured to be 0.3-0.4 nm , close to the d-spacing of (002) crystal plane (0.335 nm) of bulk graphite with slight distortion [87]. Raman spectra of the as-synthesized N-graphene sheets with different layer numbers are given in 2.19 (e). It revealed a relatively higher D-band for the N-graphene due to structural distortion caused by N-doping. While the very low value of 0.06-0.25 for the I_D/I_G indicates that the N-graphene layers remain a high crystalline quality [88].

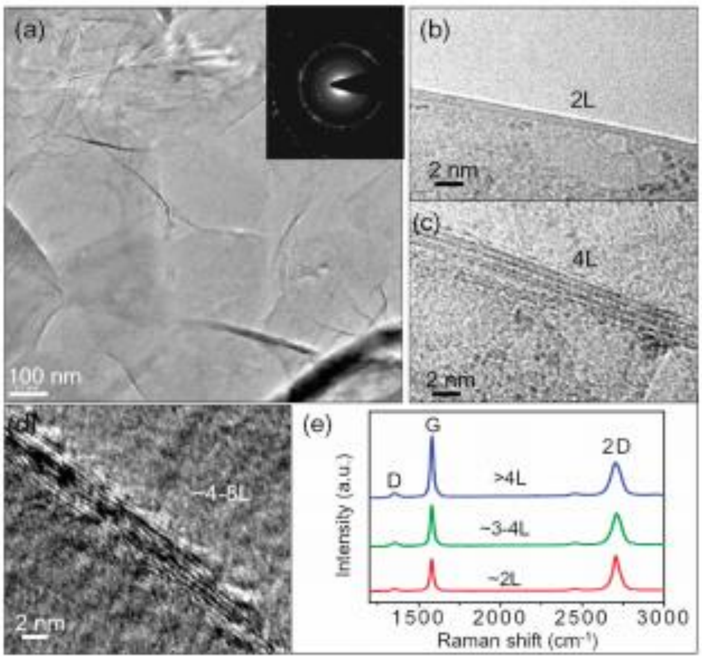

Figure 2.19 (a-d)TEM and (e) Raman analyses of the N-graphene [86]

Sun et al. [88] has shown the SEM image in Figure 2.20 (a) of three-dimensional (3D) porous nitrogen-doped grapheen sheets (NGS) with stacked and overlapped structures The TEM image in Figure 2.20 (b) also showed NGS with a structure of stacked and wrinkled nanosheets. Meanwhile, NGS was estimated to be composed of 8 layers based on the analysis of the HRTEM image which is shown in Figure 2.20 (c). The XRD patterns of the original GO and NGS were observed in Figure 2.20 (d). The diffraction peak located at 2θ = 10.1° is attributed to the (002) crystalline plane of GO and the corresponding calculated interlayer spacing is about 0.87 nm. However, the peak at 2θ = 10.1° disappeared after hydrothermal reaction, and a broad diffraction peak around 25° of the graphite (002) plane was observed for the synthesized NGS sample, indicating the reduced sample was composed of few-layer stacked graphene nanosheets. Besides, the interlayer distance was reduced from 0.87 nm of GO to 0.36 nm of NGS, which indicated the recovery of π-conjugated system after the reduction of GO [89-90].

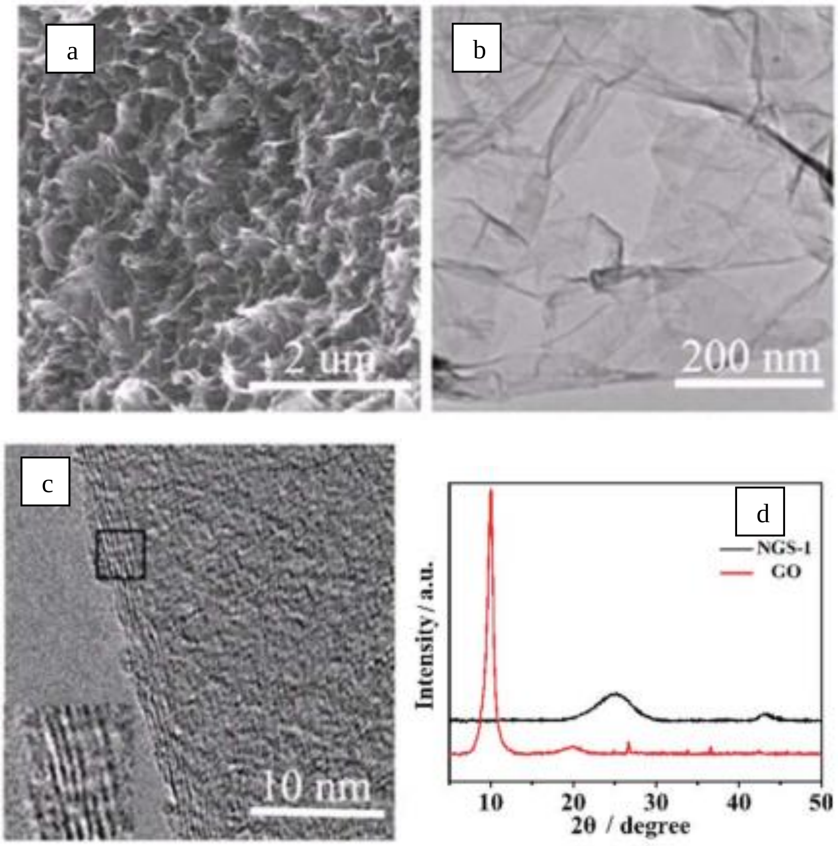

Figure 2.20 (a) SEM, (b)TEM and (c) HR-TEM of the N-graphene [88]

For further characterization to analyze the elemental compositions and nitrogen bonding configurations in nitrogen-doped graphene (NGH), Guo et al. [91] has shown by XPS analyses. The peaks at about 284.6 and 532.1 eV can be indicated as the binding energies of C1s and O1s, respectively. As shown in Figure 2.21 (b), the O1s peak of nitrogen-doped graphene became significantly weak and the C1s peak became much stronger as compared with GO which is shown in Figure 2.21 (a), suggesting a considerable increase in C/O atomic ratio. In addition, N1s peak at 399.2 eV and an additional peak at 285.9 eV corresponding to the C-N bonds were observed in the XPS survey scan spectra and C1s spectra of NGH. The N1s signal of NGH can be split into three peaks at 398.1 (pyridinic N), 399.6 (pyrrolic N), and 401.6 (graphitic/quaternary N) were located inset in Figure 2.21 (b).

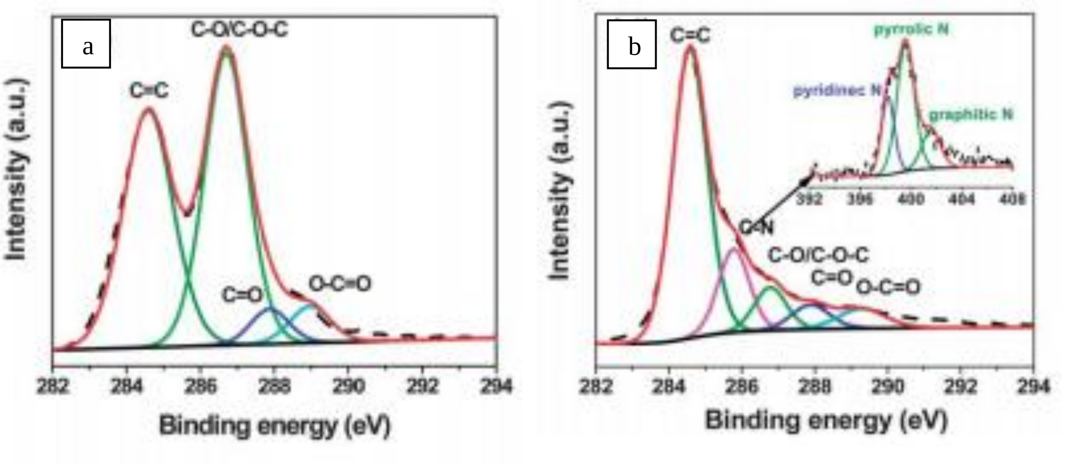

Figure 2.21 XPS survey scan spectra of (a) GO and (b) Nitrogen-doped graphene [91]

2.7.2 Electrochemical Activity of N-doped Graphene

Lu et al. [30] has shown the cyclic voltammetry of graphene oxide (GO), reduced graphene oxide (ErGO), and nitrogen-doped reduced graphene oxide (NrGO) in Figure 2.22 (a). As can be seen, the onset potential of ORR for the GO is at -0.18 V (versus AgCl) with the cathodic reduction peak at around -0.40 V (versus AgCl). After electrochemical reduction of GO both the onset potential and the ORR reduction peak potential shifted positively to -0.11 V and -0.26 respectively. These results clearly demonstrate a significant enhancement in the ORR electrocatalytic activity for the ErGO with respect to the graphene oxide electrode. Compared with GO, the ErGO shows a dramatically increased capacitance similar to NrGO, this is mainly related to the increased conductivity of the material. The heteroatom (nitrogen) doping can increase the electronic conductivity of the carbon materials due to pseudo-capacitance contribution in Figure 2.22(a) in comparison with the non-doped ones [31-32]. The change in shape of the CV curves demonstrates the increase of the non-Faradaic currents induced by the increase in effective surface area of the electrically conductive graphene that is generated by the reduction of GO. The ORR performance which is shown in Figure 2.22 (b) shows for the GO and ErGO, a clear reduction pre-wave was observed at low overpotentials, followed by a second reduction wave starting at around -0.7 V, which is indicative of a prevalent 2e$^-$ reduction pathway.

The absence of the peak in the LSV curve of NrGO at -0.7 V whih is shown in Figure 2.22 (b) suggests that NrGO has a more efficient oxygen reduction due to the presence of nitrogen related electrocatalytic active sites for oxygen reduction [30].

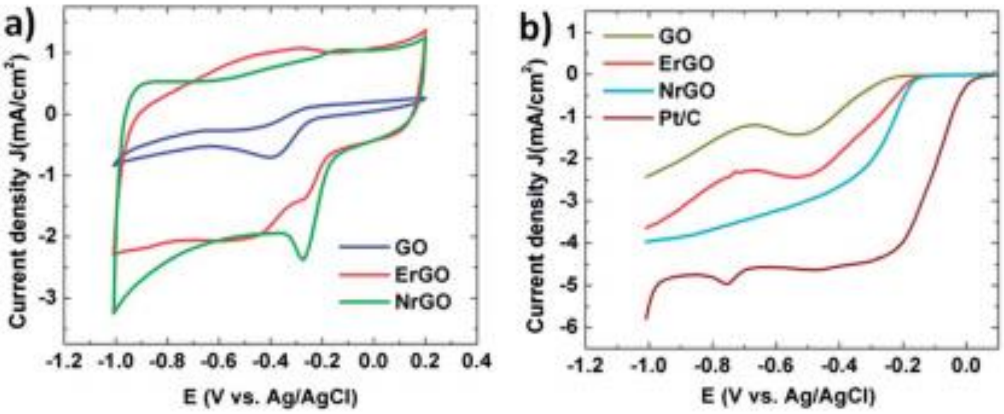

Figure 2.22 The GO, ErGO, and NrGO electrodes for (a) CV curves and (b) RDE curves in O_2 saturated 0.1 M KOH solution [30]

2.8 Influence of Methanol Oxidation

Methanol produces CO_2 on electro-oxidation and carbonate formation (equation 2.7) can be even more of a problem when a methaol fuel cell is operated with a liquid alkaline elctrolyte. The fuel cell equations for the direct use of methanol with an alkaline electrolyte are [42]:

Anode : $CH_3OH + 6OH^- \rightarrow CO_2 + 5H_2O + 6e^-$ (2.12)

(E_a = 0.81 V vs. SHE at 1 bar, 298.15 K)

Cathode : $3/2O_2 + 3H_2O + 6e^- \rightarrow 6OH^-$ (2.13)

(E_c = 0.40 V vs. SHE at 1 bar, 298.15 K)

Overall : $CH_3OH + 3/2O_2 \rightarrow 2H_2O + CO_2$ (2.14)

(E_{cell} = 1.21 V at 1 bar, 298.15 K)

The serious problem methanol used in fuel cells leads to high overvoltage, impacting negatively on the ORR activities [92], generating additional water and increasing the required oxygen stoichiometric ratio [54]. Sa et al. [93] has shown the Pt/C catalyst (Figure 2.23) exhibited a marked change in its ORR polarization curve after the addition of MeOH, indicated by a negative shift of the half-wave potential. Such a change can be influenced to the formation of a mixed potential, where the methanol and oxygen simultaneously react at the surface of the Pt particles.

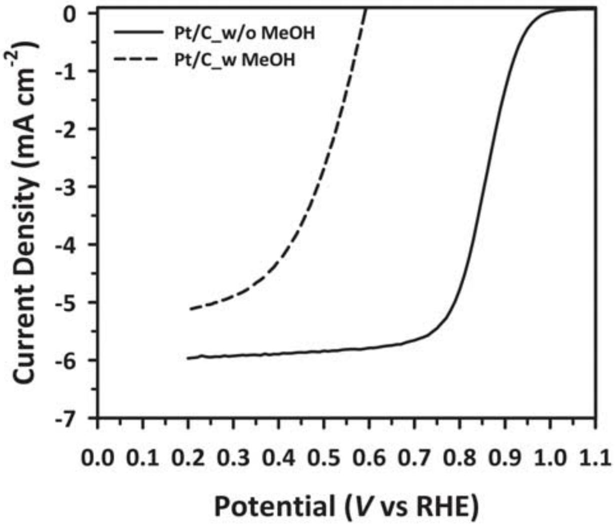

Figure 2.23 ORR polariztaion curves of Pt/C with 0.5 M methanol in 0.1 M KOH electrolyte [93]

The intermediates and reaction products depend synergistically on a number of factors such as electrode potential, catalyst crystallographic features, elemental surface composition, temperature, reaction time, supporting electrolyte, and methanol concentration [40]. Based on this situtation, Ruiz-Camacho et al. [94] show the methanol oxidation catalyst in different electrocatalysts (acid and alkaline) and different concentrations (0.0, 0.3 and 0.5 M) in Figure 2.24. For acid medium in Figure 2.24 (a) it can be observed that the activity of PtAg/C towards the ORR was not affected with the presence of methanol showing excellent properties as tolerance cathode. The three curves obtained were almost the same with and without the presence of methanol. PtAg/C exhibited a minimum mixed potential due to the simultaneous methanol oxidation and oxygen reaction on its surface. Its condisition is contrast with alkaline medium in Figure 2.24 (b), the kinetic region of the PtAg/C as cathode catalyst was drastically affected by the presence of methanol, the onset potential shifted negatively with the increase in methanol concentration. In the general, the rate of ORR depends strongly on the degree of interaction of oxygen molecules with the adsorption sites on the electrocatalyst surface. During the ORR process on an electrocatalyst surface, the oxygen molecules compete strongly with methanol molecules for the adsorption sites in the electrolyte containing methanol [54].

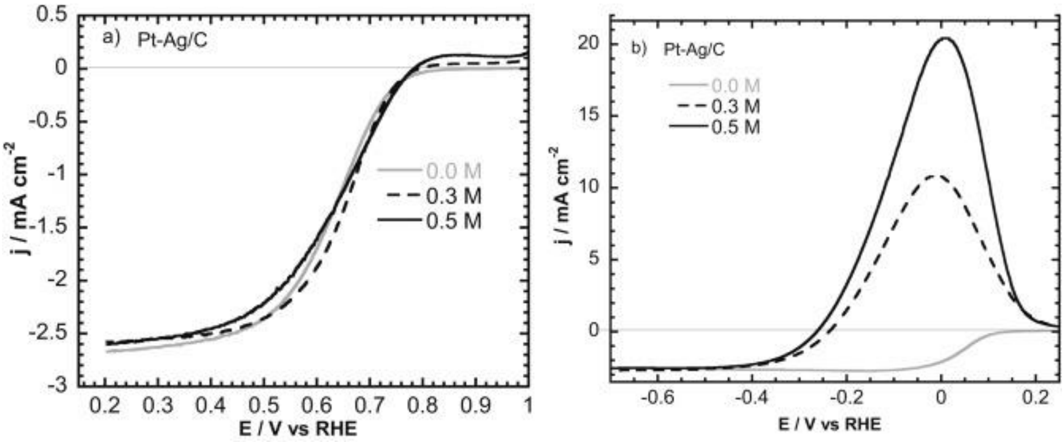

Figure 2.24 Linear sweep voltammetry curves of PtAg/C at 900 rpm in oxygen saturated (a) acid and (b) alkaline [94]

2.9 Emulsion Method

The emulsion method is a novel route for the formation of nanoparticles (NPs). An emulsion is a cloudy colloidal system of micron size droplets of one immiscible liquid dispersed in another, such as oil in water, in the presence of a suitable surfactant and a co-surfactant. An emulsion is form by vigorous stirring or sonication and is thermodynamically stable. Nano size particles can spontaneously form within the micron size water droplets as a thermodynamically stable emulsion. Briefly, in this method the first step is the formation of NP through a water-in-oil emulsion reaction, followed by a reduction step. The surfactant molecules can function as protective agents to prevent the NP from agglomeration. The surfactant molecule can be easily remove by heat treatment. The main advantage of the emulsion method is its controlling metallic composition and particle size with a narrow distribution.

2.10 Emulsion Method

Byrappa and Yoshimura [95] define hydrothermal synthesis as any heterogeneous reaction in an aqueous media carried out at high temperature and high pressure (>100°C, >1 atm) in a closed system. Supercritical water can play the role of reducing agent in hydrothermal conditions and offers a green chemistry alternative to organic solvents. In addition, its physiochemical properties can be changed widely with pressure and temperature. Supercritical water behaves like a water-like fluid with strong electrolytic solvent power, high diffusion coefficient, high ion molecules, and a dielectric constant that can be comparable with that of polar molecules. These properties allow the catalysis of a variety of heterolytic (ionic) bond cleavage reactions in water. Hydrothermal routes have been introduced for remarkable transformation of carbohydrate molecules to form homogenous carbon nanospheres and nanotubes.

The hydrothermal method has several advantages over the common chemical reduction processes: (1) the process requires very simple setup, basically an autoclave; (2) it has good upward scalability and it is industrially compatible with batch processing; (3) it is intrinsically pure because it utilizes only water, as opposed to the hydrazine or sulfonate chemical reduction method which inevitably introduces nanocarbon impurities into the treated GO; (4) the closed system of relative high temperature and internal pressure promote the recovery of π-conjugation after dehydration, which is favorable for minimizing defects, and (5) engineering the parameters of temperature and pressure affords a facile method to control the degree of reduction of the GO [96].

The reaction mechanism under hydrothermal reduction are introduced is shown in Figure 2.25 [97]. The stacked parallel layers in graphite are seperated by spaces, the interlayer is bonded by the van der Waals, through this force is weak enough to ensure the layers slide with each other in the direction perpendicular to the *c*-axis, complete exfoliation form graphite into individual layers is difficult. Therefore, to overcome the van der Waals atteractions between the adjacent layers is necessary. For oxide graphite, the introduction of oxygen-containing functional groups, such as hydroxyl (-OH), epoxy (-CH(O)CH-), and carboxyl groups (-COOH), causes the expansion between neighboring layers. The van der Waals force is inversely proportional to the interatomic separation, which can fasilitates exfoliation significantly because the d-spacing between graphite stacked increased [98]. After reduction, the oxygen-containing functional groups are removed through still exist some with the decreasing basal spacing [97].

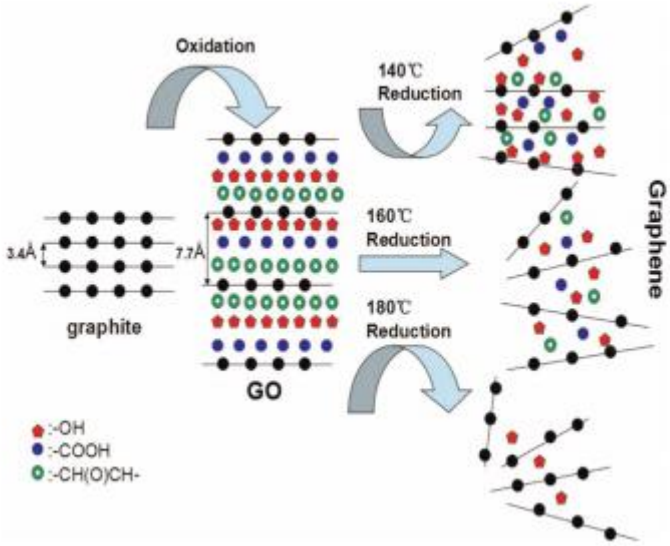

Figure 2.25 The reaction mechanism of structural transition from GO to rGO under hydrothermal condition [97]

– An intentionally blank page –

CHAPTER III

EXPERIMENTAL DETAIL

3.1 Materials

Metal precursors used for catalysts are Pd(acac)$_2$, Fe(acac)$_3$, Co(acac)$_2$, and Ni(acac)$_2$ purchased from New Jersey. Materials selection for experimental were showed in Table 3.1.

Table 3.1 Materials selection for experimental

Chemical Name	Formula	Purity	Phase	Manufacturer
Palladium (II) acetylacetonate	$C_{10}H_{14}O_4Pd$	35%	Solid	Fisher Scientific Across
Iron (III) acetylacetonate	$C_{15}H_{21}O_6Fe$	99+%	Solid	Fisher Scientific Across
Cobalt (II) acetylacetonate	$C_{10}H_{14}O_4Co$	99%	Solid	Fisher Scientific Across
Nickel (II) acetylacetonate	$C_{10}H_{14}O_4Ni$	96%	Solid	Fisher Scientific Across
Urea	CH_4N_2O	99.5%	Solid	Fisher Scientific Across
Benzyl alcohol	C_7H_8O	99%	Liquid	Fisher Scientific Across
Oleic acid	$C_{18}H_{34}O_2$	90%	Liquid	Sigma Aldrich
Oleylamine	$C_{18}H_{37}N$	80-90%	Liquid	Fisher Scientific Across
Toluene	$C_6H_5CH_3$	99.8+%	Liquid	Fisher Scientific Across
Ethyl alcohol	C_2H_6O	99.5%	Liquid	Choneye Pure Chemicals

Benzyl alcohol acts as a reducing agent in presence of oleic acid as a stabilizer and oleylamine as a co-reductant and co-surfactant. Because the presence of reducing reagent and surfactant, toluene and ethyl alcohol were used for washing. N-rGO was used as carbon support in catalysts. Material precursors used for carbon support were urea and commercial graphene oxide. Catalysts formed by catalytic cracking of N-hexane. Distilled water was used throughout this study.

3.2 Experimental Procedurs

3.5.1 Synthesize Nitrogen doped Reduced Graphene Oxide

The nitrogen doped reduced graphene oxide (N-rGO) catalyst was prepared by hydrothermal reaction of GO in the presence of urea with mass ratio 1:300. The experimental process was showed in Figure 3.1.

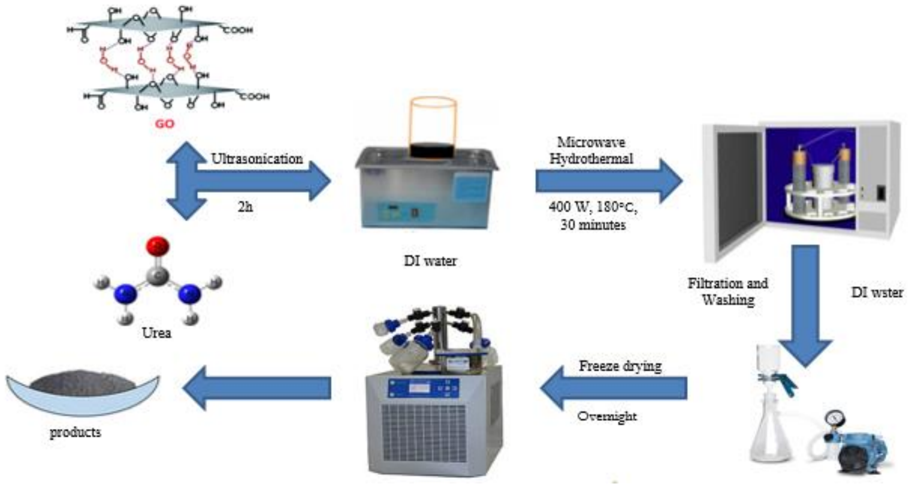

Figure 3.1 Schematic of synthesize nitrogen doped reduced graphene oxide

50 mg of GO was first dissolved in 35 ml of DI water and 15,000 mg of urea was subsequently added. The suspension was ultrasonically treated for 2 hours to achieve homogeneous dispersion. The suspension was then poured into 100 mL Teflon-lined autoclave, sealed and put into microwave hydrothermal to complete hydrothermal reaction at 180°C. After holding 30 minutes, the Teflon-lined autoclave was cooled to room temperature. Finally, the product obtained was

filtered and washed with DI water for several times to remove impurities and freeze dried for overnight. Here, reduced graphene oxide (rGO) has been synthesized by the same method without urea.

3.5.2 Synthesize Ternary Pd-M Nanoparticles

An emulsion method was employed to prepare ternary Pd-M (M = Fe, Ni, and Co) nanoparticles catalysts. To study the effect of different transition metals in ternary alloy catalysts, PdFeNi, PdFeCo, and PdCoNi ternary alloy were prepared with the initial molar ratio 3:1:1. The experimental process was showed in Figure 3.2.

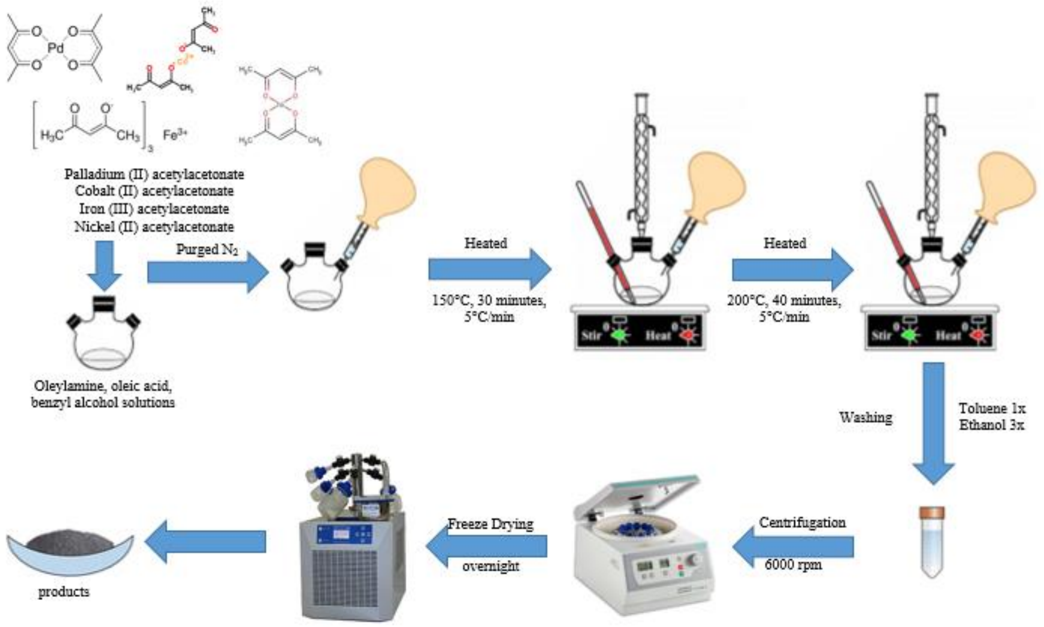

Figure 3.2 Schematic of synthesize ternary Pd-M (M = Fe, Ni, and Co)

In the typical synthesize, the given amounts of metal precursor ($Pd(acac)_2$, $Fe(acac)_3$, $Co(acac)_2$, and $Ni(acac)_2$) powders were dropped into benzyl alcohol as a reducing agent in presence of oleic acid and oleylamine with ratio 2:1. The mixture was purged with nitrogen then heated at 150°C for 30 minutes to reduce the metal precursors. Then the mixture continues heated at 200°C and held for 40 minutes to form alloy. After cooling down to room temperature, the black suspension was dropped in centrifuge tube for washing with toluene one time and ethanol three times. Finally, the black product was collected after centrifuged and freeze dried for overnight. Here, Pd nanoparticle has been synthesized by the same method without transition metal precursors.

3.5.3 Synthesize Ternary Pd-M Nanoparticles Supported N-rGO

The 40 wt% of ternary Pd-M catalysts supported N-rGO were prepared by rotary evaporation. The experimental process was showed in Figure 3.3.

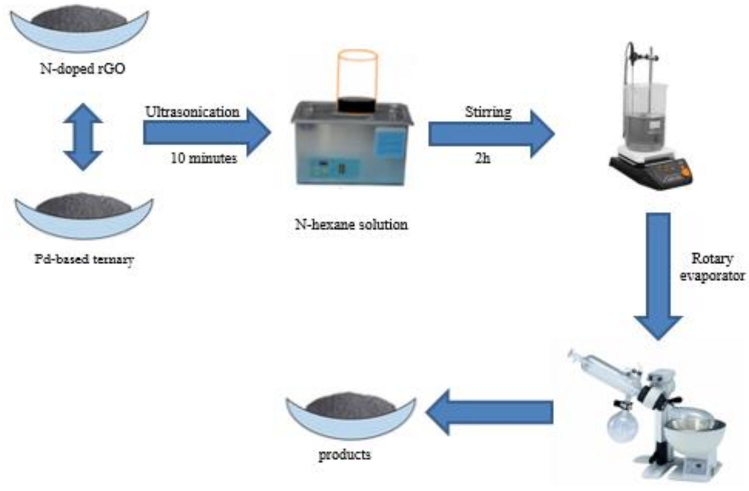

Figure 3.3 Schematic of synthesize ternary Pd-M supported N-rGO

The ternary Pd-M alloy was mixed with N-rGO in 10 mL of N-hexane solution. The solution was sonicated for 10 min to disperse the powder and stirred for 2 hours. Then the solution was put into rotary evaporator machine at 90 hPa of pressure and 40°C of temperature to remove solvent. The black product was collected after the solution evaporated.

3.3 Flowchart of Experimental

The experimental procedure to synthesize nitrogen doped reduced graphene oxide (N-rGO), ternary Pd-M (M = Fe, Ni, and Co) nanoparticles, and 40 wt% of ternary Pd-M catalysts supported N-rGO are explained by the flowcharts which shown in Figure 3.4, Figure 3.5, and Figure 3.6 respectively.

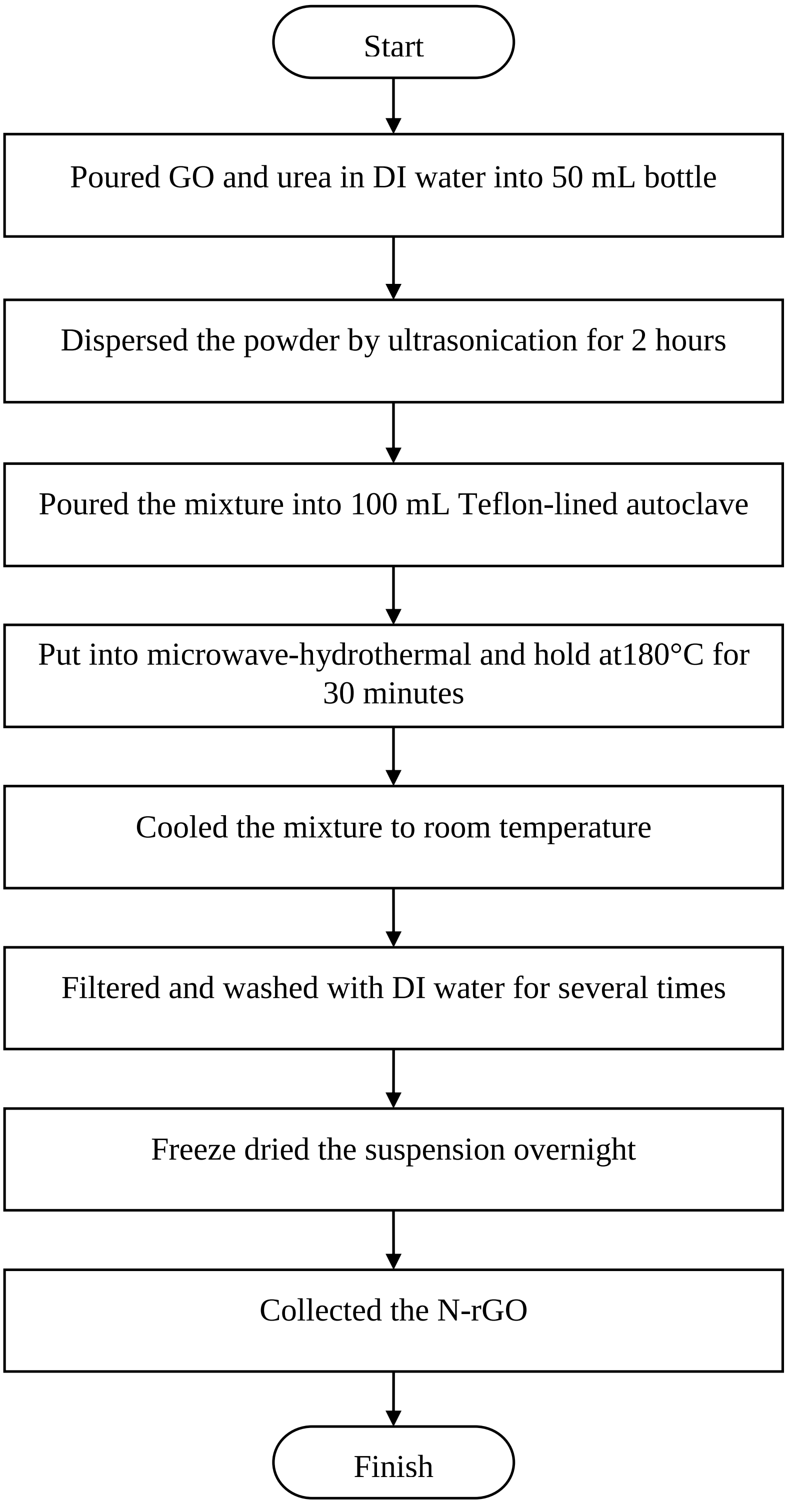

Figure 3.4 Flowchart of synthesize nitrogen doped reduced graphene oxide

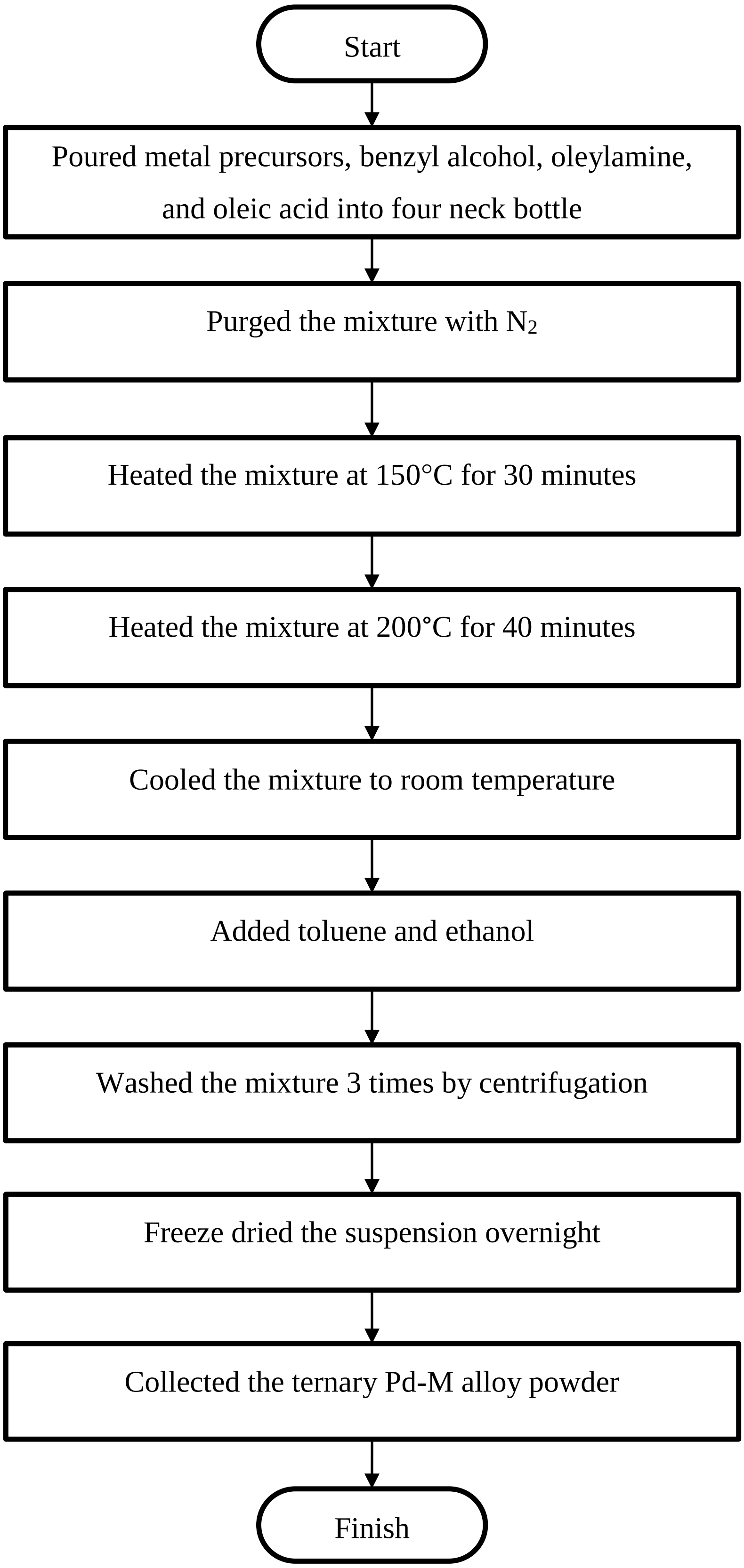

Figure 3.5 Flowchart of synthesize ternary Pd-M (M = Fe, Ni, and Co)

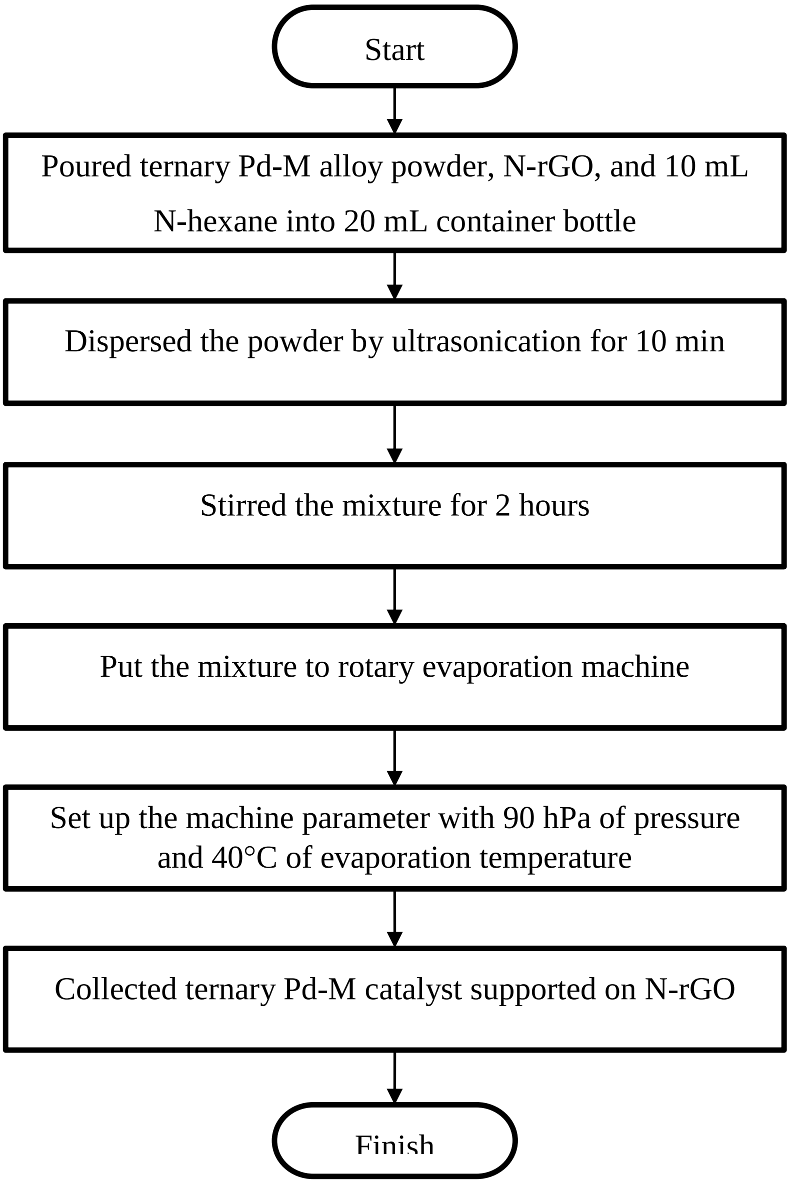

Figure 3.6 Flowchart of synthesize 40 wt% of ternary Pd-M supported N-rGO

3.4 Experimental Matrix

In this work, two variables have been studied about material catalysts, including different carbon based and different alloying metal on Pd based which is shown in Table 3.2.

Table 3.2 Experimental matrix of research

Variables	Precursors	Catalysts
Carbon based	GO	rGO
	GO Urea	N-rGO
Pd based	$Pd(acac)_2$	Pd
	$Pd(acac)_2$ $Fe(acac)_3$ $Co(acac)_2$ $Ni(acac)_2$	PdFeNi PdCoNi PdFeCo

3.5 Materials Characterization

3.5.1 Synthesize Nitrogen doped Reduced Graphene Oxide

X-Ray Diffraction (XRD) is a technique for the study of crystal structures and atomic spacing of material. These X-rays are generated by a cathode ray tube, filtered to produce monochromatic radiation, collimated to concentrate, and directed toward the sample. The interaction of the incident rays with the sample produces constructive interference when conditions satisfy Bragg's Law. From Bragg's Law equation (3.1), an estimated number of lattice parameter can be calculated.

$$n \lambda = 2d_{hkl} \sin \theta \tag{3.1}$$

n represents the reflection order, λ is the wavelength (in nanometers), d_{hkl} is interplanar distance between two planes with Miller indices hkl, and θ is the incident angle of X-rays.

The grain size of particle, τ, is estimated from the half-height width of the diffraction peak (111) using the Scherrer equation (3.2).

$$\tau = \frac{k \lambda}{\beta \cos \theta} \tag{3.2}$$

τ is the grain size (in nanometers), λ is the wavelength (in nanometers), β is the full width at half-maximum FWHM) (in radians), k is a constant (0.94 to spherical crystallites) and θ is the diffraction angle.

Some parameter was decided for measurement including of increment angle, 2θ range, scanning time, and rotation angle. For this study, all samples are measured in an angle range 10-80°C using X-Ray Diffraction: Bruker D2 Phaser. The instrument can be seen in the Figure 3.7. The spectra use Cu Kα (λ = 15.406 Å), Ni filter, 40 kV, and 100 mA. Low scanning rate was set with step size of 0.0081° and time of 0.1 second per step.

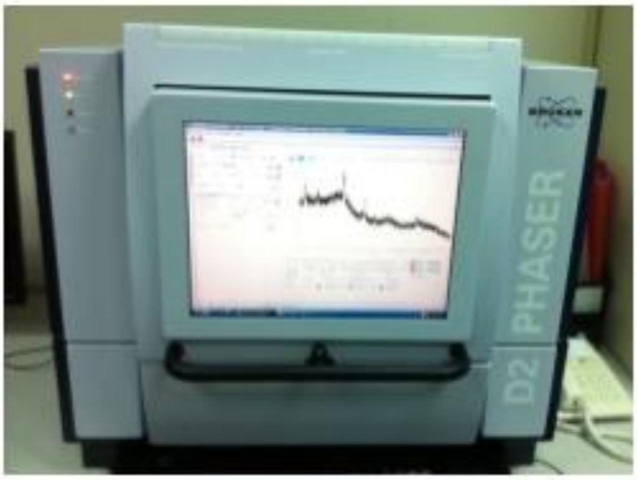

Figure 3.7 X-Ray diffraction: Bruker D2 Phase

3.5.2 Synthesize Nitrogen doped Reduced Graphene Oxide

A field emission scanning electron microscopy (FE-SEM) is microscope that works with electrons (particles with a negative charge) instead of light. These electrons are liberated by a field emission source. The object is scanned by electrons according to a zig-zag pattern. Electrons are liberated from a field emission source and accelerated in a high electrical field gradient. Within the high vacuum column these so-called primary electrons are focussed and deflected by electronic lenses to produce a narrow scan beam that bombards the object. As a result secondary electrons are emitted from each spot on the object. The angle and velocity of these secondary electrons relates to the surface structure of the object. A detector catches the secondary electrons and produces an electronic signal. This signal is amplified and transformed to a video scan-image that can be seen on a monitor or to a digital image that can be saved and processed further.

For preparation step, powder samples are coated by platinum for 60 seconds to avoid charge effect and then observed the image using FE-SEM JEOL JSM 5800 with 10 kV. The FE-SEM machine was shown by Figure 3.8.

Figure 3.8 Field emission scanning electron microscopy: JEOL JSM 5800

3.5.3 Raman Spectroscopy

Raman spectroscopy is spectroscopic technique using monochromatic light based on inelastic scattering, usually from a laser source. The instrument of raman spectroscopy was shown by Figure 3.9.

Figure 3.9 Raman spectroscopy: Jobin - Yvon Lab RAM HR800

Inelastic scattering means that the frequency of photons in monochromatic light changes upon interaction with a sample. Photons of the laser light are absorbed by the sample and reemitted. The shift reveals information about the vibrational, rotational and other low frequency transitions in molecules. The analysis equipment for this experiment is Raman spectrometer (Jobin - Yvon Lab RAM HR800-confocal micro-Raman spectroscopy), determine the ratio of I_g (graphitic intensity) and I_d (disorder intensity).

3.5.4 Field Emission Transmission Electron Microscopy

Field emission transmission electron microscopy (FE-TEM) is a type of microscopy where an electron-transparent specimen which is bombarded with a finely focused (<10 nm diameter) electron beam produced by thermionic emission heating (field emission) and with an acceleration voltage 50-150 kV under vacuum and the intensities of the transmitted electrons are measured.

For preparation step, the sample was dispersed in a polymer solution to form a bulk sample after heat treatment. The samples cut with laser beam, and put on Cu grips. Figure 3.10 shows the FE-TEM machine.

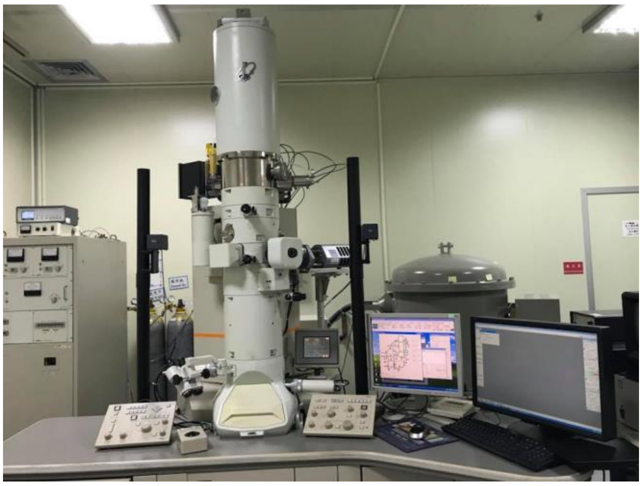

Figure 3.10 Field emission transmission electron microscopy machine

3.5.5 X-Ray Spectrometry

X-Ray photoelectron spectroscopy (XPS, VG ESCA Scientific Theta Probe) using 1486.6 eV Al K-source was used to study the changes of the N 1s, C 1s, Pd

3d, Fe 2p, Co 2p, and Ni 2p of the ternary Pd-based supported on N-rGO catalyst. Figure 3.11 presented the instrument of XPS. The percentage of those elements can be calculated using formula as follow [61-62].

$$\frac{\mathrm{N}c}{\mathrm{N}n} = \frac{\mathrm{A}c/_{Sc}}{\mathrm{A}n/_{Sn}} \qquad (3.3)$$

Notation:

I = Fitted peak surface area

N = atomic content

S = atomic sensitivity factor (ASF)

c = each elements

n = totally elements

Sample preparation of XPS analysis forms the thin powder which was compressed in compression machine. Some catalyst powder was flatted in the electrical tape and compressed in pressure of 26 km cm^{-2} for 300 seconds in room temperature.

Figure 3.11 X-Ray spectrometry instrument

3.6 Electrochemical Measurement

Electrochemical measurements were performed using a three compartment cell via a potentiostat/galvanostat (Biologic VSP Bi-stat). Catalyst ink was prepared by mixing 9.50 mg of the catalyst, 2 ml of isopropanol, and 2 ml of DI water. The ink (20 μL) and 5 μL of 0.1 wt% Nafion® solution were loaded on the GC disk and then left dry to room temperature, with a catalyst loading of 200 μg/cm^2. The CV, RRDE, and methanol oxidation measurements are shown in Figure 3.11.

Figure 3.12 The CV, ORR, and methanol oxidation instrument

3.6.1 Synthesize Nitrogen doped Reduced Graphene Oxide

The cyclic voltammetry (CV) measurement was performed using conventional three electrodes electrochemical cell. The counter and reference electrode were Pt wire and a saturated calomel electrode ($Hg/HgCl_2$ in saturated KCl solution), respectively. The CV measurement was done in 0.1 M KOH solution at a low scan rate of 10 mV/s.

3.6.2 Rotating Ring-Disk Electrode

A rotating ring-disk electrode (RRDE, PINE AFE6R2G-CAU) consisting of a glassy carbon (GC) disk and a gold ring was used as the working electrode. The counter and reference electrodes were Pt ring and a saturated calomel electrode ($Hg/HgCl_2$ in saturated KCl solution). The electrolyte used an oxygen-saturated 0.1 M KOH solution. The ORR curves were scanned at a low scan rate of 10 mV/s to decrease the non-faradaic current from the catalyst and a rotation speed of 1600 rpm. A voltage of 1.1 V vs. RHE to the ring was utilized to produce a current to oxidize the peroxide ions and allow the determination of the hydrogen peroxide ion yield of the ORR on the GC disk.

3.6.3 Methanol Oxidation

The methanol oxidation measurement was performed using the same instrument with ORR, a rotating ring-disk electrode (RRDE, PINE AFE6R2G-CAU) consisting of a glassy carbon (GC) disk and a gold ring was used as the working electrode. The counter and reference electrodes were Pt ring and a saturated calomel electrode ($Hg/HgCl_2$ in saturated KCl solution). The difference located in electrolyte where used 0.1 M KOH containing 0.1 M CH_3OH. The ORR curves were scanned at a low scan rate of 10 mV/s and a rotation speed of 1600 rpm.

3.6.4 Stability Test

To evaluate the durability of catalyst, as-prepared catalysts were carried out by LSV in the potential range of 1 – 0.6 V vs. RHE and the scan rate of 50 mV s^{-1} in N_2-saturated 0.1 M KOH. After 10000 cycles, the ORR was measured at the scan rate 10 mV s^{-1} using speed rotation 1600 rpm for 5 cycles under O_2-saturated 0.1 M KOH. Both of LSV and ORR were measured for three times. The stability test was measured for 30000 cycles using instrument as shown in Figure 3.12. The counter and reference electrodes were carbon rod and a saturated calomel electrode ($Hg/HgCl_2$ in saturated KCl solution).

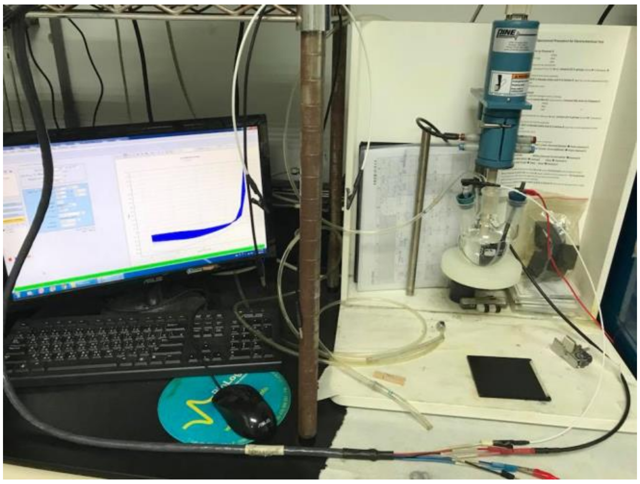

Figure 3.13 Instrument assembly of stability test

CHAPTER IV

RESULTS AND DISCUSSION

4.1 The Effect of Carbon Support

To further maximize the activity of ternary Pd-M electrocatalysts and minimize the usage of Pd, it is very important to disperse ternary Pd-M electrocatalysts with high activities on supports. Using a high surface area support material would not only maximize the reactive surface area of the electrocatalyst for electron transfer but would also provide better mass transfer of the reactants to the electrocatalysts. In this work, reduced graphene oxide has synthesized by microwave hydrothermal method.

4.1.1 X-Ray Diffraction Results

The X-ray diffraction (XRD) patterns of carbon based are shown in Figure 4.1. The interlayer spacing of commercial graphene oxide (GO) was calculated by Bragg's Law equation (equation 3.1) to be 0.792 nm according to the sharp diffraction peak (002) at around $2\theta = 11.15°$ [99]. After microwave hydrothermal, the XRD pattern of reduced graphene oxide doesn't show the sharp XRD peak of GO, while a new broad diffraction peak C (002) is appeared at around $2\theta = 24.47°$ with decreased d-spacing about 0.363 nm. This implied that most of the oxygenated functional groups were removed and reduced to graphene [100-101]. This is indicating the recovery of a graphitic crystal structure. In this work, a microwave hydrothermal reaction to simultaneously doped nitrogen and reduce commercial GO.

After microwave hydrothermal, the XRD pattern of N-rGO is appeared at $2\theta = 25.63°$, corresponding to C (002) with interlayer spacing of 0.347 nm, indicating the addition of urea not only results in nitrogen doping, but also enhances the reduction of GO, as can be proved by the decrease of oxygen content in N-rGO [91]. The higher peak of rGO and N-rGO shift to higher angle indicating the slightly structure changes were occurred after deoxidation and nitrogen doping respectively [102]. The peak position 2ϴ and d-spacing of GO, rGO, and N-rGO can be summarized at Table 4.1.

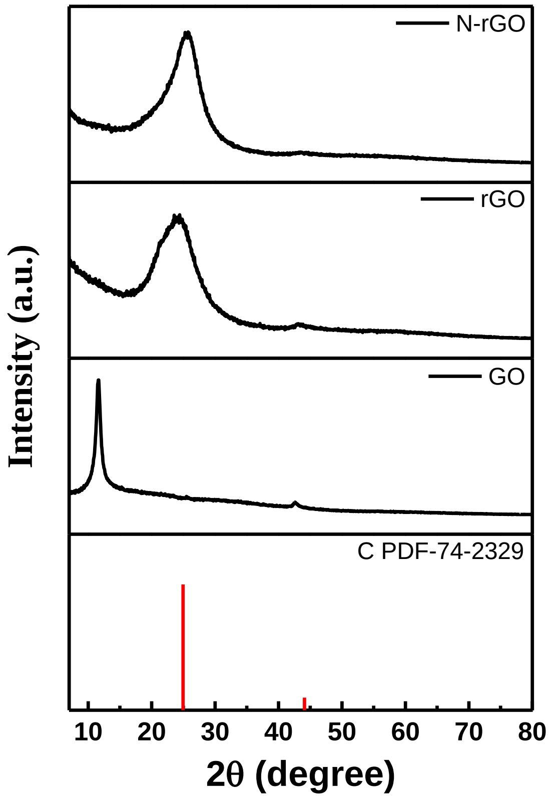

Figure 4.1 XRD patterns of GO, rGO, and N-rGO

Table 4.1 XRD result of GO, rGO, and N-rGO

Sample	Peak position 2ϴ at (002)	d-spacing (nm)
GO	11.15	0.792
rGO	24.47	0.363
N-rGO	25.63	0.347

4.1.2 Raman Spectra

Raman scattering is strongly sensitive to electronic structure and it has been proved to be an essential tool to characterize GO, rGO, and N-rGO, particularly for distinguishing ordered and disordered crystal structures of carbon and carbon heteroatoms. In this work, the two remarkable peaks around 1343.42 and 1596.64

cm^{-1} (Figure 4.2) referred to the D-band and G-band of the graphene sheet [103]. The D-band is assigned to the vibrational mode induced by the disordered structure, meanwhile the G-band is corresponding to the E_{2g} vibration of sp^2-bonded graphitic carbon system [104-105]. Therefore, the ratio of intensities for the D-band and G-band is used to indicate the graphitization degree for the carbon-based materials [106].

In this work (Table 4.2), it can shows that the higher D-band intensity of GO due to the presence oxygen containing functional groups which created some defects, vacancies, and distortions of graphitic planes. Therefore the I_D/I_G of GO is very high. During reduction, the D-band intensity is reduced, which indicates the removal of most of the oxygen containing functional groups [30] and the reduction of GO under hydrothermal conditions tends to decrease the I_D/I_G value to be 1.06 of rGO [107] which is shown in Table 4.2, and also indicating that the recovery of a graphitic crystal structure which is correlated to XRD result.

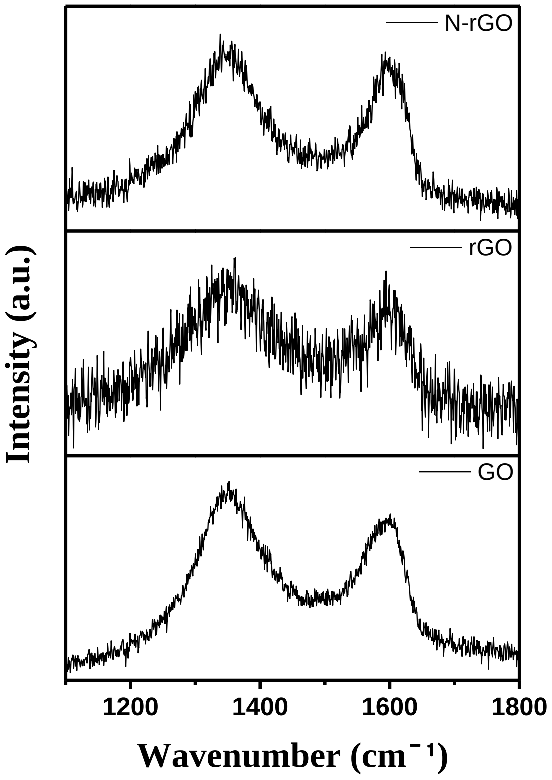

Figure 4.2 Raman spectra of GO, rGO, and N-rGO

Table 4.2 I_G and I_D intesity of GO, rGO, and N-RGO

Catalyst	G-band (cm^{-1})	D-band (cm^{-1})	I_D	I_G	I_D/I_G
GO	1343.42	1596.64	225.87	188.32	1.20
rGO			22.91	21.53	1.06
N-rGO			68.41	59.77	1.14

After nitrogen doping, it caused the formation of more defective sites. Therefore, the increased intensity of the D-band, increasing I_D/I_G to be 1.14 of N-rGO (Table 4.2) indicates the attributed to the strong interaction between carbon and nitrogen which induces disorder in the carbon-carbon rings [108-110]. A decrease in the absolute magnitude of the raman (signal-to-noise of the spectra) which generated low intensity is caused by the presence of nitrogen doped [111]. The almost similar intensity ratio for rGO and N-rGO because of using the same microwave hydrothermal method as synthesized that removes the surface oxygen containing functional groups, therefore no significant difference is found in the Raman spectra [31].

4.1.3 Field Emission Scanning Elctron Microscopy with Energy Dispersive X-Ray Spectroscopy

The field emission scanning electron misroscopy (FE-SEM) images of carbon based has been investigated in Figure 4.3. The FE-SEM images has shown the morphology of GO, rGO, and N-rGO. The morphology of GO is observed as thick layered structures including wrinkled areas in Figure 4.3 (a). GO can be visualized as individual sheets of graphene decorated with oxygen functional groups [112], it is corresponding from energy dispersive X-ray spectroscopy (EDX) analysis is shown in Figure 4.4(a). It revealed the higher content of oxygen about 34.68 atomic%.

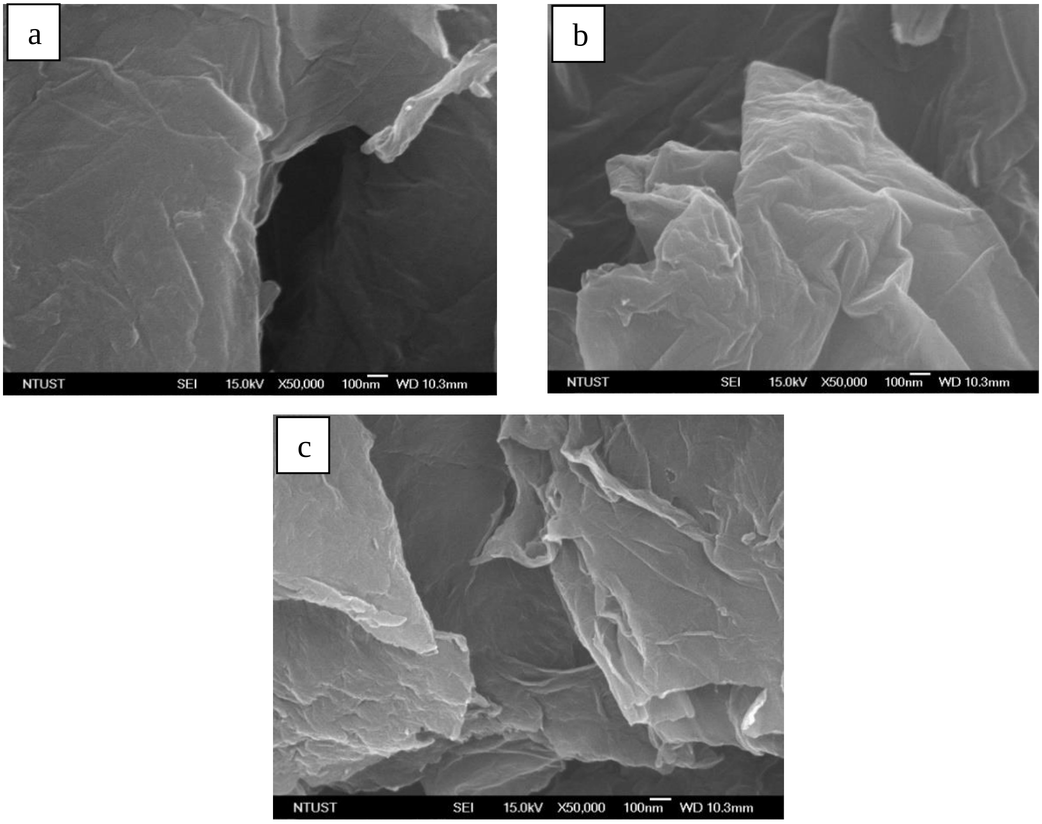

Figure 4.3 FE-SEM images of (a) GO, (b) rGO, and (c) N-rGO

The morphology of reduced graphene oxide is shown in Figure 4.3(b). These images demonstrate thin and wrinkled sheets transparent. Since hydrothermal reduction, the carbon content increases to 90.00 atomic%, which is at the expense of the great decrease of oxygen content. This phenomenon inidicates that the oxygen functionalities have been removed by hydrothermal method [89]. As can be seen in Figure 4.3 (c), the morpholgy of N-rGO is observed as interconnected of graphene sheets and overlapped structures, it is same with previous reported [88-91]. The interconnected with overlapped structures can serve as a buffering reservoir where the reactant can reduce the diffusional path to the interior, leading to higher ORR performance [113]. The synthesis of N-rGO under hydrothermal method with urea is not only nitrogen doped to rGO, but also can act as reducing agent to reduced graphene oxide [91]. It is confirmed with EDX analysis, decreasing oxygen content about 10 atomic% to 6.37 atomic% of rGO and N-rGO respectively in Figure 4.4.

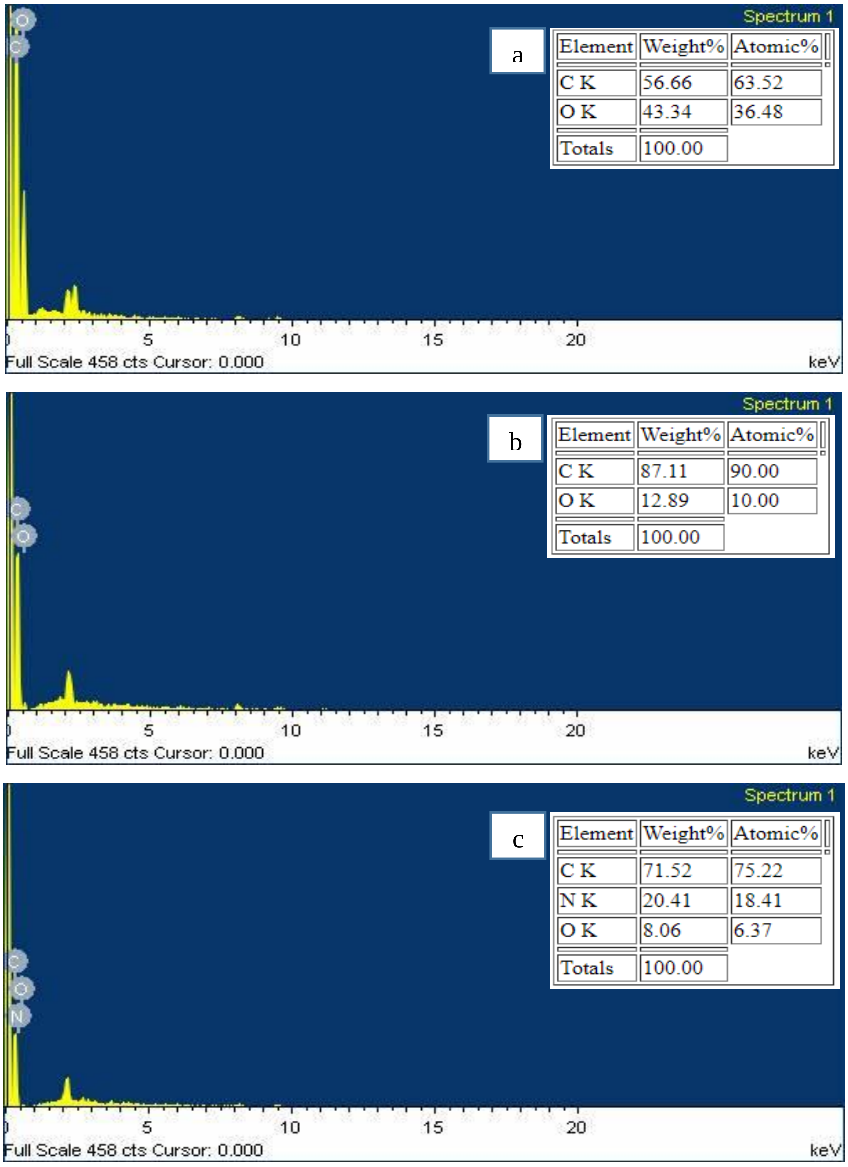

Element	Weight%	Atomic%
C K	56.66	63.52
O K	43.34	36.48
Totals	100.00	

Element	Weight%	Atomic%
C K	87.11	90.00
O K	12.89	10.00
Totals	100.00	

Element	Weight%	Atomic%
C K	71.52	75.22
N K	20.41	18.41
O K	8.06	6.37
Totals	100.00	

Figure 4.4 EDX analysis of (a) GO, (b) rGO, and (c) N-rGO

4.1.4 Cyclic Voltammogram

The cyclic voltammogram (CV) of the GO, rGO, and N-rGO were investigated in 0.1 M KOH solution and it is shown in Figure 4.5. The CV of all samples shown in Figure 4.5 (a) in N_2-saturated 0.1 M KOH do not show any significant peak, it is same with the previous reported [30]. As can be seen in Figure 4.5 (b), the cathodic reduction peak of the GO appeared at 0.61 V (vs. RHE) in O_2-saturated 0.1 M KOH. A very low intense redox peaks appeared in the GO sample, which can be attributed to the presence of oxygen functional goups on the GO sheets [114].

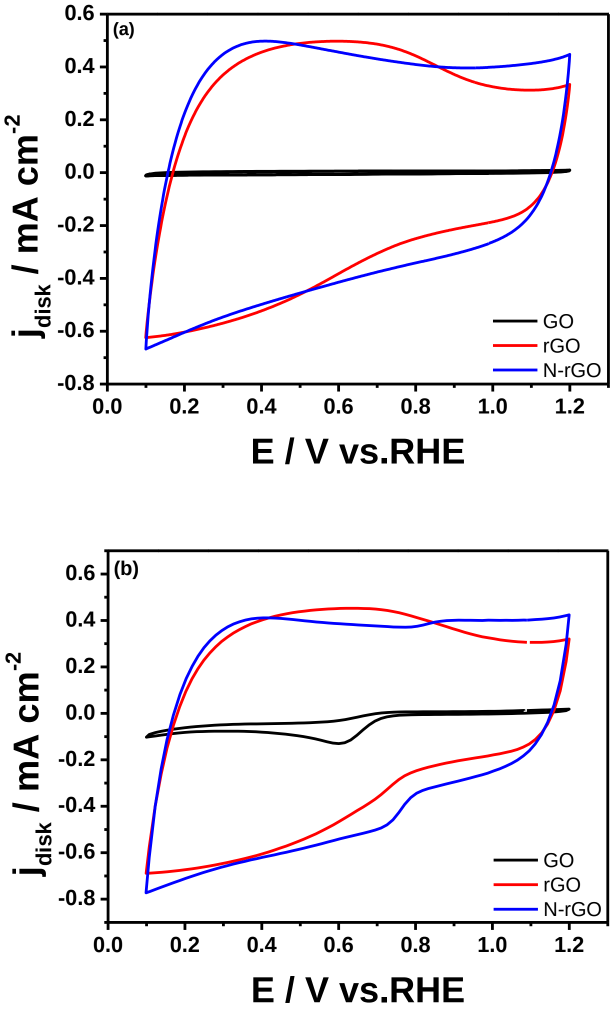

Figure 4.5 CV curves of GO, rGO, and N-rGO in 0.1 M KOH solution under (a) N_2-saturated and (b) O_2-saturated

After hydrothermal reduction of GO, cathodic reduction peak shifted positively to 0.71 V (vs. RHE) and 0.72 V (vs.RHE) of rGO and N-rGO respectively with increasing peak current density, indicating N doped to rGO can improve ORR activity [115]. The change in shape of the CV curves demonstrates the increase of the non-Faradaic currents induced by the increase in effective surface area of the electrically conductive graphene which is generated by the reduction of GO [112]. It can be seen that the excellent pseudo-capacitance of N-rGO was contributed by nitrogen doping on the interconnected structure of graphene [116-117].

4.1.5 Oxygen Reduction Reaction

The oxygen reduction reaction (ORR) polarization curves for these catalysts were investigated in O_2-saturated 0.1 M KOH solution using a rotating ring disk current (RRDE) at 1600 rpm shown in Figure 4.6. It is shown the RRDE plots for each samples, showing the measured disk current I_D at the bottom and the measured ring current I_R at the top. As observed from Figure 4.6 (a) shows a pronounced electrocatalytic ORR activity of N-rGO with more positive ORR onset potential (0.84 V vs. RHE) and higher cathodic current density at 0.1 V vs. RHE (3.82 mA cm^{-2}) than for rGO and N-rGO shown in Table 4.3. The more positive onset potential as well as the higher current density of N-rGO may be due to effect of the doped nitrogen species as well as the interconnected structure of rGO. The heteroatom doping can increase the electronic conductivity of the carbon materials due to pseudo-capacitance contribution in Figure 4.5 (b) in comparison with the non-doped ones [31-32]. Thus, oxygen could be easily absorbed onto the catalyst surface with preferred configuration in a large quantity, and the electrons could be transferred into the catalyst without difficulty [118]. It is also correlated to morphology in Figure 4.3(c), the interconnected of graphene sheets and overlapped structures are beneficial for oxygen diffusion which makes an easier contact between oxygen molecules and catalytic site [113, 119].

The electron transfer number (n) is one of the most important characteristics of the electrocatalytic oxygen reduction reaction (ORR) in aqueous electrolytes. This characteristic not only influences the efficiency of oxygen conversion but also provides information on the ORR mechanism. As can be seen in Table 4.3, the electron transfer number of N-rGO (3.88) is higher than rGO (3.51). Hence, we thought the higher electron transfer number of N-rGO almost depend on nitrogen doping effects. Doping the graphene with heteroatoms (nitrogen) introduces electrocatalytic active sites and increases the electrical conductivity as well as surface hydrophilicity [120]. The highest electron transfer number generated by GO because GO plays the role of a charge sink to allow rapid charge transfer in redox reaction [121], but a thick layered strutures which is shown in Figure 4.3 (a) will lead to a large ohmic resistance and significant mass transport limitations [82] and due to the degradation of surface functional group [114].

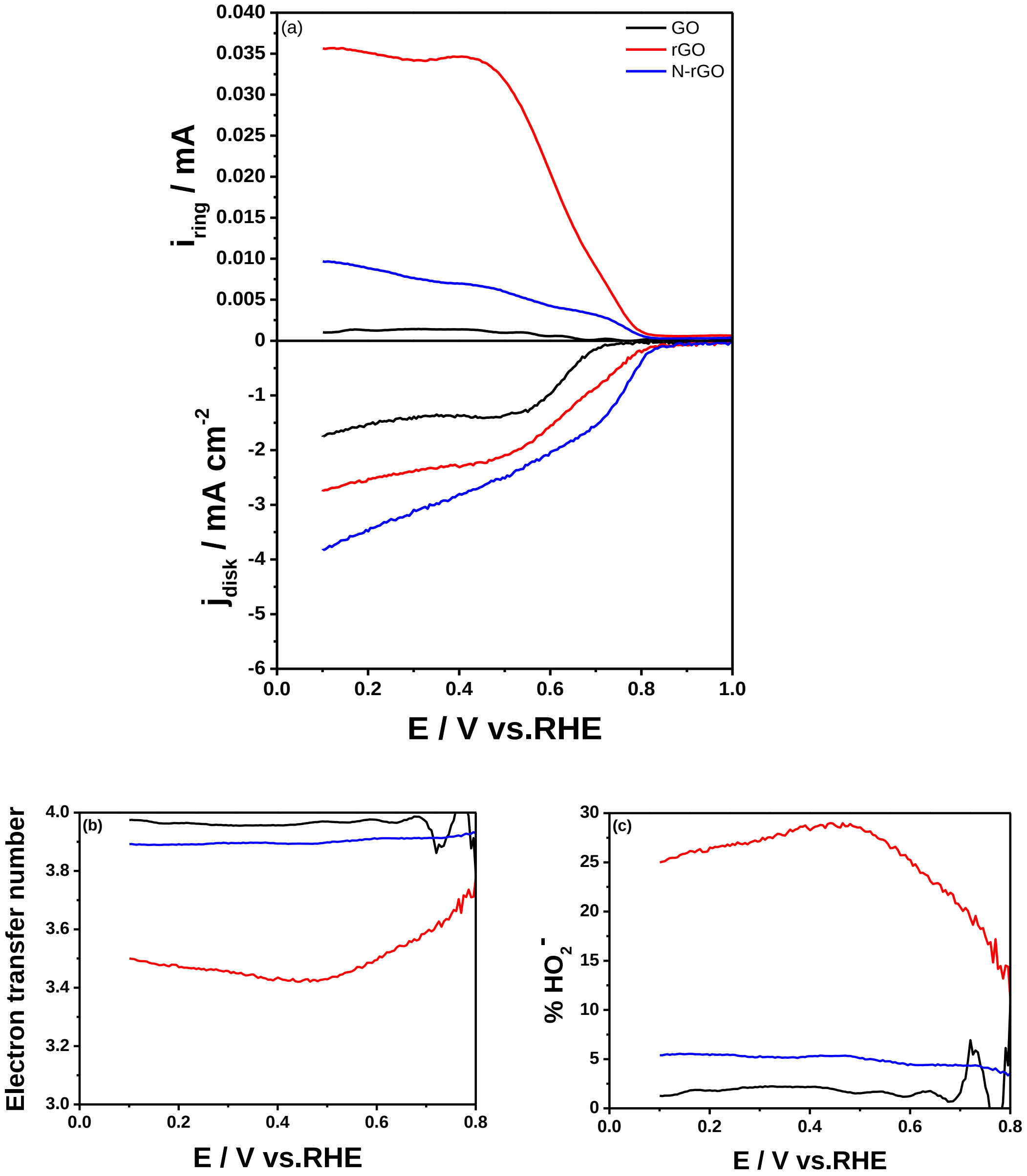

Figure 4.6 ORR performances of GO, rGO, and N-rGO in 0.1 M KOH solution under O_2-saturated (a) ring-disk current, (b) electron transfer number, and (c) %HO_2^-

Table 4.3 Electrochemical parameters of GO, rGO, and N-rGO

Catalyst	Onset potential (V vs. RHE)	Current density at 0.1 V vs. RHE (mA cm^{-2})	Electron transfer number *n*	% HO_2^-
GO	0.72	1.74	3.94	1.74
rGO	0.82	2.73	3.51	24.34
N-rGO	0.84	3.82	3.88	6.07

4.2 The Effect of Transition Metals on Ternary Palladium-based Catalyst

The ternary Pd-M (M = Fe, Ni, and Co) nanoparticles have been extensively studied as electrocatalysts for the oxygen reduction reaction (ORR) in alkaline media. Catalytic activity can be influenced by the additional metals on ternary Pd-based catalyst [122].

4.2.1 X-Ray Diffraction Results

The X-ray diffraction (XRD) pattern of Pd/N-rGO and ternary Pd-based/ N-rGO electrocatalysts can be shown in Figure 4.7. The diffraction peak of Pd/N-rGO located at about 2ϴ = 25.39° corresponds to the characteristic of N-rGO and also can be observed at 40.1°, 46.7°, and 67.8° are characteristics of crystalline face centered cubic (fcc) Pd nanoparticles (PDF 46-1043), corresponding to the (111), (200), (220) planes, respectively. For the diffraction peak located at 2ϴ = 40.33°, 40.53° and 40.26° of PdFeNi/N-rGO, PdCoNi/N-rGO, and PdFeCo/N-rGO respectively, which is close to the (111) plane of Pd nanoparticles. For all XRD patterns of ternary Pd-M/N-rGO do not show any peaks of Ni (PDF 04-0850), Co (PDF 15-0806), or Fe (PDF 06-0696), investigating because of the addition particles may be of significantly small size and be present in a small amout [123-124]. They also show a slight shift to higher 2ϴ values due to Ni, Co, and Fe are alloyed with Pd [125-126]. He et al. [127] also introduces the incorporation of Fe, Co, and Ni atoms into the Pd fcc structure would result in the formation of ordered intermetallic phases with a concomitant lattice contraction, so influences the shifted of diffraction peaks to higher angle. The transition metals in the XRD patterns indicate a gradually changing average nanoparticle crystal structure and since no sharp peaks were observed [128] in Figure 4.7. According to the Debye-Scherrer formula (equation 3.2), the smaller the particle size is, the larger the half-peak width is, and the weaker the corresponding peak intesity is [129].

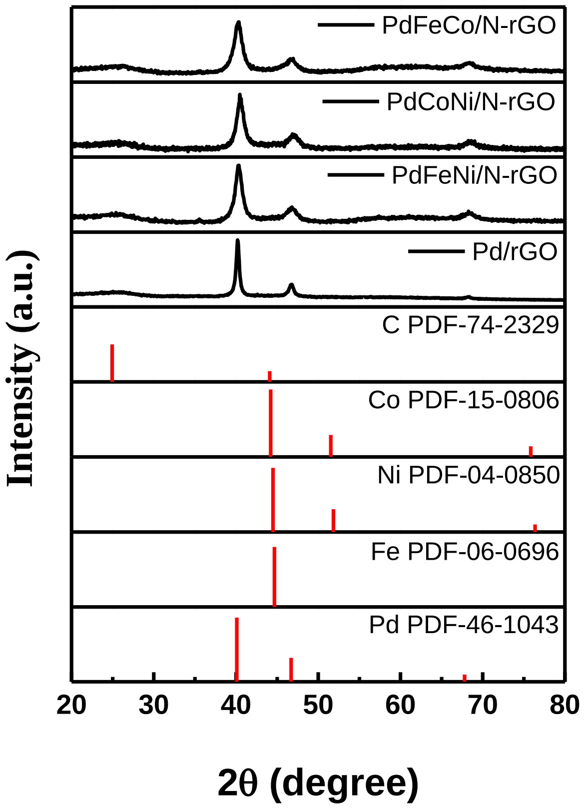

Figure 4.7 XRD patterns of Pd/N-rGO and ternary Pd-based/N-rGO

Table 4.4 XRD result of Pd/N-rGO and ternary Pd-based/N-rGO

Sample	Peak position 2Θ at (111)	Crystallite size (nm)
Pd/N-rGO	40.10	16.29
PdFeNi/N-rGO	40.33	8.02
PdCoNi/N-rGO	40.53	7.61
PdFeCo/N-rGO	40.26	7.08

4.2.2 Raman Spectra

Raman spectroscopy was used to further examine the ordered and disordered crystal structure of graphene sheets. The two remarkable peaks around 1346.78 and 1596.45 cm^{-1} (Figure 4.8) referred to the D-band and G-band of the graphene sheet [103]. The D band becomes prominent when defects are introduced in graphene [130]. It can be shown in Table 4.5, all spectra the I_D/I_G ratio of ternary Pd-based/N-rGO were increased compared to Pd/N-rGO, it suggested the clear change in carbon system due to the incorporation of some extra defects (transition metals) in graphene [131]. The I_D/I_G ratio of all catalysts has shown a relative same value which is indicated that microwave hydrothermal method is not given influenced the each bonding of catalysts.

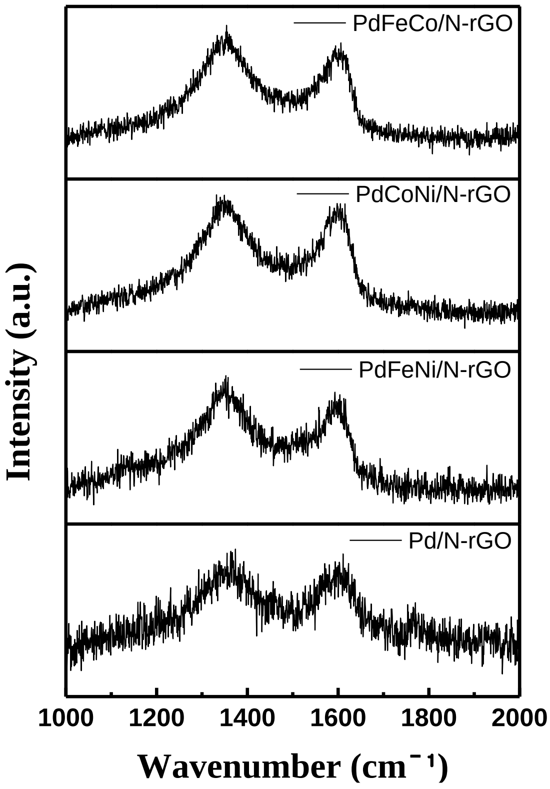

Figure 4.8 Raman spectra of Pd/N-rGO and ternary Pd-based/N-rGO

Table 4.5 Raman spectra result of Pd/N-rGO and ternary Pd-based/N-rGO

Catalyst	G-band (cm^{-1})	D-band (cm^{-1})	I_D	I_G	I_D/I_G
Pd/N-rGO	1346.78	1596.45	22.27	21.39	1.04
PdFeNi/N-rGO			62.13	53.68	1.16
PdCoNi/N-rGO			64.52	56.71	1.14
PdFeCo/N-rGO			65.92	56.44	1.17

4.2.3 Field Emission Scanning Elctron Microscopy with Energy Dispersive X-Ray Spectroscopy

The field emission scanning electron misroscopy (FE-SEM) images of of ternary Pd-M by reduction method has been investigated in Figure 4.9.

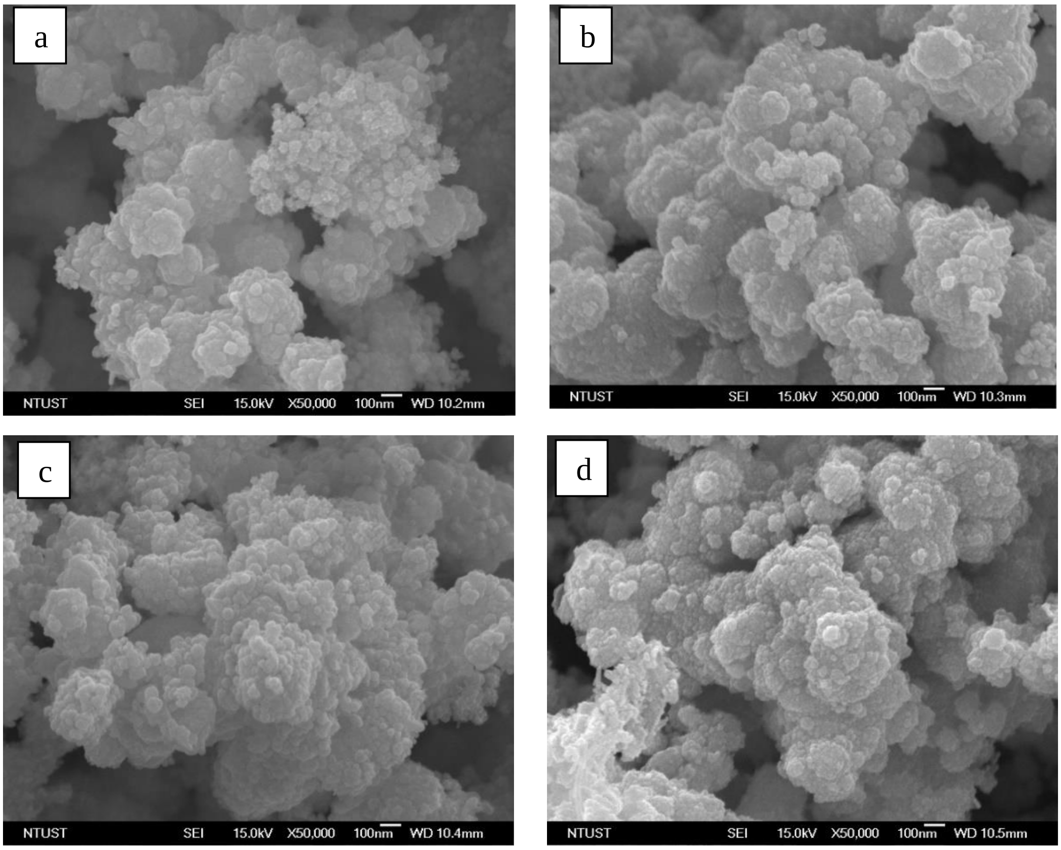

Figure 4.9 FE-SEM image of (a) Pd, (b) PdFeNi, (c) PdCoNi, and (d) PdFeCo

As can be seen in Figure 4.9, all particles of ternary Pd-M are observed with large agglomerates. These large agglomerates might be ascribed to the fast reduction process [36]. The physical phenomenon of rotary evaporator is used to make ternary Pd-M supported on N-rGO in N-hexane solution. N-hexane solution can distributed uniformly of metal nanoparticles, as well as porous materials used as supports with a high surface area [132-133]. As can be seen in Figure 4.10, all metal particles distributed on the N-rGO are uniformly. There is also no obvious large agglomeration of particles on the surface N-rGO, this phenomenon also occured because the nitrogen doping provides more defect locations for the nanoparticles and promotes a higher dispersion of metal nanoparticles [124, 134].

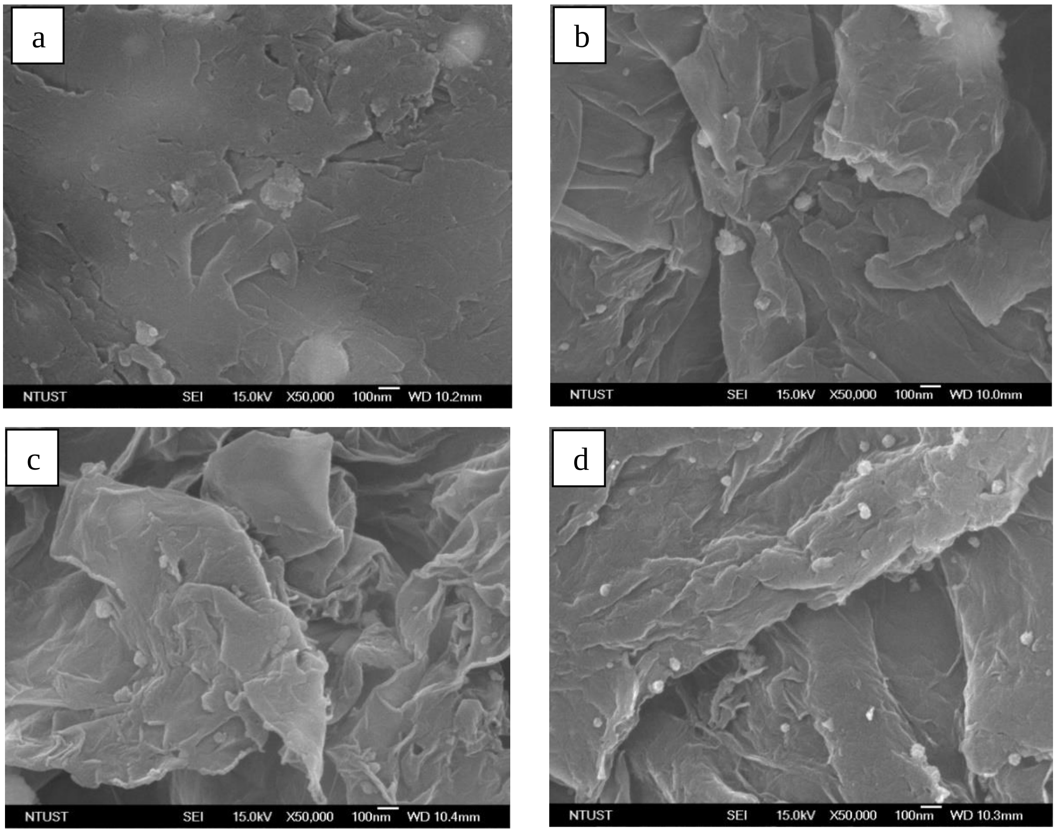

Figure 4.10 FE-SEM image of (a) Pd/N-rGO, (b) PdFeNi/N-rGO, (c) PdCoNi/N-rGO, and (d) PdFeCo/N-rGO

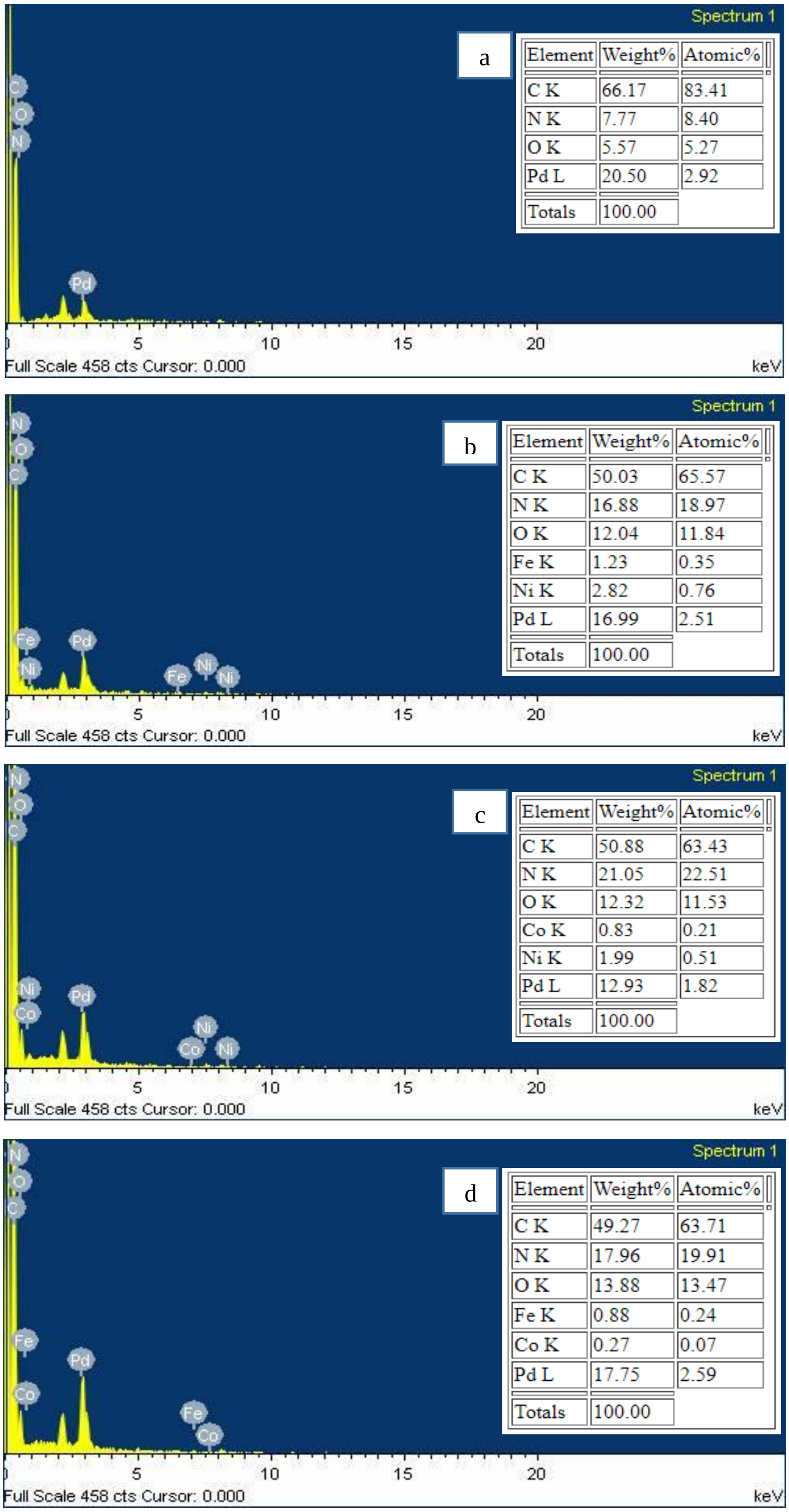

Element	Weight%	Atomic%
C K	66.17	83.41
N K	7.77	8.40
O K	5.57	5.27
Pd L	20.50	2.92
Totals	100.00	

Element	Weight%	Atomic%
C K	50.03	65.57
N K	16.88	18.97
O K	12.04	11.84
Fe K	1.23	0.35
Ni K	2.82	0.76
Pd L	16.99	2.51
Totals	100.00	

Element	Weight%	Atomic%
C K	50.88	63.43
N K	21.05	22.51
O K	12.32	11.53
Co K	0.83	0.21
Ni K	1.99	0.51
Pd L	12.93	1.82
Totals	100.00	

Element	Weight%	Atomic%
C K	49.27	63.71
N K	17.96	19.91
O K	13.88	13.47
Fe K	0.88	0.24
Co K	0.27	0.07
Pd L	17.75	2.59
Totals	100.00	

Figure 4.11 EDX patterns of (a) Pd/N-rGO, (b) PdFeNi/N-rGO, (c) PdCoNi/N-rGO, and (d) PdFeCo/N-rGO

Dark and bright spots indicate existing electron from different elements. Dark spots corresponds the beam travels into hole in the sample and the amount of secondary electrons in the surface is reduced. Bright spots are caused by incident beam scans across hill on samples and they have more electrons on the sample surface. Those observations also contribute the element that exist in prepared powder catalyst. For energy dispersive X-ray spectroscopy (EDX) analysis in Figure 4.11, the nanocatalysts contain C, N, O, and ternary Pd-M nanoparticles of each others. The presence of O peak, which is due to residual oxygen containing functional groups on N-rGO [36], while the presence of Pd, Fe, Co, and Ni proved that ternary Pd-M nanoparticles were successfully loaded on the N-rGO surface.

4.2.4 Cyclic Voltammogram

To investigate the electrocatalytic ORR performance of catalysts, cyclic voltammmetry (CV) was performed in 0.1 M KOH solution in Figure 4.12 (a) and Figure 4.12 (b) for N_2 and O_2 saturated respectively. The CV of commercial Pt/C in N_2 saturated exhibit the typical hydrogen underpotential adsorption and desorption peaks in the region 0.1 - 0.45 V vs. RHE, while oxide formation for oxidation and reduction peak of Pt were seen at 0.85 and 0.71 V vs. RHE respectively, which is consistent with findings reported in the literature [48]. Oxide formation on Pt in alkaline media are due to spesific adsorption OH^- and either desorption of oxygen containing species or reduction of the platinum itself from the supporting electrolyte during oxidation and reduction respectively [56, 135-136]. For N_2 saturated KOH solution in Figure 4.12 (a) show oxide formation of Pd reduction peaks at 0.66, 0.67, 0.67, and 0.69 vs. RHE of Pd/N-rGO, PdFeNi/N-rGO, PdCoNi/N-rGO, and PdFeCo/N-rGO respectively. These values are slightly negatively shifted compared with commercial Pt/C. As can be seen in Figure 4.12 (a) in case of Pd/N-rGO and ternary Pd-M/N-rGO, the CV give low intense hydrogen adsorption and desorption peaks in the low potential region, which is same reported with the previous reported [137].

For O_2 saturated KOH solution in Figure 4.12 (b), the ORR onset potential (E_{onset}) of Pd/N-rGO was located at 0.86 V vs. RHE with the cathodic reduction peak at 0.74 RHE. After incorporation of Fe, Co, and Ni atoms in the Pd nanoparticles, both E_{onset} and the ORR reduction peak potential were positively shifted to (0.87 and 0.76) V vs. RHE of PdFeNi/N-rGO, (0.89 and 0.77) V vs. RHE of PdCoNi/N-rGO, and (0.93 and 0.79) V vs. RHE of PdFeCo/N-rGO, accompanied by a concomitant increase in the peak current density. It can be indicated the incorporation transition metals on surface graphene sheets can improve ORR activity [115, 138].

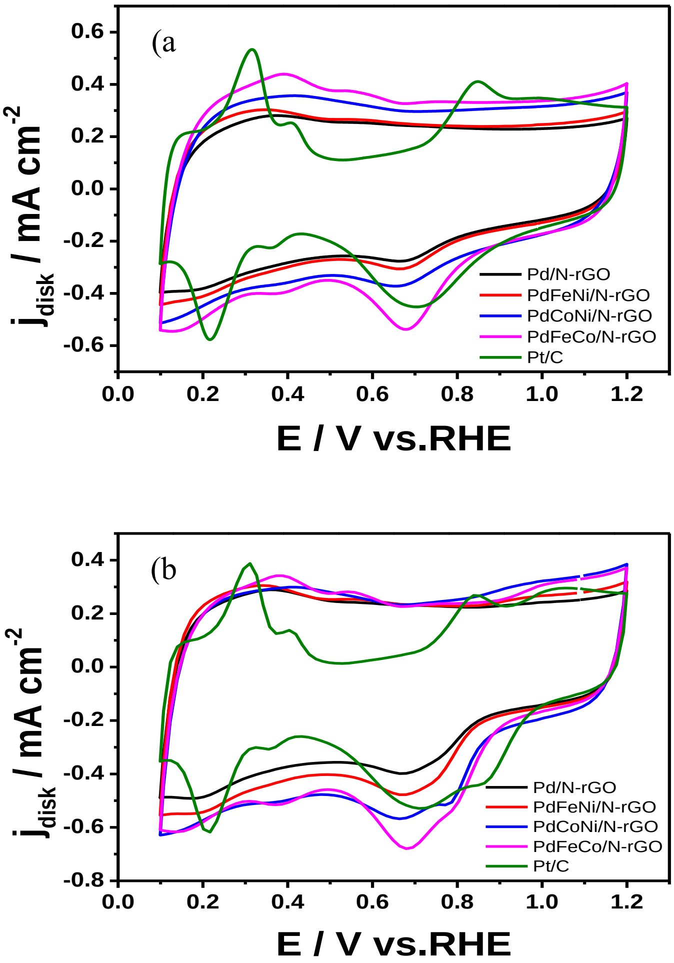

Figure 4.12 CV curves of Pd/N-rGO, ternary Pd-M (M = Fe, Ni, and Co)/N-rGO, and Pt/C in 0.1 M KOH solution under (a) N_2-saturated and (b) O_2-saturated

4.2.5 Oxygen Reduction Reaction

The oxygen reduction reaction (ORR) polarization curves for these catalysts were investigated in O_2-saturated 0.1 M KOH solution using a rotating ring disk current (RRDE) at 1600 rpm shown in Figure 4.13. It is shown the RRDE plots for each samples, showing the measured disk current I_D at the bottom and the measured ring current I_R at the top.

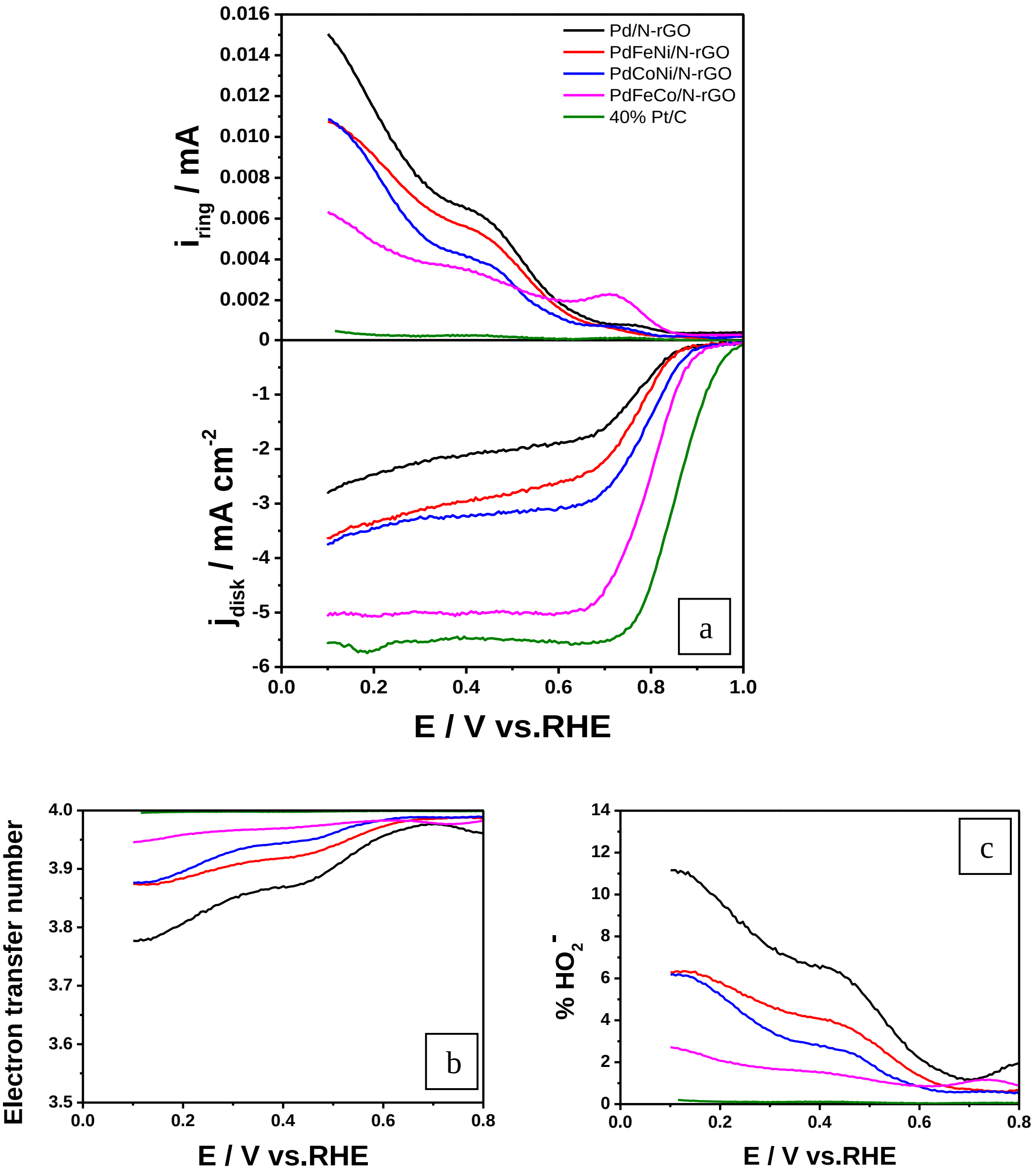

Figure 4.13 ORR performances of Pd/N-rGO, ternary Pd-M (M = Fe, Ni, and Co)/N-rGO, and Pt/C in 0.1 M KOH solution under O_2-saturated (a) ring-disk current, (b) electron transfer number, and (c) %HO_2^-

As can be observed at Figure 4.13 (b), the onset potential and the current density for ternary Pd-M are calculated 0.87, 0.89, and 0.93 V vs. RHE of

PdFeNi/N-rGO, PdCoNi/N-rGO, and PdFeCo/N-rGO respectively. The more positive onset potential as well as the higher current density of all ternary Pd-M/N-rGO from the Pd/N-rGO (Table 4.6) indicates that the transition metals enhanced the activity of ORR. The incorporation of Fe, Co, and Ni atoms in the Pd nanoparticles would adjust the compressive strain of the Pd surface, resulting in a change in the Gibbs free energy of the intermediate state and providing an effective approach to improve the catalytic activities of the Pd [139-140]. The highest onset potential of PdFeCo/N-rGO and closed to Pt/C of 0.99 V vs. RHE are caused by the strong incorporation of Fe and Co atoms in the Pd nanoparticles. The effect of Co presence is the decrease in metal particle size, thus increasing ORR activity [18, 55], it is also correlated with the particle size which is calculated by Debye-Scherrer formula (Table 4.4). Iron can greatly increase catalyst activity due to the strong bonding of Fe with nitrogen doped carbon based (Fe-NCX), so it can be conclude that the bonding iron with nitrogen doped rGO is also important plays to enhance the ORR activity [56, 141]. The highest ORR performance of PdFeCo/N-rGO with increase diffusion limited current density due to the uniform distribution of active sites on the catalyst surface [136], which is coressponding to HAADF-STEM-EDS in Figure 4.15. The ORR acticity can be summarized at Table 4.6.

On the other hand, the high yield of the peroxide (HO_2^-) in the ORR mechanism may damage the catalyst or the membrane in the membrane electrode assembly (MEA) [142]. The transferred electron number (*n*) and the HO_2^- yield of the catalysts are shown in Figure 4.13 (c) and 4.13 (d) respectively. The Pt/C through a four-electron process over 0.99 V vs. RHE, and the HO_2^- yield is negligible. While the transferred electron number (*n*) of catalysts at potentials of 0.1 to 0.8 V vs. RHE is evaluated to be average 3.87, 3.93, 3.94, and 3.96 of Pd/N-rGO, PdFeNi/N-rGO, PdCoNi/N-rGO, and PdFeCo/N-rGO respectively, which suggests a direct reduction of O_2 to H_2O via $4e^-$ pathway [36]. In either case, a low value for the transferred electron number indicates that the catalyst may generate a significant amount of the HO_2^- yield as intermediate product [143]. Therefore, the reaction used $4e^-$ pathway to produce less H_2O. It is correlated with the catalysts generated which is shown in Table 4.6, a decreasing value of the electron transfer number (*n*) would increased amount of the HO_2^- yield. It is confirmed that PdFeCo/N-rGO has the highest transferred electron number (*n*) and least of the HO_2^- yield compare with the other ternary Pd-based/N-rGO catalysts, indicating it is most likely reducing oxygen via the highly desirable and efficient direct 4e$^-$ process where O_2 is completely reduced to OH^-, without producing significant amounts of intermediates [53].

Table 4.6 Electrochemical parameters of Pd/N-rGO, ternary Pd-M/N-rGO, and Pt/C

Catalyst	Onset potential (V vs. RHE)	Current density at 0.1 V vs. RHE (mA cm^{-2})	Electron transfer number *n*	% HO_2^-
Pd/N-rGO	0.86	2.78	3.87	6.23
PdFeNi/N-rGO	0.87	3.63	3.93	3.43
PdCoNi/N-rGO	0.89	3.73	3.94	2.83
PdFeCo/N-rGO	0.93	5.05	3.96	2.00
40% Pt/C	0.99	5.55	4.00	~0.00

4.2.6 Field Emission Trasnmission Electron Microscopy

The field emission transmission electron microscopy (FE-TEM) test were carried out in order to observe the shape, structure, and dispersion of the synthesized PdFeCo nanoparticles as the best sample over the support, which is shown in Figure 4.14. In Figure 4.14 (a) can be observed, the small nanoparticles are distributed uniform on the surface of N-rGO with the particle size is around 10-20 nm. The crystallite size measured by TEM is higher than the crystallite size from XRD analysis is due to overlapped of the particles. The TEM images indicate that the nanoparticles had a mixture of irregular and square shape in Figure 4.14 (b). The differences in shape indicate that doping of various transition metals in Pd would affected strongly in its morphology [144]. The second reasons is due to rGO plays a different role during formation, perhaps modifying the nucleation and reduction which are influence for the undirectional growth, which is determined by the presence or absence of carbon functional groups on the surface which may act as anchoring centers as nucleation sites [34]. The high-resolution TEM (HRTEM) images are shown in Figure 4.14 (c). The lattice fringes distance are found to be 0.226 nm and 0.228 nm which are close to the (111) lattice of the face-centered cubic (fcc) planes of Pd metal (0.224 nm) according to the PDF 46-1043. This result demonstrates the preferential growth along the (111) directions of the PdFeCo nanoparticles. The anisotropic growth along the (111) direction is due to the low surface energy of the (111) crystal plane [129, 145].

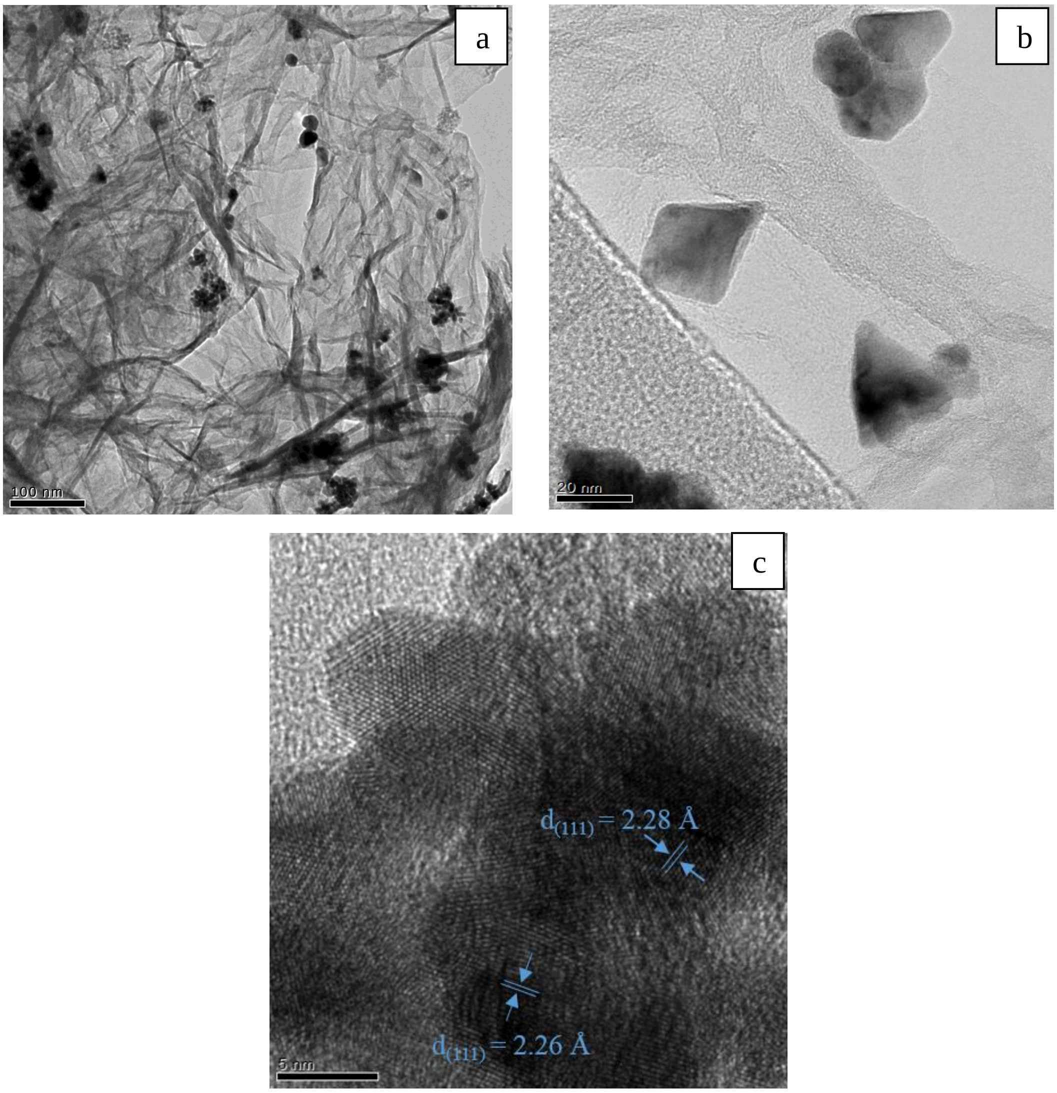

Figure 4.14 (a and b) TEM and (c) HRTEM images of PdFeCo/N-rGO

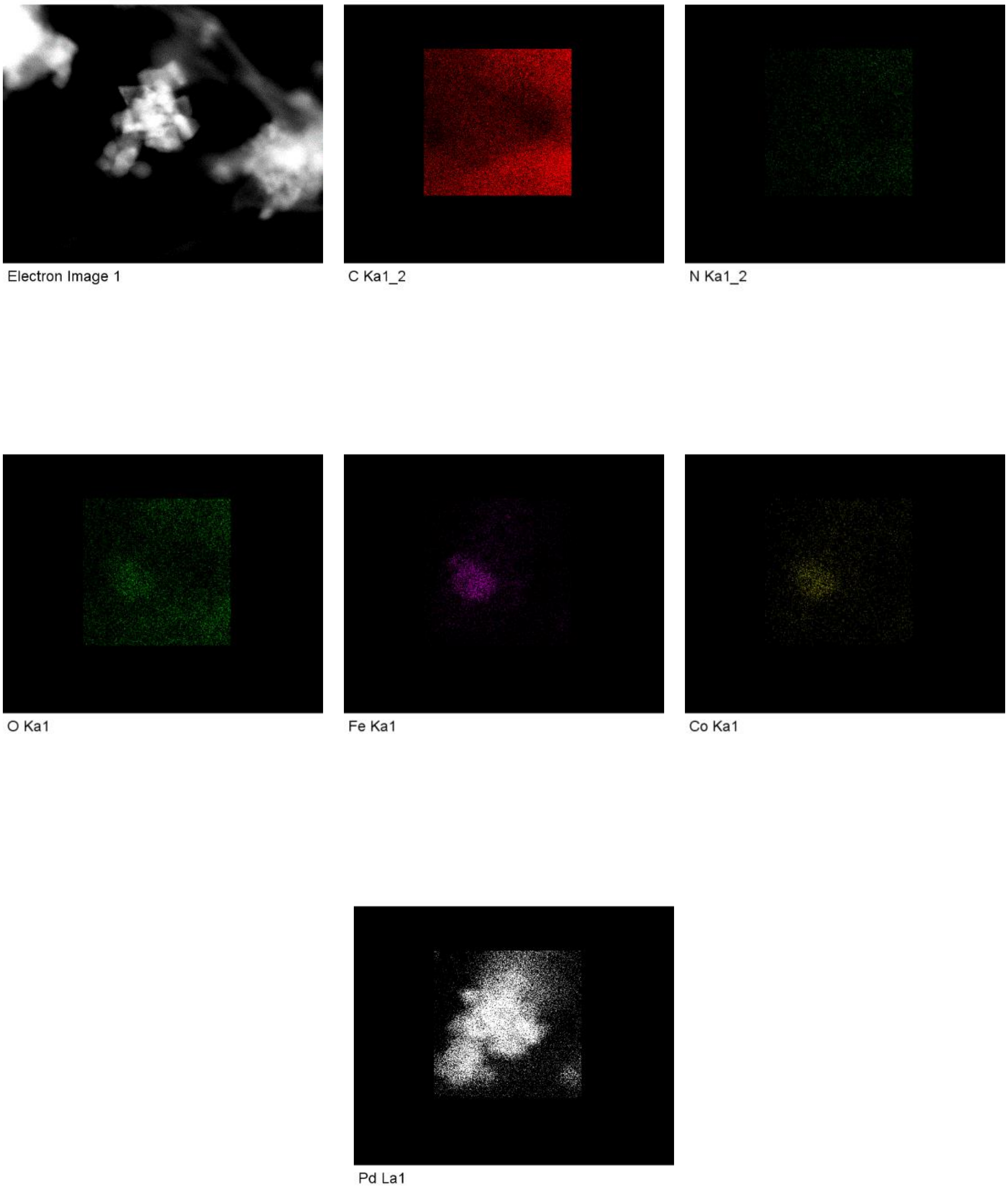

Electron Image 1

C Ka1_2

N Ka1_2

O Ka1

Fe Ka1

Co Ka1

Pd La1

Figure 4.15 HRTEM images of PdFeCo/N-rGO

High-angle annular dark-field scanning transmission electron microscopy – energy dispersive X-ray spectroscopy (HAADF-STEM-EDS) is employed to study the elemental composition and distribution of catalyst. Figure 4.15 shows the HAADF-STEM-EDS mapping of each elements of PdFeCo/N-rGO nanocatalyst. These images show that Pd, Fe, Co, N, C, and O are uniformly distributed in the whole PdFeCo/N-rGO nanocatalyst. The result indicates that the three elements (Pd, Fe, and Co) mixed very well on the N-rGO surface, which confirms that the PdFeCo/N-rGO has been successfully synthesized. The presence of O, which is due to residual oxygen containing functional groups on N-rGO [36].

4.2.7 X-ray Photoelectron Microscopy

The X-ray photoelectron microscopy (XPS) test were carried out in order to further investigate the reduction level and determine the composition of the synthesized PdFeCo nanoparticles as the best sample over the support. The elemental percentages of each elements are shown in Table 4.7. The precentage atomic ratio of transition metals alloyed to Pd (3.57: 1.18: 0.90) are closed to experimental design (3:1:1). As shown in Figure 4.16, the XPS exhibits the presence of Pd, Fe, Co, C, and N elements on the PdFeCo/N-rGO catalyst. In Figure 4.16 (a), the XPS spectrum of Pd shows characteristic peaks at 335.2 and 341.2 eV corresponding to the Pd $3d_{5/2}$ and Pd $3d_{3/2}$ respectively. Compared to the standard spectra of metal Pd^0, the binding energies of Pd increase greatly (from 335 eV to 335.2 eV and from 340 eV to 341.2 eV), these result is due to the presence a transition metal support interaction occurs between Pd nanoparticles and N-rGO support [146]. While the components at binding energy of 336.4 eV and 342.5 eV are attributed to Pd^{2+}. The existence of Pd^{2+} may be attributed to the following reasons: (a) the Pd-N bond formed at the interface of Pd/N-rGO, (b) the reduction of Pd^{2+} was not completed from precursor; (c) the external metal Pd^0 is likely oxidized to Pd^{2+} at ambient conditions [147-149].

There are two main peaks observable at the high resolution XPS spectrum for Fe 2p region at 711.7 eV and 723.9 eV corresponding to the Fe $2p_{3/2}$ and $2p_{1/2}$ respectively in Figure 4.16 (b). These peaks increase slightly (from 707 eV to 711.7 eV and from 720 eV to 723.9 eV) compared to the standard spectra of metal Fe^0, indicating oxidised Fe species. This phenomenon occured due to the catalyst is exposed to air for a certain time during the sample preparation and it is well known that Fe is highly sensitive to air, being easily oxidised [150]. The predominant $2p_{3/2}$ and $2p_{1/2}$ peaks of Co^0 are observed at 778.57 eV and 793.06 eV respectively in Figure 4.16 (c).

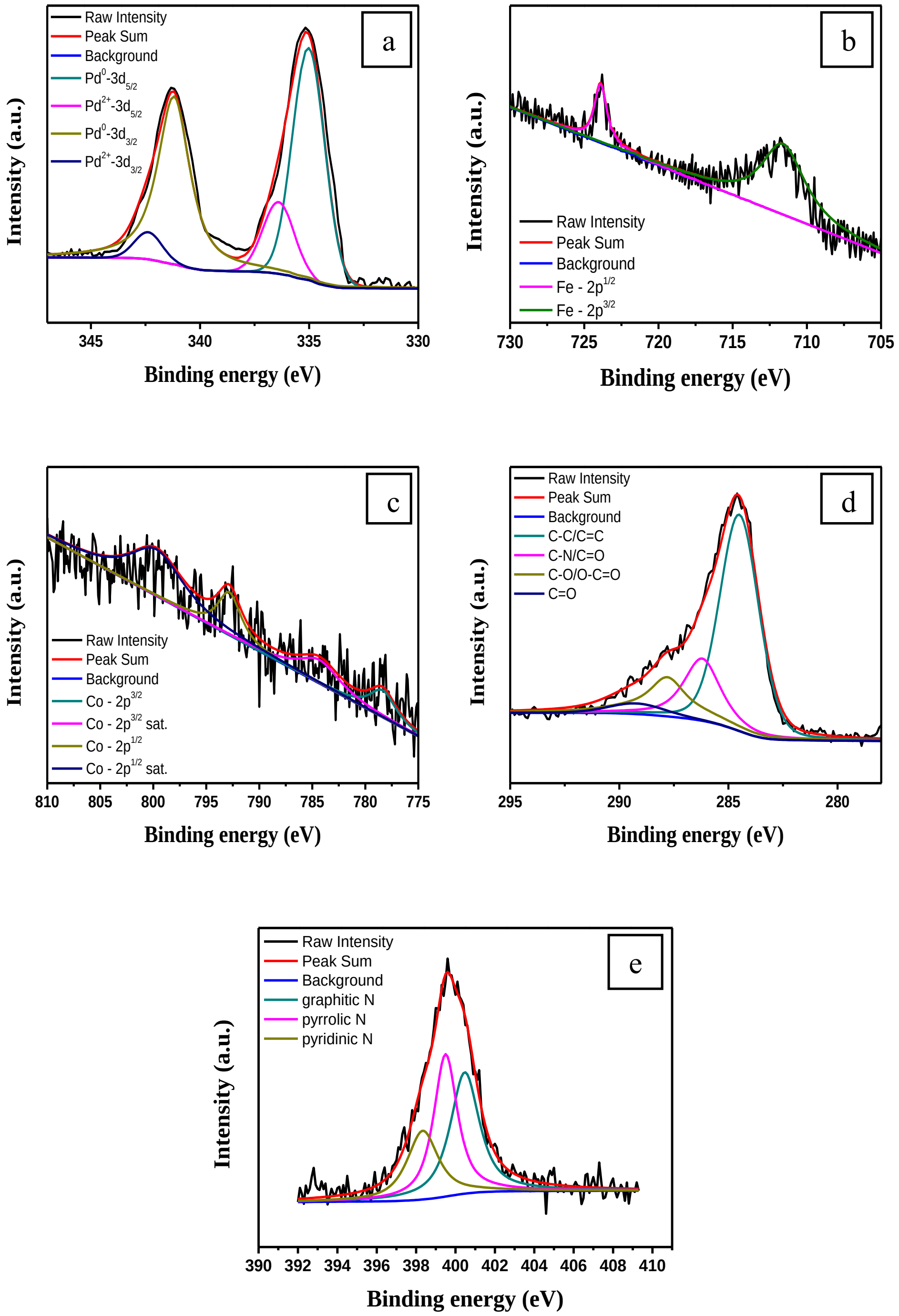

Figure 4.16 The XPS spectra of PdFeCo/N-rGO (a) Pd-3d spectra, (b) Fe-2p spectra, (c) Co-2p spectra, (d) C-1s spectra, and (e) N-1s spectra

These peaks also increase slightly (from 778 eV to 778.57 eV and from 793 eV to 793.06 eV) compared to the standard spectra of metal Co^0 and in addition the shake-up satellite (sat.) peaks at the high binding energy side of the Co $2p_{3/2}$ and Co $2p_{1/2}$ at 784.7 eV and 800.28 eV, indicating the presence of Co^{2+} which may be caused by the surface oxidation or chemisorption of environmental oxygen during the synthesis process [151-152].

Table 4.7 The elemental percentages of PdFeCo/N-rGO

Catalyst	Pd (at %)	Fe (at.%)	Co (at.%)	C (at.%)	N (at.%)
PdFeCo/N-rGO	6.07	2.01	1.53	73.16	17.23

The presence of C and N also show in Figure 4.16 (d) and 4.16 (e) respectively. As can be seen in Figure 4.16 (d), the formation of C-C/C=C, C-N/C=O, C-O/O-C=O, and C=O are located at 284.6 eV, 286.3 eV, 287.97 eV, and 289.3 eV respectively, indicating by the C 1s XPS spectra [153]. The N 1s spectrum in Figure 4.16 (e) suggests the presence of three types of N, including pyridinic-N (398.32 eV), pyrrolic-N (399.48 eV), and graphitic-N (400.48 eV) [91]. The main type of plannar pyridinic-N and pyrrolic-N may possess a low electrical resistance and high electrocatalytic activity of the N-rGO since the nitrogens with planar sp^2 hybridization would not interrupt the π-π conjugation and avoid an intrinsic barrier impairing a continuous pathway for electron transport, thus may be activated where O_2 molecules could be adsorbed and reduced during the ORR [87, 154-158]. Meanwhile several research groups have reported that the pyridinic-N was the active site to enhance the ORR activity of the N-doped carbon materials, some others suggested that more graphitic-N atoms, rather than the pyridinic ones, are important for the ORR [159-160].

Table 4.8 The percentages of N-types in PdFeCo/N-rGO

Catalyst	Pyridinic-N (%)	Pyrrolic-N (%)	Graphitic-N (%)
PdFeCo/N-rGO	23.78	37.39	38.83

4.2.8 Methanol Oxidation

Methanol produces CO_2 on electro-oxidation and carbonate formation, which is shown in equation 2.7 can be even more of a problem when a methaol fuel cell is operated with a liquid alkaline electrolyte. The methanol ozidation of PdFeCo/N-rGO and commercial 40% Pt/C is shown in Figure 4.17. For Pt/C exhibited a marked change in its ORR polarization curve after the addition of 0.1 M MeOH, the half-wave potential shift negatively, indicating the methanol and oxygen simultaneously react at the surface of the particles [93]. Despite PdFeCo/N-rGO shows the peak oxidation affected by the presence of methanol but its peak shows a narrow shape and leads to a lower current density value than previous reported [94]. The affected of peak oxidation indicates that the supporting electrolyte can influence the reaction products during the ORR process in presence of methanol [56, 94]. It can be suggested that the PdFeCo/N-rGO is more effective for cathode catalyst in alkaline media in presence of methanol than previous reported [94].

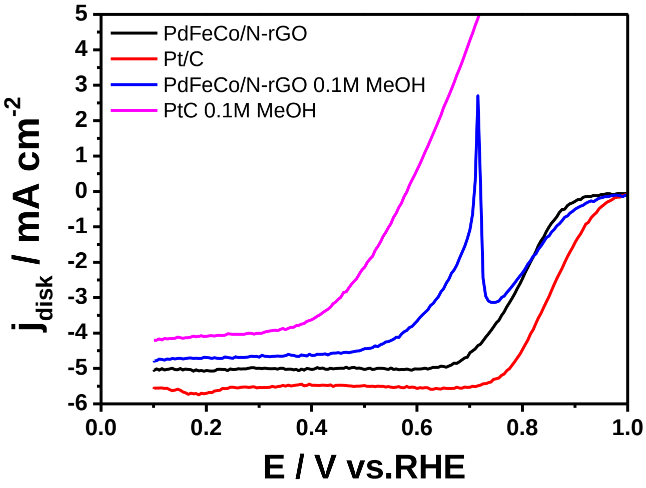

Figure 4.17 Methanol oxidation of PdFeCo/N-rGO and Pt/C in 0.1 M KOH + 0.1 M MeOH solution under O_2-saturated

4.2.9 Stability Test

For practical fuel cells, the long-term stability of the electrode is of great importance. The stability of PdFeCo/N-rGO catalyst has also been evaluated compared to commercial 40% Pt/C in Figure 4.18. The both catalyst were employed for ORR after scanning LSV curves in an O_2-saturated 0.1 M KOH solution. As can be seen in Figure 4.18 (b), Pt/C loses significant activity about 14.76% from initial value after 30000 cycles for both in kinetic and diffusion limiting regions (Table 4.9). This phenomenon would result from Pt dissolution, redeposition on the catalyst surface and Pt migration through the surface [161]. The dissolved Pt^{2+} ions can be redeposited on the Pt surface, resulting in the formation of larger less dispersed Pt nanoparticles, this phenomenon known as Ostwald ripening [162].

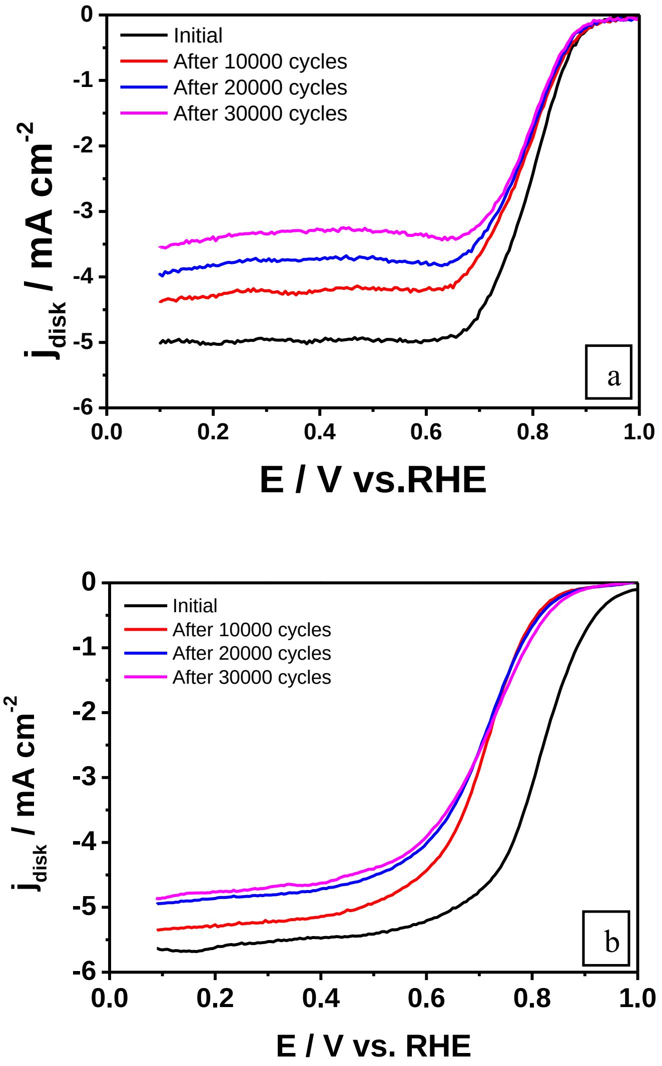

Figure 4.18 The stability performance of (a) PdFeCo/N-rGO and (b) Pt/C in 0.1 M KOH solution under O_2-saturated

Table 4.9 Stability parameters of PdFeCo/N-rGO and Pt/C

Catalysts	PdFeCo/N-rGO	Pt/C
Initial half-wave (mV)	799	813
10000 cycles (mV)	773	707
20000 cycles (mV)	765	695
30000 cycles (mV)	757	693
$\Delta E_{1/2}$ (mV)	42	120

In contrast with PdFeCo/N-rGO, it loses significant activity about 5.25% from initial value after 30000 cycles in diffusion-limiting regions, but slow degradation in kinetic region, which is due to the existence of π bonds and well dispersed PdFeCo nanoparticles on graphene sheets which actually the synergetic promotional effect between the nanoparticles and the support [163].

CHAPTER V

CONCLUSIONS

The nitrogen doped reduced graphene oxide (N-rGO) has successfully snynthesized by microwave hydrothermal method. The X-ray diffraction (XRD) patterns confirmed the presence of N-rGO caused the increase slightly peak at higher angle indicating the slightly structure changes were occurred after deoxidation and nitrogen doping. After nitrogen doping, it caused the formation of more defective sites with increasing I_D/I_G which confirmed from raman spectra. The interconnected of graphene sheets with overlapped structures of N-rGO can serve as a buffering reservoir where the reactant can reduce the diffusional path to the interior and the excellent pseudo-capacitance of N-rGO which was confirmed by CV curve, leading to higher ORR performance. The oxygen reduction reaction (ORR) of N-rGO show the highest onset potential and current density lead the highest electron transfer number and least yield of % HO_2^- compared other carbon based catalysts.

The high performance of N-rGO lead to make a composite with ternary Pd-M (M = Fe, Ni, and Co) as supported carbon based material. The Pd-M catalysts has successfully synthesized by emulsion method. The ternary Pd-M supported on N-rGO already successfully synthesized by rota-evaporation method with the presence N-hexane solution. The ORR performance show the PdFeCo/N-rGO is the best catalyst compared with others (PdFeCo/N-rGO > PdCoNi/N-rGO > PdFeNi/N-rGO) with the highest onset potential and current density. The highest electron transfer number of PdFeCo/N-rGO which is close to dominant four electron pathway generates least yield of % HO_2^-. This is confirmed from XRD pattern which resulted the smallest crystallite size which is calculated by Debye-Scherrer formula. The highest I_D/I_G of PdFeCo/N-rGO caused extra defects on carbon and lead to higher ORR performance. There is also no obvious large agglomeration and homogeneous distribution of particles on the surface N-rGO which confirmed from field emission scanning electron microscopy (FE-SEM) and representative field emission transmission electron microscopy (FE-TEM) images. X-ray photoelectron spectroscopy (XPS) results confirmed the presence of Pd, Fe, Co, N, and C in PdFeCo/N-rGO which are agreed with the experimental design of ratio. The presence highest precentage of graphitic-N can increase active site leading to enhance the ORR activity.

For practical fuel cells, the tolerance from methanol oxidation and the long-term stability of the electrode are of great importance. The affected limiting current density of PdFeCo/N-rGO only fluctuation slightly mainly due to the presence of methanol in alkaline solution. For stability test, it is confirmed that the PdFeCo/N-rGO has an excellent stability compared to the commercial Pt/C after LSV test of 30000 cycles, which decrease slightly initial value in the kinetic region.

REFERENCE

[1] Y. Yang, J. Wang, J. Zheng, S. Li, S. Zhang, A stable anion exchange membrane based on imidazolium salt for alkaline fuel cell. Journal of Membrane Science, 467 (2014) 48-55.

[2] G. Merle, M. Wessling, K. Nijmeijer, Anion exchange membranes for alkaline fuel cells: A review. Journal of Membrane Science, 377 (2011) 1-35.

[3] A. Zadick, L. Dubau, N. Sergent, G. Berthome, M. Chatenet, Huge instability of Pt/C catalysts in alkaline medium. ACS Catalysis, 5 (2015) 4819-4824.

[4] H.R. Colón-Mercado, B.N. Popov, Stability of platinum based alloy cathode catalysts in PEM fuel cells. Journal of Power Sources, 155 (2006) 253-263.

[5] A. Serov, C. Kwak, Review of non-platinum anode catalysts for DMFC and PEMFC application. Applied Catalysis B: Environmental, 90 (2009) 313-320.

[6] H. Erikson, M. Liik, A. Sarapuu, J. Kozlova, V. Sammelselg, K. Tammeveski, Oxygen reduction on electrodeposited Pd coatings on glassy carbon. Electrochimica Acta, 88 (2013) 513-518.

[7] L. Kuai, X. Yu, S. Wang, Y. Sang, B. Geng, Au–Pd alloy and core–shell nanostructures: One-pot coreduction preparation, formation mechanism, and electrochemical properties. Langmuir, 28 (2012) 7168-7173.

[8] J.-J. Lv, S.-S. Li, A.-J. Wang, L.-P. Mei, J.-J. Feng, J.-R. Chen, Z. Chen, One-pot synthesis of monodisperse palladium–copper nanocrystals supported on reduced graphene oxide nanosheets with improved catalytic activity and methanol tolerance for oxygen reduction reaction. Journal of Power Sources, 269 (2014) 104-110.

[9] J.H. Shim, Y.S. Kim, M. Kang, C. Lee, Y. Lee, Electrocatalytic activity of nanoporous Pd and Pt: effect of structural features. Physical Chemistry Chemical Physics, 14 (2012) 3974-3979.

[10] H. Osgood, S.V. Devaguptapu, H. Xu, J. Cho, G. Wu, Transition metal (Fe, Co, Ni, and Mn) oxides for oxygen reduction and evolution bifunctional catalysts in alkaline media. Nano Today, 11 (2016) 601-625.

[11] B. Han, C. Xu, Nanoporous PdFe alloy as highly active and durable electrocatalyst for oxygen reduction reaction. International Journal of Hydrogen Energy, 39 (2014) 18247-18255.

[12] G. Jiang, H. Zhu, X. Zhang, B. Shen, L. Wu, S. Zhang, G. Lu, Z. Wu, S. Sun, Core/shell face-centered tetragonal FePd/Pd nanoparticles as an efficient non-Pt catalyst for the oxygen reduction reaction. ACS nano, 9 (2015) 11014-11022.

[13] J. Liu, C.Q. Sun, W. Zhu, Origin of efficient oxygen reduction reaction on Pd monolayer supported on Pd-M (M= Ni, Fe) intermetallic alloy. Electrochimica Acta, (2018).

[14] M. Tarasevich, A. Sadkowski, E. Yeager, Oxygen electrochemistry, in: Comprehensive treatise of electrochemistry, Springer, 1983, pp. 301-398.

[15] Z. Zhang, K.L. More, K. Sun, Z. Wu, W. Li, Preparation and characterization of PdFe nanoleaves as electrocatalysts for oxygen reduction reaction. Chemistry of Materials, 23 (2011) 1570-1577.

[16] L. Chen, H. Guo, T. Fujita, A. Hirata, W. Zhang, A. Inoue, M. Chen, Nanoporous PdNi Bimetallic Catalyst with Enhanced Electrocatalytic Performances for Electro-oxidation and Oxygen Reduction Reactions. Advanced Functional Materials, 21 (2011) 4364-4370.

[17] J. Jia, H. Yu, X. Gao, J. Chi, Y. Zeng, B. Qin, D. Yao, W. Song, Z. Shao, B. Yi, 3D Pd/Co core–shell nanoneedle arrays as a high-performance cathode catalyst layer for AAEMFCs. RSC Advances, 8 (2018) 12887-12893.

[18] W. Wang, D. Zheng, C. Du, Z. Zou, X. Zhang, B. Xia, H. Yang, D.L. Akins, Carbon-supported Pd-Co bimetallic nanoparticles as electrocatalysts for the oxygen reduction reaction. Journal of Power Sources, 167 (2007) 243-249.

[19] C. Xu, Y. Liu, H. Zhang, H. Geng, A Nanoporous PdCo Alloy as a Highly Active Electrocatalyst for the Oxygen-Reduction Reaction and Formic Acid Electrooxidation. Chemistry–An Asian Journal, 8 (2013) 2721-2728.

[20] J. Mora-Hernández, A. Ezeta-Mejía, C. Reza-San Germán, S. Citalán-Cigarroa, E.M. Arce-Estrada, Electrochemical activity towards ORR of mechanically alloyed PdCo supported on Vulcan carbon and carbon nanospheres. Journal of Applied Electrochemistry, 44 (2014) 1307-1315.

[21] D.N. Son, O.K. Le, V. Chihaia, K. Takahashi, Effects of Co content in Pd-skin/PdCo alloys for oxygen reduction reaction: density functional theory predictions. The Journal of Physical Chemistry C, 119 (2015) 24364-24372.

[22] S. Guo, S. Dong, Graphene nanosheet: synthesis, molecular engineering, thin film, hybrids, and energy and analytical applications. Chemical Society Reviews, 40 (2011) 2644-2672.

[23] R. Kou, Y. Shao, D. Wang, M.H. Engelhard, J.H. Kwak, J. Wang, V.V. Viswanathan, C. Wang, Y. Lin, Y. Wang, Enhanced activity and stability of Pt catalysts on functionalized graphene sheets for electrocatalytic oxygen reduction. Electrochemistry Communications, 11 (2009) 954-957.

[24] Y. Shao, S. Zhang, C. Wang, Z. Nie, J. Liu, Y. Wang, Y. Lin, Highly durable graphene nanoplatelets supported Pt nanocatalysts for oxygen reduction. Journal of Power Sources, 195 (2010) 4600-4605.

[25] Y. Tan, C. Xu, G. Chen, N. Zheng, Q. Xie, A graphene–platinum nanoparticles–ionic liquid composite catalyst for methanol-tolerant oxygen reduction reaction. Energy & Environmental Science, 5 (2012) 6923-6927.

[26] R. Kou, Y. Shao, D. Mei, Z. Nie, D. Wang, C. Wang, V.V. Viswanathan, S. Park, I.A. Aksay, Y. Lin, Stabilization of electrocatalytic metal nanoparticles at metal− metal oxide− graphene triple junction points. Journal of the American Chemical Society, 133 (2011) 2541-2547.

[27] L. Tao, Q. Wang, S. Dou, Z. Ma, J. Huo, S. Wang, L. Dai, Edge-rich and dopant-free graphene as a highly efficient metal-free electrocatalyst for the oxygen reduction reaction. Chemical Communications, 52 (2016) 2764-2767.

[28] H. Peng, Z. Mo, S. Liao, H. Liang, L. Yang, F. Luo, H. Song, Y. Zhong, B. Zhang, High performance Fe-and N-doped carbon catalyst with graphene structure for oxygen reduction. Scientific reports, 3 (2013) 1765.

[29] J. Xu, M. Wang, N.P. Wickramaratne, M. Jaroniec, S. Dou, L. Dai, High-Performance Sodium Ion Batteries Based on a 3D Anode from Nitrogen-Doped Graphene Foams. Advanced materials, 27 (2015) 2042-2048.

[30] Z.-J. Lu, S.-J. Bao, Y.-T. Gou, C.-J. Cai, C.-C. Ji, M.-W. Xu, J. Song, R. Wang, Nitrogen-doped reduced-graphene oxide as an efficient metal-free electrocatalyst for oxygen reduction in fuel cells. Rsc Advances, 3 (2013) 3990-3995.

[31] Y.-H. Lee, K.-H. Chang, C.-C. Hu, Differentiate the pseudocapacitance and double-layer capacitance contributions for nitrogen-doped reduced graphene oxide in acidic and alkaline electrolytes. Journal of Power Sources, 227 (2013) 300-308.

[32] Z.S. Wu, A. Winter, L. Chen, Y. Sun, A. Turchanin, X. Feng, K. Müllen, Three-dimensional nitrogen and boron co-doped graphene for high-performance all-solid-state supercapacitors. Advanced Materials, 24 (2012) 5130-5135.

[33] P.C. Jennings, S. Lysgaard, H.A. Hansen, T. Vegge, Decoupling strain and ligand effects in ternary nanoparticles for improved ORR electrocatalysis. Physical Chemistry Chemical Physics, 18 (2016) 24737-24745.

[34] R. Carrera-Cerritos, V. Baglio, A. Aricò, J. Ledesma-García, M. Sgroi, D. Pullini, A. Pruna, D. Mataix, R. Fuentes-Ramírez, L. Arriaga, Improved Pd electro-catalysis for oxygen reduction reaction in direct methanol fuel cell by reduced graphene oxide. Applied Catalysis B: Environmental, 144 (2014) 554-560.

[35] A. Ejaz, S. Jeon, The individual role of pyrrolic, pyridinic and graphitic nitrogen in the growth kinetics of Pd NPs on N-rGO followed by a comprehensive study on ORR. International Journal of Hydrogen Energy, 43 (2018) 5690-5702.

[36] L. Sun, B. Liao, X. Ren, Y. Li, P. Zhang, L. Deng, Y. Gao, Ternary PdNi-based nanocrystals supported on nitrogen-doped reduced graphene oxide as highly active electrocatalysts for the oxygen reduction reaction. Electrochimica Acta, 235 (2017) 543-552.

[37] B. Gou, W. Na, B. Diong, Fuel cells: dynamic modeling and control with power electronics applications, CRC press, 2016.

[38] A. Dicks, D.A.J. Rand, Fuel cell systems explained, Wiley Online Library, 2018.

[39] C. Kunusch, P. Puleston, M. Mayosky, Sliding-Mode control of PEM fuel cells, Springer Science & Business Media, 2012.

[40] J. Zhang, PEM fuel cell electrocatalysts and catalyst layers: fundamentals and applications, Springer Science & Business Media, 2008.

[41] S. Stankovich, D.A. Dikin, G.H. Dommett, K.M. Kohlhaas, E.J. Zimney, E.A. Stach, R.D. Piner, S.T. Nguyen, R.S. Ruoff, Graphene-based composite materials. nature, 442 (2006) 282.

[42] J.R. Varcoe, R.C. Slade, Prospects for alkaline anion-exchange membranes in low temperature fuel cells. Fuel cells, 5 (2005) 187-200.

[43] G. McLean, T. Niet, S. Prince-Richard, N. Djilali, An assessment of alkaline fuel cell technology. International Journal of Hydrogen Energy, 27 (2002) 507-526.

[44] E. Gülzow, M. Schulze, Long-term operation of AFC electrodes with CO2 containing gases. Journal of Power Sources, 127 (2004) 243-251.

[45] P. Gouérec, L. Poletto, J. Denizot, E. Sanchez-Cortezon, J. Miners, The evolution of the performance of alkaline fuel cells with circulating electrolyte. Journal of Power Sources, 129 (2004) 193-204.

[46] M. Schulze, E. Gülzow, Degradation of nickel anodes in alkaline fuel cells. Journal of Power Sources, 127 (2004) 252-263.

[47] E. Agel, J. Bouet, J.-F. Fauvarque, Characterization and use of anionic membranes for alkaline fuel cells. Journal of Power Sources, 101 (2001) 267-274.

[48] T. Xua, Z. Liub, W. Yanga, Fundamental studies of a new series of anion exchange membranes: membrane prepared from poly (2, 6-dimethyl-1, 4-phenylene oxide)(PPO) and triethylamine. Journal of membrane science, 249 (2005) 183-191.

[49] D.R. Dekel, Review of cell performance in anion exchange membrane fuel cells. Journal of Power Sources, 375 (2018) 158-169.

[50] L. Carrette, K. Friedrich, U. Stimming, Fuel cells–fundamentals and applications. Fuel cells, 1 (2001) 5-39.

[51] N. Brandon, D. Brett, Engineering porous materials for fuel cell applications. Philosophical Transactions of the Royal Society of London A: Mathematical, Physical and Engineering Sciences, 364 (2006) 147-159.

[52] X. Ge, A. Sumboja, D. Wuu, T. An, B. Li, F.T. Goh, T.A. Hor, Y. Zong, Z. Liu, Oxygen reduction in alkaline media: from mechanisms to recent advances of catalysts. Acs Catalysis, 5 (2015) 4643-4667.

[53] S. Kabir, A. Serov, P. Atanassov, 3D-Graphene supports for palladium nanoparticles: effect of micro/macropores on oxygen electroreduction in anion exchange membrane fuel cells. Journal of Power Sources, 375 (2018) 255-264.

[54] E. Antolini, Palladium in fuel cell catalysis. Energy & Environmental Science, 2 (2009) 915-931.

[55] X. Li, Q. Huang, Z. Zou, B. Xia, H. Yang, Low temperature preparation of carbon-supported PdCo alloy electrocatalysts for methanol-tolerant oxygen reduction reaction. Electrochimica Acta, 53 (2008) 6662-6667.

[56] M. Tarasevich, G. Zhutaeva, V. Bogdanovskaya, M. Radina, M. Ehrenburg, A. Chalykh, Oxygen kinetics and mechanism at electrocatalysts on the base of palladium–iron system. Electrochimica acta, 52 (2007) 5108-5118.

[57] S. Liu, C. Deng, L. Yao, H. Zhong, H. Zhang, The key role of metal dopants in nitrogen-doped carbon xerogel for oxygen reduction reaction. Journal of Power Sources, 269 (2014) 225-235.

[58] H. Xiao, Z.-G. Shao, G. Zhang, Y. Gao, W. Lu, B. Yi, Fe–N–carbon black for the oxygen reduction reaction in sulfuric acid. Carbon, 57 (2013) 443-451.

[59] H. Yin, S. Liu, C. Zhang, J. Bao, Y. Zheng, M. Han, Z. Dai, Well-coupled graphene and Pd-based bimetallic nanocrystals nanocomposites for electrocatalytic oxygen reduction reaction. ACS applied materials & interfaces, 6 (2014) 2086-2094.

[60] M.H. Seo, S.M. Choi, D.U. Lee, W.B. Kim, Z. Chen, Correlation between theoretical descriptor and catalytic oxygen reduction activity of graphene supported palladium and palladium alloy electrocatalysts. Journal of Power Sources, 300 (2015) 1-9.

[61] K.S. Novoselov, A.K. Geim, S.V. Morozov, D. Jiang, Y. Zhang, S.V. Dubonos, I.V. Grigorieva, A.A. Firsov, Electric field effect in atomically thin carbon films. science, 306 (2004) 666-669.

[62] L. Ponomarenko, F. Schedin, M. Katsnelson, R. Yang, E. Hill, K. Novoselov, A. Geim, Chaotic Dirac billiard in graphene quantum dots. Science, 320 (2008) 356-358.

[63] F. Ruffino, F. Giannazzo, A Review on Metal Nanoparticles Nucleation and Growth on/in Graphene. Crystals, 7 (2017) 219.

[64] M. Terrones, A.R. Botello-Méndez, J. Campos-Delgado, F. López-Urías, Y.I. Vega-Cantú, F.J. Rodríguez-Macías, A.L. Elías, E. Munoz-Sandoval, A.G. Cano-Márquez, J.-C. Charlier, Graphene and graphite nanoribbons: morphology, properties, synthesis, defects and applications. Nano today, 5 (2010) 351-372.

[65] V. Singh, D. Joung, L. Zhai, S. Das, S.I. Khondaker, S. Seal, Graphene based materials: past, present and future. Progress in materials science, 56 (2011) 1178-1271.

[66] S. Chaudhary, P. Luthra, A. Kumar, Use of Graphene as a Patch Material in comparison to the copper and other Carbon Nanomaterials. (2013).

[67] W. Choi, J.-w. Lee, Graphene: synthesis and applications, CRC press, 2016.

[68] W. Choi, I. Lahiri, R. Seelaboyina, Y.S. Kang, Synthesis of graphene and its applications: a review. Critical Reviews in Solid State and Materials Sciences, 35 (2010) 52-71.

[69] X. Xu, L. Pan, Y. Liu, T. Lu, Z. Sun, D.H. Chua, Facile synthesis of novel graphene sponge for high performance capacitive deionization. Scientific reports, 5 (2015) 8458.

[70] Y. Xu, K. Sheng, C. Li, G. Shi, Self-assembled graphene hydrogel via a one-step hydrothermal process. ACS nano, 4 (2010) 4324-4330.

[71] A.V. Murugan, T. Muraliganth, A. Manthiram, Rapid, facile microwave-solvothermal synthesis of graphene nanosheets and their polyaniline nanocomposites for energy strorage. Chemistry of Materials, 21 (2009) 5004-5006.

[72] S. Perumbilavil, P. Sankar, T. Priya Rose, R. Philip, White light Z-scan measurements of ultrafast optical nonlinearity in reduced graphene oxide nanosheets in the 400–700 nm region. Applied Physics Letters, 107 (2015) 051104.

[73] K. Krishnamoorthy, M. Veerapandian, R. Mohan, S.-J. Kim, Investigation of Raman and photoluminescence studies of reduced graphene oxide sheets. Applied Physics A, 106 (2012) 501-506.

[74] M.S. Dresselhaus, A. Jorio, M. Hofmann, G. Dresselhaus, R. Saito, Perspectives on carbon nanotubes and graphene Raman spectroscopy. Nano letters, 10 (2010) 751-758.

[75] W.I. Hayes, P. Joseph, M.Z. Mughal, P. Papakonstantinou, Production of reduced graphene oxide via hydrothermal reduction in an aqueous sulphuric acid suspension and its electrochemical behaviour. Journal of solid state electrochemistry, 19 (2015) 361-380.

[76] H.H. Yang, R.L. McCreery, Elucidation of the Mechanism of Dioxygen Reduction on Metal-Free Carbon Electrodes. Journal of the Electrochemical Society, 147 (2000) 3420-3428.

[77] B. Zhao, P. Liu, Y. Jiang, D. Pan, H. Tao, J. Song, T. Fang, W. Xu, Supercapacitor performances of thermally reduced graphene oxide. Journal of power sources, 198 (2012) 423-427.

[78] S.-H. Kim, C.-H. Lee, J.-M. Yun, Y.-J. Noh, S.-S. Kim, S. Lee, S.M. Jo, H.-I. Joh, S.-I. Na, Fluorine-functionalized and simultaneously reduced graphene oxide as a novel hole transporting layer for highly efficient and stable organic photovoltaic cells. Nanoscale, 6 (2014) 7183-7187.

[79] S. Yang, L. Zhi, K. Tang, X. Feng, J. Maier, K. Müllen, Efficient synthesis of heteroatom (N or S)-doped graphene based on ultrathin graphene oxide-porous silica sheets for oxygen reduction reactions. Advanced Functional Materials, 22 (2012) 3634-3640.

[80] F. Akbar, M. Kolahdouz, S. Larimian, B. Radfar, H. Radamson, Graphene synthesis, characterization and its applications in nanophotonics, nanoelectronics, and nanosensing. Journal of Materials Science: Materials in Electronics, 26 (2015) 4347-4379.

[81] M. Fan, Z.-Q. Feng, C. Zhu, X. Chen, C. Chen, J. Yang, D. Sun, Recent progress in 2D or 3D N-doped graphene synthesis and the characterizations, properties, and modulations of N species. Journal of materials science, 51 (2016) 10323-10349.

[82] Q. He, Q. Li, S. Khene, X. Ren, F.E. López-Suárez, D. Lozano-Castelló, A. Bueno-López, G. Wu, High-loading cobalt oxide coupled with nitrogen-doped graphene for oxygen reduction in anion-exchange-membrane alkaline fuel cells. The Journal of Physical Chemistry C, 117 (2013) 8697-8707.

[83] Y. Hou, Z. Wen, S. Cui, S. Ci, S. Mao, J. Chen, An advanced nitrogen-doped graphene/cobalt-embedded porous carbon polyhedron hybrid for efficient catalysis of oxygen reduction and water splitting. Advanced Functional Materials, 25 (2015) 872-882.

[84] R.I. Jafri, N. Rajalakshmi, S. Ramaprabhu, Nitrogen doped graphene nanoplatelets as catalyst support for oxygen reduction reaction in proton exchange membrane fuel cell. Journal of Materials Chemistry, 20 (2010) 7114-7117.

[85] D. Usachov, O. Vilkov, A. Gruneis, D. Haberer, A. Fedorov, V. Adamchuk, A. Preobrajenski, P. Dudin, A. Barinov, M. Oehzelt, Nitrogen-doped graphene: efficient growth, structure, and electronic properties. Nano letters, 11 (2011) 5401-5407.

[86] L. Qu, Y. Liu, J.-B. Baek, L. Dai, Nitrogen-doped graphene as efficient metal-free electrocatalyst for oxygen reduction in fuel cells. ACS nano, 4 (2010) 1321-1326.

[87] Y. Baskin, L. Meyer, Lattice constants of graphite at low temperatures. Physical Review, 100 (1955) 544.

[88] L. Sun, L. Wang, C. Tian, T. Tan, Y. Xie, K. Shi, M. Li, H. Fu, Nitrogen-doped graphene with high nitrogen level via a one-step hydrothermal reaction of graphene oxide with urea for superior capacitive energy storage. Rsc Advances, 2 (2012) 4498-4506.

[89] D. Long, W. Li, L. Ling, J. Miyawaki, I. Mochida, S.-H. Yoon, Preparation of nitrogen-doped graphene sheets by a combined chemical and hydrothermal reduction of graphene oxide. Langmuir, 26 (2010) 16096-16102.

[90] D. Deng, X. Pan, L. Yu, Y. Cui, Y. Jiang, J. Qi, W.-X. Li, Q. Fu, X. Ma, Q. Xue, Toward N-doped graphene via solvothermal synthesis. Chemistry of Materials, 23 (2011) 1188-1193.

[91] H.-L. Guo, P. Su, X. Kang, S.-K. Ning, Synthesis and characterization of nitrogen-doped graphene hydrogels by hydrothermal route with urea as reducing-doping agents. Journal of Materials Chemistry A, 1 (2013) 2248-2255.

[92] O.O. Fashedemi, K.I. Ozoemena, Enhanced methanol oxidation and oxygen reduction reactions on palladium-decorated FeCo@ Fe/C core–shell nanocatalysts in alkaline medium. Physical Chemistry Chemical Physics, 15 (2013) 20982-20991.

[93] Y.J. Sa, K. Kwon, J.Y. Cheon, F. Kleitz, S.H. Joo, Ordered mesoporous Co 3 O 4 spinels as stable, bifunctional, noble metal-free oxygen electrocatalysts. Journal of Materials Chemistry A, 1 (2013) 9992-10001.

[94] B. Ruiz-Camacho, R. Morales-Rodriguez, A.M. Ramírez, Pt–Ag/C catalyst for methanol oxidation and alcohol tolerant cathode in different electrolytes. International Journal of Hydrogen Energy, 41 (2016) 23336-23344.

[95] K. Byrappa, M. Yoshimura, Handbook of hydrothermal technology, William Andrew, 2012.

[96] Y. Zhou, Q. Bao, L.A.L. Tang, Y. Zhong, K.P. Loh, Hydrothermal dehydration for the “green” reduction of exfoliated graphene oxide to graphene and demonstration of tunable optical limiting properties. Chemistry of Materials, 21 (2009) 2950-2956.

[97] X. Mei, X. Meng, F. Wu, Hydrothermal method for the production of reduced graphene oxide. Physica E: Low-dimensional Systems and Nanostructures, 68 (2015) 81-86.

[98] J.N. Israelachvili, Intermolecular and surface forces, Academic press, 2011.

[99] M.A. Molina-García, N.V. Rees, “Metal-free” electrocatalysis: Quaternary-doped graphene and the alkaline oxygen reduction reaction. Applied Catalysis A: General, 553 (2018) 107-116.

[100] H.J. Shin, K.K. Kim, A. Benayad, S.M. Yoon, H.K. Park, I.S. Jung, M.H. Jin, H.K. Jeong, J.M. Kim, J.Y. Choi, Efficient reduction of graphite oxide by sodium borohydride and its effect on electrical conductance. Advanced Functional Materials, 19 (2009) 1987-1992.

[101] L. Tang, Y. Wang, Y. Li, H. Feng, J. Lu, J. Li, Preparation, structure, and electrochemical properties of reduced graphene sheet films. Advanced Functional Materials, 19 (2009) 2782-2789.

[102] Z. Mo, R. Zheng, H. Peng, H. Liang, S. Liao, Nitrogen-doped graphene prepared by a transfer doping approach for the oxygen reduction reaction application. Journal of Power Sources, 245 (2014) 801-807.

[103] Y. Wang, M. Zhang, D. Pan, Y. Li, T. Ma, J. Xie, Nitrogen/sulfur co-doped graphene networks uniformly coupled N-Fe2O3 nanoparticles achieving enhanced supercapacitor performance. Electrochimica Acta, 266 (2018) 242-253.

[104] J. Long, X. Xie, J. Xu, Q. Gu, L. Chen, X. Wang, Nitrogen-doped graphene nanosheets as metal-free catalysts for aerobic selective oxidation of benzylic alcohols. Acs Catalysis, 2 (2012) 622-631.

[105] X. Duan, S. Indrawirawan, H. Sun, S. Wang, Effects of nitrogen-, boron-, and phosphorus-doping or codoping on metal-free graphene catalysis. Catalysis Today, 249 (2015) 184-191.

[106] Y.-R. Chen, Q. Wang, X. Bai, Z. Yan, Y. Ning, F. He, Z. Wu, J. Zhang, Unexpected catalytic performance of Fe–M–C (M= N, P, and S) electrocatalysts towards oxygen reduction reaction: surface heteroatoms boost the activity of Fe 2 M/graphene nanocomposites. Dalton Transactions, 46 (2017) 16885-16894.

[107] J. Tai, J. Hu, Z. Chen, H. Lu, Two-step synthesis of boron and nitrogen co-doped graphene as a synergistically enhanced catalyst for the oxygen reduction reaction. RSC Advances, 4 (2014) 61437-61443.

[108] T. Wang, L.-X. Wang, D.-L. Wu, W. Xia, D.-Z. Jia, Interaction between nitrogen and sulfur in co-doped graphene and synergetic effect in supercapacitor. Scientific Reports, 5 (2015) 9591.

[109] C. Fu, C. Song, L. Liu, X. Xie, W. Zhao, Synthesis and properties of nitrogen-doped graphene as anode materials for lithium-ion batteries. Int. J. Electrochem. Sci, 11 (2016) 3876.

[110] A.E. Vilian, M. Rajkumar, S.-M. Chen, C.-C. Hu, S. Piraman, A promising photoelectrochemical sensor based on a ZnO particle decorated N-doped reduced graphene oxide modified electrode for simultaneous determination of catechol and hydroquinone. RSC Advances, 4 (2014) 48522-48534.

[111] S. Maldonado, S. Morin, K.J. Stevenson, Structure, composition, and chemical reactivity of carbon nanotubes by selective nitrogen doping. Carbon, 44 (2006) 1429-1437.

[112] S.K. Bikkarolla, P. Cumpson, P. Joseph, P. Papakonstantinou, Oxygen reduction reaction by electrochemically reduced graphene oxide. Faraday discussions, 173 (2014) 415-428.

[113] M. Hassan, E. Haque, A.I. Minett, V.G. Gomes, Co-Doping of Activated Graphene for Synergistically Enhanced Electrocatalytic Oxygen Reduction Reaction. ChemSusChem, 8 (2015) 4040-4048.

[114] H. Zhang, T. Kuila, N.H. Kim, D.S. Yu, J.H. Lee, Simultaneous reduction, exfoliation, and nitrogen doping of graphene oxide via a hydrothermal reaction for energy storage electrode materials. Carbon, 69 (2014) 66-78.

[115] Z. Zhang, S. Yang, M. Dou, H. Liu, L. Gu, F. Wang, Systematic study of transition-metal (Fe, Co, Ni, Cu) phthalocyanines as electrocatalysts for oxygen reduction and their evaluation by DFT. RSC Advances, 6 (2016) 67049-67056.

[116] J.W. Lee, J.M. Ko, J.-D. Kim, Hydrothermal preparation of nitrogen-doped graphene sheets via hexamethylenetetramine for application as supercapacitor electrodes. Electrochimica Acta, 85 (2012) 459-466.

[117] Z. Wen, X. Wang, S. Mao, Z. Bo, H. Kim, S. Cui, G. Lu, X. Feng, J. Chen, Crumpled nitrogen-doped graphene nanosheets with ultrahigh pore volume for high-performance supercapacitor. Advanced materials, 24 (2012) 5610-5616.

[118] L. Chen, R. Du, J. Zhu, Y. Mao, C. Xue, N. Zhang, Y. Hou, J. Zhang, T. Yi, Three-Dimensional Nitrogen-Doped Graphene Nanoribbons Aerogel as a Highly Efficient Catalyst for the Oxygen Reduction Reaction. Small, 11 (2015) 1423-1429.

[119] L. Wang, F. Yin, C. Yao, N-doped graphene as a bifunctional electrocatalyst for oxygen reduction and oxygen evolution reactions in an alkaline electrolyte. International journal of hydrogen energy, 39 (2014) 15913-15919.

[120] Y. Xue, J. Liu, H. Chen, R. Wang, D. Li, J. Qu, L. Dai, Nitrogen-doped graphene foams as metal-free counter electrodes in high-performance dye-sensitized solar cells. Angewandte Chemie International Edition, 51 (2012) 12124-12127.

[121] M. Jahan, Z. Liu, K.P. Loh, A Graphene oxide and copper-centered metal organic framework composite as a tri-functional catalyst for HER, OER, and ORR. Advanced Functional Materials, 23 (2013) 5363-5372.

[122] K. Mohanraju, L. Cindrella, Impact of alloying and lattice strain on ORR activity of Pt and Pd based ternary alloys with Fe and Co for proton exchange membrane fuel cell applications. RSC Advances, 4 (2014) 11939-11947.

[123] Y.-H. Cho, O.-H. Kim, D.Y. Chung, H. Choe, Y.-H. Cho, Y.-E. Sung, PtPdCo ternary electrocatalyst for methanol tolerant oxygen reduction reaction in direct methanol fuel cell. Applied Catalysis B: Environmental, 154 (2014) 309-315.

[124] X. Ren, B. Liao, Y. Li, P. Zhang, L. Deng, Y. Gao, Facile synthesis of PdSnCo/nitrogen-doped reduced graphene as a highly active catalyst for lithium-air batteries. Electrochimica Acta, 228 (2017) 36-44.

[125] F. Ren, C. Wang, C. Zhai, F. Jiang, R. Yue, Y. Du, P. Yang, J. Xu, One-pot synthesis of a RGO-supported ultrafine ternary PtAuRu catalyst with high electrocatalytic activity towards methanol oxidation in alkaline medium. Journal of Materials Chemistry A, 1 (2013) 7255-7261.

[126] J.N. Tiwari, W.G. Lee, S. Sultan, M. Yousuf, A.M. Harzandi, V. Vij, K.S. Kim, High-affinity-assisted nanoscale alloys as remarkable bifunctional catalyst for alcohol oxidation and oxygen reduction reactions. ACS nano, 11 (2017) 7729-7735.

[127] C. He, J. Tao, P.K. Shen, Solid Synthesis of Ultrathin Palladium and Its Alloys’ Nanosheets on RGO with High Catalytic Activity for Oxygen Reduction Reaction. ACS Catalysis, 8 (2018) 910-919.

[128] M.M. van Schooneveld, C. Campos-Cuerva, J. Pet, J.D. Meeldijk, J. van Rijssel, A. Meijerink, B.H. Erné, F.M. de Groot, Composition tunable cobalt–nickel and cobalt–iron alloy nanoparticles below 10 nm synthesized using acetonated cobalt carbonyl. Journal of Nanoparticle Research, 14 (2012) 991.

[129] Y. Zhai, Z. Zhu, X. Lu, Z. Zhou, J. Shao, H.S. Zhou, Facile synthesis of three-dimensional PtPdNi fused nanoarchitecture as highly active and durable electrocatalyst for methanol oxidation. ACS Applied Energy Materials, 1 (2018) 32-37.

[130] X. Mei, J. Ouyang, Ultrasonication-assisted ultrafast reduction of graphene oxide by zinc powder at room temperature. Carbon, 49 (2011) 5389-5397.

[131] R. Krishna, E. Titus, O. Okhay, J.C. Gil, J. Ventura, E.V. Ramana, J.J. Gracio, Rapid electrochemical synthesis of hydrogenated graphene oxide using Ni nanoparticles. Int J Electrochem Sci, 9 (2014) e69.

[132] K. An, S. Alayoglu, N. Musselwhite, K. Na, G.A. Somorjai, Designed catalysts from Pt nanoparticles supported on macroporous oxides for selective isomerization of n-hexane. Journal of the American Chemical Society, 136 (2014) 6830-6833.

[133] K. An, G.A. Somorjai, Size and shape control of metal nanoparticles for reaction selectivity in catalysis. ChemCatChem, 4 (2012) 1512-1524.

[134] L. Perini, C. Durante, M. Favaro, V. Perazzolo, S. Agnoli, O. Schneider, G. Granozzi, A. Gennaro, Metal–support interaction in platinum and palladium nanoparticles loaded on nitrogen-doped mesoporous carbon for oxygen reduction reaction. ACS applied materials & interfaces, 7 (2015) 1170-1179.

[135] N.M. Markovic, H.A. Gasteiger, P.N. Ross, Oxygen reduction on platinum low-index single-crystal surfaces in alkaline solution: rotating ring diskPt (hkl) studies. The Journal of Physical Chemistry, 100 (1996) 6715-6721.

[136] D.A. Stevens, J.R. Dahn, Electrochemical characterization of the active surface in carbon-supported platinum electrocatalysts for PEM fuel cells. Journal of The Electrochemical Society, 150 (2003) A770-A775.

[137] P. Raghavendra, G.V. Reddy, R. Sivasubramanian, P.S. Chandana, L.S. Sarma, Reduced graphene oxide-supported Pd@ Au bimetallic nano electrocatalyst for enhanced oxygen reduction reaction in alkaline media. International Journal of Hydrogen Energy, 43 (2017) 4125-3135.

[138] D. Park, M.S. Ahmed, S. Jeon, Covalent functionalization of graphene with 1, 5-diaminonaphthalene and ultrasmall palladium nanoparticles for electrocatalytic oxygen reduction. International Journal of Hydrogen Energy, 42 (2017) 2061-2070.

[139] D. Wang, H.L. Xin, R. Hovden, H. Wang, Y. Yu, D.A. Muller, F.J. DiSalvo, H.D. Abruña, Structurally ordered intermetallic platinum–cobalt core–shell nanoparticles with enhanced activity and stability as oxygen reduction electrocatalysts. Nature materials, 12 (2013) 81.

[140] L. Bu, N. Zhang, S. Guo, X. Zhang, J. Li, J. Yao, T. Wu, G. Lu, J.Y. Ma, D. Su, X. Huang, Biaxially strained PtPb/Pt core/shell nanoplate boosts oxygen reduction catalysis. Science, 354 (2016) 1410-1414.

[141] V.A. Setyowati, H.C. Huang, C.C. Liu, C.H. Wang, Effect of iron precursors on the structure and oxygen reduction activity of iron–nitrogen–carbon catalysts. Electrochimica Acta, 211 (2016) 933-940.

[142] C. He, P.K. Shen, Pt loaded on truncated hexagonal pyramid WC/graphene for oxygen reduction reaction. Nano Energy, 8 (2014) 52-61.

[143] G.A. Goenaga, A.L. Roy, N.M. Cantillo, S. Foister, T.A. Zawodzinski, A family of platinum group metal-free catalysts for oxygen reduction in alkaline media. Journal of Power Sources, 395 (2018) 148-157.

[144] H. Peng, F. Liu, X. Liu, S. Liao, C. You, X. Tian, H. Nan, F. Luo, Z. Fu, P. Huang, Effect of transition metals on the structure and performance of the doped carbon catalysts derived from polyaniline and melamine for ORR application. ACS Catalysis, 4 (2014) 3797-3805.

[145] L.X. Chen, L.Y. Jiang, A.J. Wang, Q.Y. Chen, J.J. Feng, Simple synthesis of bimetallic AuPd dendritic alloyed nanocrystals with enhanced electrocatalytic performance for hydrazine oxidation reaction. Electrochimica Acta, 190 (2016) 872-878.

[146] Y.N. Liu, X. Zhou, X. Wang, K. Liang, Z.K. Yang, C.C. Shen, M. Imran, S. Sahar, A.W. Xu, Hydrogenation/oxidation induced efficient reversible color switching between methylene blue and leuco-methylene blue. RSC Advances, 7 (2017) 30080-30085.

[147] J. Sun, Y. Fu, G. He, X. Sun, X. Wang, Catalytic hydrogenation of nitrophenols and nitrotoluenes over a palladium/graphene nanocomposite. Catalysis Science & Technology, 4 (2014) 1742-1748.

[148] B. Hu, T. Wu, K. Ding, X. Zhou, T. Jiang, B. Han, Seeding growth of Pd/Au bimetallic nanoparticles on highly cross-linked polymer microspheres with ionic liquid and solvent-free hydrogenation. The Journal of Physical Chemistry C, 114 (2010) 3396-3400.

[149] V.B. Parambhath, R. Nagar, S. Ramaprabhu, Effect of nitrogen doping on hydrogen storage capacity of palladium decorated graphene. Langmuir, 28 (2012) 7826-7833.

[150] M. Martins, B. Šljukić, Ö. Metin, M. Sevim, C.A. Sequeira, T. Şener, D.M. Santos, Bimetallic PdM (M= Fe, Ag, Au) alloy nanoparticles assembled on reduced graphene oxide as catalysts for direct borohydride fuel cells. Journal of Alloys and Compounds, 718 (2017) 204-214.

[151] M. Yun, M.S. Ahmed, S. Jeon, Thiolated graphene oxide-supported palladium cobalt alloyed nanoparticles as high performance electrocatalyst for oxygen reduction reaction. Journal of Power Sources, 293 (2015) 380-387.

[152] B. Çelik, Y. Yıldız, H. Sert, E. Erken, Y. Koşkun, F. Şen, Monodispersed palladium–cobalt alloy nanoparticles assembled on poly (N-vinyl-pyrrolidone)(PVP) as a highly effective catalyst for dimethylamine borane (DMAB) dehydrocoupling. RSC Advances, 6 (2016) 24097-24102.

[153] Z. Li, Q. Gao, H. Zhang, W. Tian, Y. Tan, W. Qian, Z. Liu, Low content Pt nanoparticles anchored on N-doped reduced graphene oxide with high and stable electrocatalytic activity for oxygen reduction reaction. Scientific reports, 7 (2017) 43352.

[154] D. Yu, Q. Zhang, L. Dai, Highly efficient metal-free growth of nitrogen-doped single-walled carbon nanotubes on plasma-etched substrates for oxygen reduction. Journal of the American Chemical Society, 132 (2010) 15127-15129.

[155] S. Chen, J. Bi, Y. Zhao, L. Yang, C. Zhang, Y. Ma, Q. Wu, X. Wang, Z. Hu, Nitrogen-doped carbon nanocages as efficient metal-free electrocatalysts for oxygen reduction reaction. Advanced materials, 24(2012), 5593-5597.

[156] Y. Nie, L. Li, Z. Wei, Recent advancements in Pt and Pt-free catalysts for oxygen reduction reaction. Chemical Society Reviews, 44 (2015) 2168-2201.

[157] D. Guo, R. Shibuya, C. Akiba, S. Saji, T. Kondo, J. Nakamura, Active sites of nitrogen-doped carbon materials for oxygen reduction reaction clarified using model catalysts. Science, 351 (2016) 361-365.

[158] W. Ding, Z. Wei, S. Chen, X. Qi, T. Yang, J. Hu, D. Wang, L.J. Wan, S.F. Alvi, L. Li, Space-Confinement-Induced Synthesis of Pyridinic-and Pyrrolic-Nitrogen-Doped Graphene for the Catalysis of Oxygen Reduction. Angewandte Chemie, 125 (2013) 11971-11975.

[159] H. Niwa, K. Horiba, Y. Harada, M. Oshima, T. Ikeda, K. Terakura, J.I. Ozaki, S. Miyata, X-ray absorption analysis of nitrogen contribution to oxygen reduction reaction in carbon alloy cathode catalysts for polymer electrolyte fuel cells. Journal of Power Sources, 187 (2009) 93-97.

[160] R. Liu, D. Wu, X. Feng, K. Müllen, Nitrogen-doped ordered mesoporous graphitic arrays with high electrocatalytic activity for oxygen reduction. Angewandte Chemie, 122 (2010) 2619-2623.

[161] H.R. Colón-Mercado, B.N. Popov, Stability of platinum based alloy cathode catalysts in PEM fuel cells. Journal of Power Sources, 155 (2006) 253-263.

[162] P.J. Ferreira, Y. Shao-Horn, D. Morgan, R. Makharia, S. Kocha, H.A. Gasteiger, Instability of Pt⁄ C electrocatalysts in proton exchange membrane fuel cells a mechanistic investigation. Journal of The Electrochemical Society, 152 (2005) A2256-A2271.

[163] J.E. Choe, M.S. Ahmed, S. Jeon, 3, 4-Ethylenedioxythiophene functionalized graphene with palladium nanoparticles for enhanced electrocatalytic oxygen reduction reaction. Journal of Power Sources, (2015) 211-218.

– An intentionally blank page –

BIOGRAPHY

Frizka Vietanti was born in Banyuwangi (Indonesia) on 18 January 1994. She is second daughter of Ahmad Kusaeri and Indah Hariyati. She got her bachelor degree of engineering from Materials and Metallurgical Engineering ITS Indonesia. Her final project for bachelor degree was "**Analysis The Effect of Mass Zinc Reductor in Electrocatalyst PdAu/Graphene Synthesis on The Performance of Direct Methanol Fuel Cells (DMFC)**". She got opportunity for pursuit double degree program in Taiwan. Therefore, she also studied in Materials Science and Engineering NTUST Taiwan. When study in NTUST, she doing a reaseach about fuel cell. She got her master degree with the thesis title "**Ternary Palladium based Cathode Catalyst Supported on Nitrogen doped Reduced Graphene Oxide for AEMFC**".

– An intentionally blank page –